UNIVERSITÀ DEGLI STUDI DI PADOVA

Department of Information Engineering
University of Padova, Padova, Italy
XXIX Ph.D. Course
Curriculum: Bioengineering

MOVING BEYOND DTI: NON-GAUSSIAN DIFFUSION IN THE BRAIN AND SKELETAL MUSCLE

This Ph.D. has been funded by the Scientific Institute IRCCS Eugenio Medea, Bosisio Parini, LC, Italy.

Headmaster
Prof. Matteo Bertocco
Supervisor
Prof. Alessandra Bertoldo
Co-Supervisors:
Dr. Filippo Arrigoni
Dr. Martijn Froeling

Ph.D. candidate
Alberto De Luca

Moving beyond DTI: non-Gaussian diffusion in the brain and skeletal muscle

ABSTRACT

Diffusion Magnetic Resonance Imaging (dMRI) is a diagnostic technique able to provide in-vivo measures that are related to the microstructure of tissues. The key idea behind the technique is the acquisition of a series of images that are limited in spatial resolution, within the millimeters scale, but are sensitized to the random motion (diffusion) of water molecules. The diffusion measurements are performed in the timescale of milliseconds, thus images provide an indirect measure of molecular displacement in the range of micrometers. This thesis shows the developments and the results I achieved during my PhD studies. Most of the research here included has been carried out in a multi-disciplinary environment, that includes engineering and medical skills, therefore the first plural person will be used throughout the work. Chapter I covers the general principles of molecular diffusion, Magnetic Resonance Imaging (MRI) and dMRI that are essential for the development of this thesis, referring the interested reader to the appropriate sources to deepen the concepts. Thanks to the sensitivity to microstructural tissue changes, Diffusion Weighted Imaging (DWI) and derived metrics, as the Apparent Diffusion Coefficient (ADC) (Denis Le Bihan & Breton, 1985), became the gold standard for the detection of strokes and ischemia since the early 90's. Nevertheless, over time many sophisticated dMRI approaches have been developed. In 1994 Basser and colleagues introduced Diffusion Tensor Imaging (DTI), the first quantification approach able to capture the anisotropy of the diffusion process in in-vivo biological tissues. Chapter II introduces the theoretical formulation of this popular method, then shows the results we obtained applying DTI to investigate white matter alterations of a population affected by Friedreich's Ataxia (Vavla et al., 2015).

After more than 20 years from its introduction, DTI is still widely applied. However, concerns about the limitations of the technique have been increasingly risen over-time. A limitation regards the lack of specificity of the model in the context of biological tissues, that are highly heterogeneous in composition and properties. For this reason, when signals arise from tissues with limited directional architecture, as gray matter in the brain, or from tissues with multiple architectures, as crossing fibers in white matter, metrics provided by DTI are often uninformative. Additionally, the tensor model can be applied only to a range of "moderate" diffusion sensitizations, after which the presence of biological membranes

becomes non-negligible and gives origin to phenomena of "non-Gaussian diffusion", that violate the assumptions of the model. Chapter III and Chapter IV deal specifically with these limitations, addressing the problem with two different approaches and applications. In particular, Chapter III deals with the Neurite Orientation Dispersion and Density Imaging (NODDI) technique, that has been introduced by Zhang and colleagues in 2012 to provide microstructure specific metrics in the brain. In this thesis we present its applications to investigate temporal lobe damage in a population affected by Multiple Sclerosis (MS) (M Calabrese et al., 2016; Alberto De Luca, Castellaro, Montemezzi, Calabrese, & Bertoldo, 2015a). Another popular technique to investigate the dMRI signal is Spherical Deconvolution (SD), that in Chapter IV is presented in a tissue specific formulation and applied to derive diffusivity metrics specific to white matter, gray matter and cerebrospinal fluid, both in healthy controls and in a patient affected by MS (Alberto De Luca, Castellaro, Montemezzi, Calabrese, & Bertoldo, 2015b).

Since the early days of dMRI, experiments have been performed not only in the brain but in several body districts, including the skeletal muscle. In particular, the acquisition of diffusion weighted data and the application of DTI to the skeletal muscles have been shown to be feasible since the '90s (Van Donkelaar et al., 1999). However, although many concepts used in brain acquisitions can easily be adapted, the great difference in cellular types, structure and composition of the tissues yield to technical and theoretical challenges with non-trivial solution. Back in 1986 Le Bihan et al. (D Le Bihan et al., 1986) observed that the water flowing in the micro vascular network and in the vessels was contributing to the acquisition of data at very low diffusion sensitization. Upon these observations, they proposed the "Intra-Voxel Incoherent Motion" (IVIM) model, that expressed the dMRI signal as sum of tissue and blood signals, that can be recognized among the first examples of non mono-exponential Gaussian diffusion. The IVIM model was originally described in the brain but has found a number of applications to the skeletal muscle. IVIM can be seen either as a model to obtain measures of pseudo-diffusion (Nguyen et al., 2016), or as a technique to obtain perfusion free ADC measures, thus recognizing it as an artifact (Denis Le Bihan, 2013). Although dMRI and DTI were applied to the skeletal muscle since its early days, later evolutions as Diffusion Kurtosis Imaging (Jensen, Helpern, Ramani, Lu, & Kaczynski, 2005) have only recently been applied to the skeletal muscle (Marschar et al., 2015) to fit dMRI data acquired at strong diffusion sensitization. The concepts of IVIM and DKI are developed in Chapter V, where the effects of the first on DTI and DKI, as well as the relation between DTI and DKI metrics

are investigated through simulations and MRI data of the calf (Alberto De Luca, Bertoldo, & Froeling, 2016).

In line with the current dMRI literature, the first 5 chapters of this thesis depict the diffusion signal as a complex measure arising from multiple tissue components, that can be partially disentangled through multi-compartmental modeling and acquisition of appropriate data. One of the difficulties with multi-compartment models is the optimal choice of the number of components, that is clearly tissue but also technologically dependent. Chapter VI investigates a multi-compartment pseudo-continuous deconvolution approach (Alberto De Luca, Bertoldo, Arrigoni, & Froeling, 2016), a technique that does not require explicit modeling of the tissues. The method is applied to estimate different diffusion regimes in the brain comparing dMRI data acquired with both a conventional and a non-conventional dMRI sequence. Finally, Chapter VII presents an overview of other research topics I have work on during the PhD.

Contents

CHAPTER I: THEORY OF THE DIFFUSION MR SIGNAL

Introduction to NMR

Magnetic Resonance Imaging (MRI) is one of the most successful and popular diagnostic tool, and can be regarded as the gold-standard technique to investigate biological tissues in-vivo. The physical foundation of MRI is Nuclear Magnetic Resonance (NMR), a phenomena observed when atoms with non-null magnetic moment (NMR active nuclei) are placed in a strong and static magnetic field. In the context of medical NMR, the hydrogen atom (^{1}H) represents the most obvious and well-known choice. Being made of a single proton, it has spin number ½ and thus has a non-null magnetic moment. Moreover, ^{1}H constitutes 2/3 of the water molecules and it is therefore abundant in biological tissues. When an atom with non-null magnetic moment is placed in a strong and static magnetic field (B_0), the spin axis aligns to form a characteristic angle with the direction of B_0 and undergoes a precession motion as shown in **Figure 1**.

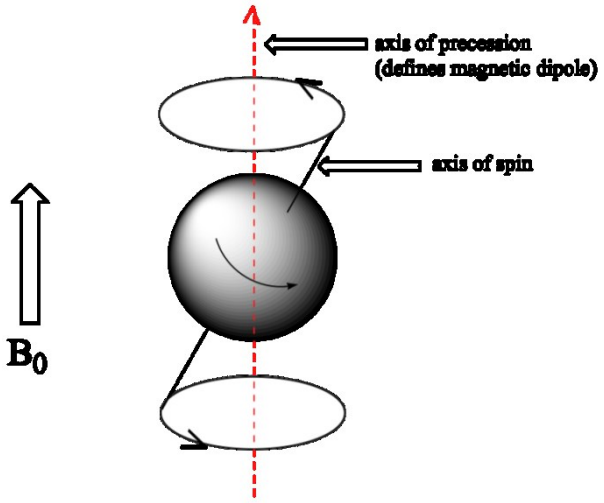

Figure 1: The precession of a spin around its magnetic dipole (dotted red line), that is aligned with the imposed field B_0. The precession angle in steady-state is characteristic of the spin species.

^{1}H can assume two spin states, +½ when the angle between its direction and B_0 is acute, -½ when it has opposite direction and the angle with B_0 is obtuse. The +½ state has lower energy than -½, thus in a large sample the positive state is slightly more abundant (the +½ over -½

ratio increases with B_0). The precession frequency of the spin is called Larmor frequency (ν_L) and essentially depends on the chemical specie and on the strength of B_0:

$$\nu_L = \gamma \frac{B_0}{2\pi} \quad [1]$$

where γ is the gyromagnetic ratio, that is equal to 2.68x10^8 rad/s/T for ^{1}H, and ν_L equals to 127.728MHz at 3T. The resonance phenomena take place when a population of protons precessing around B_0 is irradiated with radio-frequency (RF) waves (B_1^+) at the frequency ν_L and with direction perpendicular to that of the main field, causing the transition of a number of spins from the +½ state to -½ (proportionally to the irradiating energy). Under these conditions, the net magnetic moment M of the population, that was substantially aligned with B_0, rotates of an angle α (see **Figure 2**).

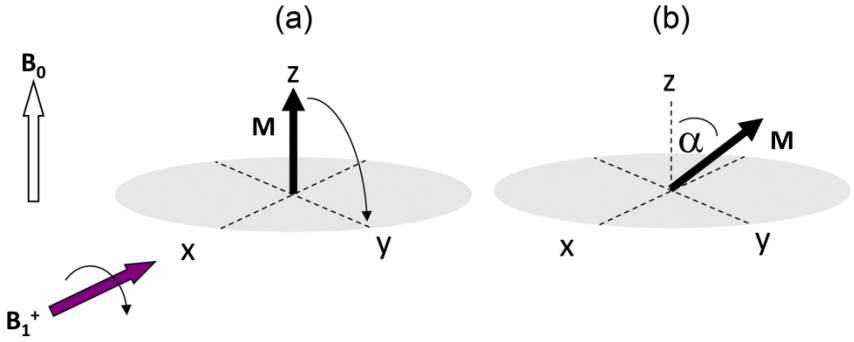

Figure 2: The net magnetic moment M of the spin population is aligned with B_0 in steady state (a). The application of a perpendicular field B_1^+ flips M on the x-y plane proportionally to its strength and duration.

If M is decomposed in its longitudinal component along the z-axis (M_Z) and its transverse component (M_{XY}) in an orthogonal tri-dimensional plane, it is noticeable that B_1^+ substantially converts the longitudinal component into transverse magnetization (that was null during the steady state). When B_1^+ is turned off, the system recovers the original steady state oscillating in the x-y plane. Such oscillations in the transverse plane can be converted into electronic signals with receiver coils tuned at the appropriate Larmor frequency, giving origin to the Free Induction Decay (FID) signal. Such signal is what is measured in an NMR experiment. The angle α is called flip-angle, and can be tuned by appropriate choice of the applied field B_1^+ (that is in the order of magnitude of μT) and its duration t_p:

$$\alpha = \gamma B_1{}^+ t_p \quad [2]$$

The NMR signal can be mathematically described with the Bloch equation (Bloch, Hansen, & Packard, 1946a, 1946b), that introduces a relation between the magnetization observed in the three dimensional axis $M=(M_X,M_Y,M_Z)$ and the time constants T_1 and T_2:

$$\frac{dM_X}{dt} = \gamma(M \times B_0)_X - \frac{M_X}{T_2} \quad [3]$$

$$\frac{dM_Y}{dt} = \gamma(M \times B_0)_Y - \frac{M_Y}{T_2} \quad [4]$$

$$\frac{dM_Z}{dt} = \gamma(M \times B_0)_Z - \frac{M_Z - M_0}{T_1} \quad [5]$$

M_0 is the magnetization at steady-state, T_1 is the longitudinal magnetization constant that defines the rate of recovery of the M_Z component to M_0, while T_2 is the transverse magnetization constant, that describes the rate of M_{XY} nulling. In line of principle, the T_2 could be inferred from the FID signal described above, that was generated imposing a flip-angle of 90 degrees to completely rotate M_0 on the transverse plane. Using the Bloch equations, the following solution can be derived for such experiment:

$$M_{XY} = M_0 e^{-\frac{t}{T_2^*}} \quad [6]$$

$$\frac{1}{T_2^*} = \frac{1}{T_2} + \frac{1}{\gamma \Delta B_0} \quad [7]$$

where the term ΔB_0 accounts for the local field inhomogeneity that affects any real magnet. In 1950 Hahn (Hahn, 1950) introduced the concept of Spin-Echo, an NMR sequence (i.e. a series of RF pulses to obtained pre-determined flip-angles) to determine pure T_2 signals. The Spin-Echo sequence consists of two RF pulses spaced with a time $T_E/2$, the first designed to obtain a 90 degrees flip-angle, the second to impose a flip angle equal to 180 degrees. The first RF pulse completely rotates the magnetization vector on the transverse plane, exactly as in the FID experiment. However, without additional stimulation the local field inhomogeneity would result in additional loss of coherence (de-phasing) of the spins, further attenuating the signal. Indeed, the second RF pulse flips the X-Y component of the magnetization vector, reversing the effect of field inhomogeneity to obtain a completely refocused vector field after an additional time $T_E/2$, thus producing a completely refocused echo after a total time T_E (called Echo Time). The process is exemplified in **Figure 3**.

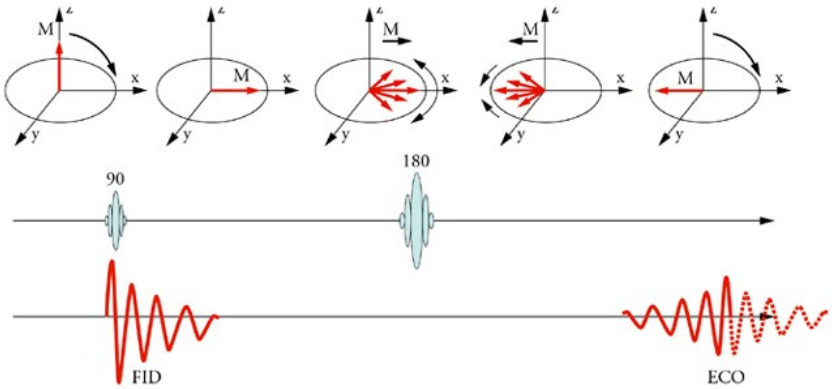

Figure 3: Effects of the spin-echo sequence on the net magnetization vector M. The first 90 degrees pulse rotates M on the x-y plane. T_2^* dephasing induces loss of coherence in the x-y plane. The 180 degrees swaps the sign of M, thus identical but opposite T_2^* effects compensate for the initial dephasing and result in fully refocused transverse magnetization.

The diffusion process

In 1828 Robert Brown described the motion of pollen grains suspended in water (V.P.L.S., 1828), observing for the first time what was later called Brownian motion or diffusion process. Adolf Fick proposed two laws to describe the Brownian motion (Fick, 1855). The first determines the flow in terms of spatial position (x) under stationary conditions, while the second expresses the particle density as function of the flow over time:

$$\vec{J} = -\frac{\partial}{\partial x}(D\rho) \quad [8]$$

$$\frac{\partial \rho}{\partial t} + \frac{\partial \vec{J}}{\partial x} = 0 \quad [9]$$

where $\vec{J}$ denotes the net molecular flow, D is the diffusion coefficient and ρ is the particle density. Combining the two equations under the assumption of isotropic D, the following equation can be derived:

$$\frac{\partial \rho}{\partial t} = D\frac{\partial^2 \rho}{\partial x^2} \quad [10]$$

The solution to this second order differential equation was proposed by Albert Einstein (Einstein, 1905):

$$\rho(x,t) = \frac{1}{\sqrt{4\pi D t}} e^{-\frac{x^2}{4Dt}} \quad [11]$$

Eq. [11] corresponds to a Gaussian diffusion process with zero mean and standard deviation given by:

$$\sigma = \sqrt{2Dt} \quad [12]$$

The aforementioned diffusion process is often referred as self-diffusion, i.e. the Brownian motion of molecules in a homogeneous media without concentration gradients, such that D does not vary over time due to gradient flow. Eq. [12] shows that σ, the root mean square displacement of the spins, essentially depends on D and on t. The diffusion coefficient is intimately related to the underlying microstructure, thus it is reasonable to hypothesize D as a valuable marker sensitive to microscopic changes. Additionally, Eq. [12] states that different aspects of the microstructure can be proved just changing the experimental settings, i.e. varying the diffusion time to achieve different values of σ within the limitation of the measurement hardware. The Gaussian solution of Eq. [11] is valid only in absence of diffusion restrictions within the average displacement achieved in the experimental diffusion time. This assumption is often violated in biological tissues due to their high compartmentalization, as further discussed in the following chapters. To conclude the overview of the diffusion process, it is worth to recall the Stokes-Einstein equation:

$$D = \mu k_B T \quad [13]$$

that shows the dependency of D on the mobility of the spins μ (thus on geometry, chemical composition), on the Stephan Boltzmann constant k_B and on the absolute temperature T. The dependence on T is an important parameter to account for, reason why experimental settings are extremely important for reproducibility and comparability of the results.

The Stejskal-Tanner diffusion sequence

Starting from the observations of Hahn (Hahn, 1950) on the Spin-Echo experiment, Carr and Purcell (Carr & Purcell, 1954) presented a modified Spin-Echo sequence with sensitization of the NMR signal to the diffusion process. In the same work, they performed the first diffusion experiment on pure water and determined its diffusion coefficient with NMR for the first time. However, the introduction of the diffusion weighted spin-echo sequence, as still used nowadays, is due to Stejskal and Tanner. In the work "Spin Diffusion Measurements: Spin Echoes in the Presence of a Time Dependent Field Gradient" (Stejskal & Tanner, 1965), they introduced the Pulsed-Gradient Spin-Echo (PGSE) scheme and derived a closed form solution to the Bloch-Torrey equation.

The schematic gradient layout of the Stejskal-Tanner Diffusion-Weighted (DW) sequence is shown in **Figure 1**. Going through the sequence, the first 90 degrees RF pulse generates an echo that it is subject to both transverse dephasing (T_2) and additional spin-spin interaction (T_2^*) that cause additional signal loss. The second 180 degrees RF pulse, that is applied after a time $T_E/2$, refocuses the signal and produces a T_2^* free signal an additional time $T_E/2$. The diffusion weighting is achieved with two identical spatial gradients around the 180 degrees pulse (READOUT line in **Figure 1**). In absence of diffusion, the spins follow a pure random walk and thus no net displacement vector can be observed. Conversely, in presence of a diffusion process the spin population will be characterized by a net displacement (Δx). The de-phasing caused by two diffusion gradients with amplitude G and duration δ in presence of net displacement of the spins caused by diffusion is:

$$\Delta\phi = \int_0^{\delta} \gamma G x_1 - \int_0^{\delta} \gamma G x_2 = \gamma G \Delta x \qquad [14]$$

It is clear that if Δx is not null, the total magnetization is reduced and thus in presence of diffusion the measured spin-echo signal is attenuated.

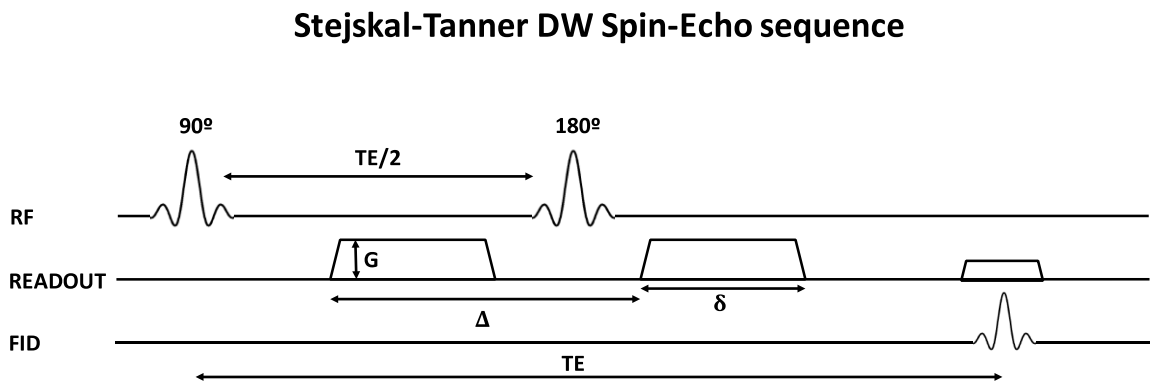

Figure 4 Schematic layout of the Stejskal-Tanner diffusion weighted Spin-Echo sequence. The addition of two gradients with amplitude G, duration δ and inter-gradients time Δ sensitizes the signal to molecular motion.

Stejskal and Tanner derived the analytical signal equation for a DW Spin-Echo experiment with diffusion gradients of amplitude G, duration δ and inter-gradients time Δ. Their derivation started from the Torrey equation (Torrey, 1956), that adds the diffusion term to the Bloch equations:

$$dM/dt = \gamma MxB + \nabla D \nabla M \qquad [15]$$

where B is the static magnetic field, M the magnetization vector, t is the time, γ the gyromagnetic ratio and D the diffusion coefficient. The solution to Eq. [15] is:

$$\frac{S}{S_0} = e^{-\gamma^2 G^2 \delta^2 (\Delta - \delta/3) D} \quad [16]$$

where S and S_0 design the signals acquired respectively with and without diffusion gradients but identical echo time. Eq. [16] can be rewritten with a more commonly used symbolism:

$$\begin{cases} S = S_0 e^{-bD} \\ b = \gamma^2 G^2 \delta^2 (\Delta - \delta/3) \end{cases} \quad [17]$$

The term b is named b-value, has unit [s/mm^2], and conveniently summarizes the contribution of the three gradient parameters (G,δ,Δ) on the measured diffusion signal.

Diffusion MRI became an imaging technique in the mid-80s after the pioneering works of Le Bihan and collegues (D Le Bihan et al., 1986; Denis Le Bihan & Breton, 1985). In the first work, "Imagerie de diffusion in vivo par résonance magnétique nucléaire", the combination of a Stejskal-Tanner diffusion sensitized sequence with imaging gradients was introduced. It was only after the collaboration of Le Bihan and Turner that the Stejskal-Tanner Spin-Echo sequence was combined with 2D Echo-Planar Imaging (EPI) (Schmitt, Stehling, & Turner, 1998; Turner, Le Bihan, & Chesnick, 1991), as schematized in **Figure 5**, greatly reducing acquisition time and imaging artifacts, finally opening the road for its widespread application.

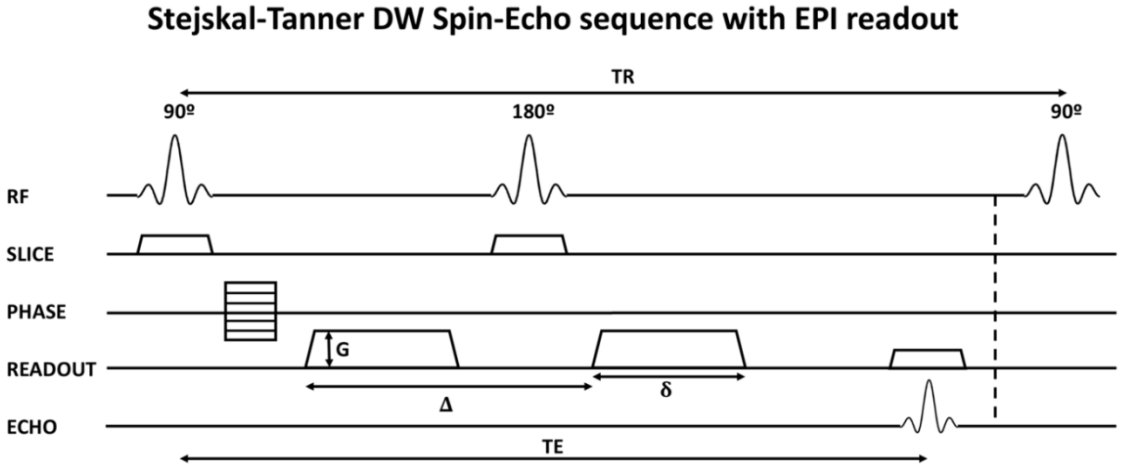

Figure 5 Schematic layout of a Stejskal Tanner diffusion weighted acquisition, that consists in the repetition of the basic Stejskal-Tanner Spin Echo with EPI readout after a time TR.

2D EPI essentially allows to acquire a 3D volume as a series of 2D images with pre-defined thickness. Specific gradients, called slice selective, are applied simultaneously to the RF

pulses along the z-axis to excite only the spins within a volume with specific z coordinate. The slice selective gradients alter the Larmor frequency of the spins along the z-axis, thus only the spins in the desired volume are in resonance with the RF pulses. To disentangle the location of the signals in-plane, additional gradients along the x-axis and the y-axis are applied (frequency and phase encoding), then the image reconstruction is performed via inverse Fast Fourier Transform. Details about the concepts of Fourier image reconstruction, EPI and k-space can be found in a comprehensive book (Brown, Cheng, Haacke, Thompson, & Venkatesan, 2014). The result of this acquisition process is a 3D matrix made of elements called voxels, each representing the module of the signal acquired at a specific spatial location.

Basic concepts of dMRI

Generally speaking, a complete diffusion experiment is essentially a series of 3D matrices, each acquired with a specific diffusion weighting, that is then fit with a specific model. The consensus on how to perform a diffusion experiment greatly varied over time especially in terms of number of diffusion weightings, number of directions and models to fit the data. Interestingly, long time after the introduction of dMRI, the research field on this topic is still very active on the optimization of each of the cited topics. In the early days of diffusion MRI, it was common practice to acquire a spin-echo volume without diffusion weighting (S_0), and three volumes with orthogonal diffusion weighting b ($S(b)$), implicitly assuming diffusion to be a direction independent (isotropic) process. A diffusion coefficient (D) was then computed for each voxel following the equations proposed by Stejskal and Tanner. Le Bihan et al. (D Le Bihan et al., 1986) proposed the name "Apparent Diffusion Coefficient" (ADC) for D to underline that it does not reflect a real measure but instead is the result of a massive averaging operation in the micron scale. Over time, the number of acquired diffusion weightings and directions grew with hardware developments to fulfill the requirements of newly proposed methods. Nowadays acquisition protocols can include more than 200 DW volumes, as will be seen in Chapter IV.

The last topic of this introduction deals with acquisition artifacts. In the following chapters different examples of acquisition schemes and quantification techniques will be shown, however, generally speaking, almost all dMRI data is affected by some common artifacts that must be recognized and, if possible, corrected. The major sources of dMRI artifacts are subject motion, eddy currents and EPI related effects (Denis Le Bihan, Poupon, Amadon, &

Lethimonnier, 2006). During the diffusion experiment multiple 3D volumes are acquired over several minutes, therefore subject motion is likely to happen and potentially alter the acquired geometry, causing misalignments between consecutive volumes, and not rarely loss of the volumes acquired during motion events. In brain acquisition motion artifacts result essentially in rigid rotations or translations, thanks to the constraining effects of the skull. The problem becomes more complex in thorax, abdomen and skeletal muscle acquisitions, where movements may result in changes of shape or size. A common and generally effective solution to this artifact is the affine registration of all acquired volumes to the first, operation that is commonly performed offline (i.e. after acquisition). Affine image registration also corrects for eddy currents artifacts, i.e. geometric distortions caused by currents self-inducted in the coils from the fast on-off switching of the strong gradients used for diffusion sensitization. In addition to post-processing corrections, a number of hardware optimizations (i.e. shielded coils, pre-emphasis of the gradients) and ad-hoc sequences (i.e. twice refocused spin echo, (Reese, Heid, Weisskoff, & Wedeen, 2003)) can be employed to mitigate Eddy currents. As mentioned above, EPI readout is one of the key reasons behind the success of dMRI, however, it comes with some drawbacks. The gradients used to perform the readout are strongly sensitive to residual magnetization that may come from eddy currents, resulting in the "N/2 ghosting" artifact, that is the repetition of the imaged object at regular intervals. The pixel bandwidth (i.e. the difference in MR frequencies between adjacent pixels) is very high in the frequency encoding direction (kHZ) but low in the phase-encoding (PE) direction (some Hz). Under these conditions, chemical shift artifacts arise: the signals of chemical compounds as fat undergo a pixel shift in the PE direction and contaminate voxels at the wrong spatial location. In dMRI only the signal originating from water molecules is generally of interest, therefore fat suppression approaches can greatly reduce this issue. The most common methods to perform fat suppression are the Spectral Pre-saturation with Inversion Recovery (SPIR) and the Spectral Attenuated Inversion Recovery (SPAIR) techniques, both based on RF pulses to suppress signals with a frequency shift of 220Hz from water (that is the main fat peak at 3T). However, these methods are not perfect and rely on very accurate B_1^+ transmit fields, thus residual fat artifacts can persist in the acquired data, especially when multiple fat species (with multiple frequency shifts from water) populate the acquired tissues. To note, this is often the case outside the brain. Finally, EPI is sensitive to B_0 field inhomogeneity. Tissue interfaces with air (as in the sinuses) or with bones result in magnetic susceptibility and thus geometric distortions. A number of approaches have been proposed to overcome this very common artifact, as B_0 field unwarping (Jezzard & Balaban, 1995) or

double acquisition with reversed phase-encoding, often called blip-up blip-down (Andersson, Skare, & Ashburner, 2003).

CHAPTER II: A DTI STUDY OF FRIEDREICH'S ATAXIA

Introduction

Diffusion MRI has found great application in the structural investigation of the brain and in particular of the white matter (WM). Diffusion Tensor Imaging (DTI) has been the gold standard quantification method of dMRI data for long time, and still is in the clinical routine context. This chapter introduces the core concepts of DTI and presents the results of a DTI based study we performed on a population affected by Friedreich's Ataxia (FRDA), a degenerative disease of the central nervous system. The results here reported have been presented as conference proceedings (Vavla et al., 2015) at the International Conference on Friedrich's Ataxia, and are now being submitted as journal paper. FRDA is the most common subtype of inherited ataxia, and is caused by an abnormal expansion of the GAA tri-nucleotide repeat in the intron 1 of the gene FXN (previously named X25) on chromosome 9 (Campuzano et al., 1996). The expansion of the GAA triplet hampers the proper unfolding of the DNA and thus the encoding of the frataxin (Campuzano et al., 1997), a protein which absence has been linked to the accumulation of iron in mitochondria and the production of free radicals, that result in cellular stress and death. The progression of the disease appears to be a dying back process from the largest and longest myelinated fibers to the brain, with the dorsal root ganglia and the cortico-spinal tracts being among the most known sites of damage (Delatycki, Williamson, & Forrest, 2000). The onset of the disease is generally before the age of 20, with progressive deficits in the motor functions, muscle weakness, sensory loss and other symptoms. The main objective of the study here presented was to obtain objective and quantitative biomarkers of FRDA from the analysis of the cerebral and cerebellar alteration patterns of patients compared to healthy controls (HC). Such analysis was performed with statistical tests of DTI metrics across groups and analysis of the correlation between MRI measures and clinical covariates in FRDA. The identification of a specific pattern of damage distinguishing FRDA from HC is expected to help the design of longitudinal studies, with particular focus on disease progression monitoring and response to treatments.

Theory

Since the first applications of dMRI, it appeared clear that diffusion weighted images (DWI) were dependent on the direction of the diffusion gradients (Moseley et al., 1990), implying that the assumption of isotropic Gaussian diffusion was not sufficient to explain the signal in

a large part of the investigated tissues. In the early 90's, Basser and collegues (Basser, Mattiello, & LeBihan, 1994; Pierpaoli & Basser, 1996) introduced the DTI technique, a three dimensional generalization of ADC that accounts for three Gaussian diffusion processes along the perpendicular spatial axis. The breakthrough of this method was the ability to describe the anisotropy and the directionality of the diffusion process with a relatively simple mathematical framework. If the diffusion gradient is applied along the direction $\mathbf{g}=[\mathbf{g_X}\ \mathbf{g_Y}\ \mathbf{g_Z}]$, equation [17] can be generalized:

$$S = S_0 e^{-b\mathbf{g}^{\mathbf{T}}\bar{D}\mathbf{g}} \qquad [18]$$

In equation [18] the term D has been replaced with $\bar{D}$, a 3x3 symmetric matrix called diffusion tensor that takes the form:

$$\bar{D} = \begin{bmatrix} D_{XX} & D_{XY} & D_{XZ} \\ D_{XY} & D_{YY} & D_{YZ} \\ D_{XZ} & D_{YZ} & D_{ZZ} \end{bmatrix} \qquad [19]$$

Six unknowns need at least six DWI measures to determine $\bar{D}$. If exactly 6 DWIs are collected, $\bar{D}$ can be computed by solution of a linear system. However, in practice, the most common way to address the problem is to collect a much larger number of DWIs and to solve the problem via Linear Least-Squares (LLS), Weighted Linear Least-Squares (WLLS) or Non-linear Least-Squares (NNLS). Solution via Least-Squares also allows to consider S_0 as an additional unknown, as suggested by a previous work (Koay, Chang, Carew, Pierpaoli, & Basser, 2006). To solve the problem with Linear Least-Squares, either weighted or non-weighted, the logarithms of both sides of Eq. [18] are considered:

$$\log(S) = \log(S_0) - b\mathbf{g}^{\mathbf{T}}\bar{D}\mathbf{g} \qquad [20]$$

After further development of the right side of the equation, some useful substitutions can be introduced:

$$X = \begin{bmatrix} 1 & b^2(\mathbf{g_X}\mathbf{g_X})_1 & b^2(\mathbf{g_Y}\mathbf{g_Y})_1 & b^2(\mathbf{g_Z}\mathbf{g_Z})_1 & b^2(\mathbf{g_X}\mathbf{g_Y})_1 & b^2(\mathbf{g_X}\mathbf{g_Z})_1 & b^2(\mathbf{g_Y}\mathbf{g_Z})_1 \\ \vdots & \vdots & \vdots & \vdots & \vdots & \vdots & \vdots \\ 1 & b^2(\mathbf{g_X}\mathbf{g_X})_n & b^2(\mathbf{g_Y}\mathbf{g_Y})_n & b^2(\mathbf{g_Z}\mathbf{g_Z})_n & b^2(\mathbf{g_X}\mathbf{g_Y})_n & b^2(\mathbf{g_X}\mathbf{g_Z})_n & b^2(\mathbf{g_Y}\mathbf{g_Z})_n \end{bmatrix}$$

$$p = [\log(S_0), -D_{XX}, -D_{YY}, -D_{ZZ}, -2D_{XY}, -2D_{XZ}, -2D_{YZ}]^{\mathrm{T}} \qquad [21]$$

$$Y = \begin{bmatrix} \log(S_1) \\ \vdots \\ \log(S_n) \end{bmatrix}$$

where n is the number of acquired DWIs.

Eq. [20] can now be expressed with a simple matrix formulation that ease its numerical implementation:

$$Y = Xp \qquad [22]$$

Consequently, p can be determined by

$$\begin{aligned} p &= (X^{\mathrm{T}}X)^{-1}X^{\mathrm{T}}Y \\ p &= (X^{\mathrm{T}}\Sigma^{-1}X)^{-1}X^{\mathrm{T}}\Sigma^{-1}Y \end{aligned} \qquad [23]$$

for LLS and WLLS respectively. Σ is a diagonal square matrix that weights each DWI into the fit. Different choices of the weights have been exploited by some works (Casaseca-de-la-Higuera et al., 2012). Even if the pre-processing step is carefully performed, dataset acquired from children or patients affected by involuntary motion can still be biased by recurrent motion artifacts. A technique to minimize their effect on the final fit is RESTORE (Chang, Jones, & Pierpaoli, 2005), that has been employed in this work along with NLLS. RESTORE is the acronym for "Robust Estimation of Tensors by Outlier Rejection, and consists in an iterative method to identify and exclude corrupted data points from the final tensor fit voxel-wise. The first step in the RESTORE pipeline is the weighted NNLS fit, using a diagonal weighting matrix initialized with the reciprocal of the data variance. The goodness of fit is then computed by means of Chi-Square (χ^2):

$$\begin{aligned} \chi^2 &= \sum_i \omega_i \times (Y_i - Xp) \\ \omega_i &= \frac{1}{\sigma^2} \end{aligned} \qquad [24]$$

If the goodness of fit criteria is not satisfied, i.e. χ^2 is greater than a certain threshold, an iterative estimate – reweight procedure is performed until the criteria is satisfied. In particular, the weights are updated using the Geman-McClure M-estimator in conjunction with the median absolute deviation of the residuals. When convergence is met, all data points corresponding to residuals outside 3 standard deviations of the data noise are rejected, then a final NNLS fit with constant weights as in Eq. [24] is performed.

The 25 years long success of DTI has been certainly supported by its affordable mathematical formulation and the relatively low acquisition demand (7+ DWIs, less than 4 minutes with

modern scanners). However, the introduction of rotation invariant metrics (Basser & Pierpaoli, 1996) computed from the eigenvectors/eigenvalues decomposition of the diffusion tensor has certainly been its workhorse. The most common metrics are "Mean Diffusivity" (MD), "Axial Diffusivity" (AD), Radial Diffusivity (RD) and "Fractional Anisotropy" (FA). MD, AD and RD share the unit measure of the three eigenvalues, that is mm^2/s. Differently, FA is unit less and quantifies the concept of anisotropy, assuming values between 0, for perfect isotropy, and 1, for full anisotropy. Named λ_1, λ_2, λ_3 the three eigenvalues in descending order, and L_1, L_2, L_3 the corresponding eigenvectors, the aforementioned metrics are defined as follows:

$$\mathrm{MD} = (\lambda_1 + \lambda_2 + \lambda_3)/3 \quad [25]$$

$$\mathrm{AD} = \lambda_1 \quad [26]$$

$$\mathrm{RD} = (\lambda_2 + \lambda_3)/2 \quad [27]$$

$$\mathrm{FA} = \sqrt{\frac{3((\lambda_1 - \mathrm{MD})^2 + (\lambda_2 - \mathrm{MD})^2 + (\lambda_3 - \mathrm{MD})^2)}{2(\lambda_1^2 + \lambda_2^2 + \lambda_3^2)}} \quad [28]$$

Pajevic and Pierpaoli (Pajevic & Pierpaoli, 1999) introduced a practical and successful representation of L_1 as Direction Encoded Colors (DEC), that consists in assigning the x, y and z components weighted by FA to the red, green and blue channel respectively. As L_1 represents the dominant fiber direction in the DTI framework, its visual inspections is of great interest. This convenient representation, shown in **Figure 6** next to FA and MD, has been useful in a number of applications to show abnormal fiber directions in pathology.

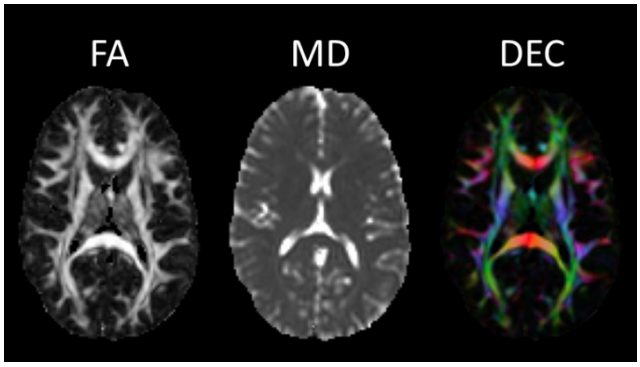

Figure 6 Examples of a FA, MD and DEC map obtained on a HC included in this study. FA and DEC are shown in the 0-1 intensity range, MD between 0 and $3.0\mu m^2/ms$ .The DEC map represents the main fiber direction weighted by FA using the color convention that assigns left-right to red, antero-posterior to green and bottom-top to blue.

Data & Methods

Eighteen healthy controls (HC) and twenty-one patients affected by Friedrich's Ataxia underwent an MRI session at IRCCS E. Medea (Bosisio Parini, Italy) with a 3T Achieva dStream Scanner (Philips Medical Systems) equipped with a 32 channels head coil. FRDA was genetically determined on all patients included in this study with molecular diagnosis. The HC group included 11 females and 7 males, and had age 27±9 years (mean ± standard deviation). The FRDA group included 16 females and 5 males with age 27±10 years. The acquisition protocol featured the following sequences:

- a 3D T_1-weighted (T_{1W}) high resolution scan based on Fast Field Echo (FFE), T_E=3.5ms, T_R=8ms, flip-angle 8°, voxel-size 1x1x1mm^3, SENSE factor 2, matrix size 256x256x160;
- a multi-shell dMRI acquisition featuring 15 gradient directions at b=300s/mm^2, 53 gradient directions at b=1100s/mm^2 and 8 volumes at b=0s/mm^2. Sequence settings were voxel size 2.2x2.2x2.2mm^3, T_E=100ms, T_R=8.8s, SPIR fat suppression, SENSE factor 2, matrix size 112x112x80;
- a T_2-weighted (T_{2W}) Turbo Spin Echo (TSE) fat suppressed (SPIR) scan, T_E=100ms, T_R=4.7s, voxel size 1.5x1.5x1.5mm^3, SENSE factor 2, matrix size 160x146x110.

Neurologic evaluation of the patients was performed by a trained neurologist with the "Scale for the Assessment and Rating of Ataxia" (SARA, (Subramony, 2007)), that essentially evaluates upright posture, speech and limb kinetic function (score range 0-40). dMRI data was pre-processed with Tortoise (Pierpaoli et al., 2010) to remove motion artifacts and attenuate geometric distortions due to the EPI readout and Eddy currents. Tortoise essentially achieves motion correction through a 12 degrees of freedom (DOF) registration of each DW volume to the first non-weighted volume. Additionally, the pipeline implemented in the tool takes advantage of the T_{2W} volume to effectively reduce geometric distortions through a quadratic model in the frequency encoding direction (Posterior-Anterior in this study). A warp field to move the first non-weighted volume to the T_{2W} is estimated, then it is combined with the affine transformation needed to motion correct each DW volume to perform a single final interpolation. The corrected volumes were visually inspected to ensure no artifacts were still affecting the data. Volumes with residual corruption were individually removed. The diffusion tensor was computed for each subject with the NLLS estimator implemented in Tortoise, however, the RESTORE options was used for some selected subjects that appeared

more prone to motion. Two study specific templates were built with DTI-TK (H. Zhang et al., 2007; H. Zhang, Yushkevich, Alexander, & Gee, 2006), one for HC and one for FRDA. DTI-TK takes advantage of all six tensor elements to perform the registrations, delivering more accurate spatial alignments than tools based on a single feature, especially in regions with complex fiber architecture as the brainstem. The template of the patients was non-linearly registered to the template of controls, then the transformations were concatenated to move the tensors of Ataxia affected subjects to the template space of healthy controls with a single interpolation. Finally, FA, MD, AD and RD maps were computed for each subject in the final template space. A custom atlas defining major white matter structures was built merging parts of two existing atlases, respectively the JHU DTI-based white matter atlas (Mori, Wakana, van Zijl, & Nagae-Poetscher, 2005) and the JHU probabilistic tracts atlas (Hua et al., 2008), resulting in 43 complimentary Regions of Interest (ROIs) (**Table 1**). Group comparisons between HC and FRDA were performed at voxel and ROI level with two General Linear Models (GLM). GLM analysis at ROI level was performed with in-house software written in MATLAB (The Mathworks, Natick, USA), using a 5% critical threshold with Bonferroni correction for multiple comparisons.

Voxel-wise GLMs were instead performed with the "Randomise" tool included in FSL (Winkler, Ridgway, Webster, Smith, & Nichols, 2014), setting the multiple comparison option to permutation based correction with "Threshold Free Cluster Enhancement" (TFCE) (S. M. Smith & Nichols, 2009). The first GLM expressed the dependent variable (DTI metrics) as function of diagnosis, age and sex:

$$Y = DIAGNOSIS \times \beta_1 + AGE \times \beta_2 + SEX \times \beta_3 + \beta_4 \quad [29]$$

An additional GLM analysis was performed only on FRDA subjects to elucidate effects of disease duration (DD) and summarized SARA score (tSARA) on MRI metrics. Given the correlation between age and DD (ρ=0.89), the first was excluded from the final GLM:

$$Y = SEX \times \beta_1 + DD \times \beta_2 + tSARA \times \beta_3 + \beta_4 \quad [30]$$

Table 1 – List of the ROIs used for the statistical tests of DTI metrics

Anterior thalamic radiation L	Inferior cerebellar peduncle R
Anterior thalamic radiation R	Inferior cerebellar peduncle L
Corticospinal tract L	Superior cerebellar peduncle R
Corticospinal tract R	Superior cerebellar peduncle L
Cingulum (cingulate gyrus) L	Anterior limb of internal capsule R
Cingulum (cingulate gyrus) R	Anterior limb of internal capsule L
Cingulum (hippocampus) L	Posterior limb of internal capsule R
Cingulum (hippocampus) R	Posterior limb of internal capsule L
Forceps major	Anterior corona radiata R
Forceps minor	Anterior corona radiata L
Inferior fronto-occipital fasciculus L	Superior corona radiata R
Inferior fronto-occipital fasciculus R	Superior corona radiata L
Inferior longitudinal fasciculus L	Posterior corona radiata R
Inferior longitudinal fasciculus R	Posterior corona radiata L
Superior longitudinal fasciculus L	External capsule R
Superior longitudinal fasciculus R	External capsule L
Uncinate fasciculus L	Fornix (column, body, cres with stria terminalis)
Uncinate fasciculus R	Post. thalamic radiation and part of internal capsule R
Sup. Long. fasciculus (temporal part) L	Post. thalamic radiation and part of internal capsule L
Sup. Long. fasciculus (temporal part) R	
Genu of corpus callosum	
Body of corpus callosum	
Splenium of corpus callosum	

Results

Figure 7 highlights the benefits of the Tortoise pre-processing on a subject included in this study. The figure shows a comparison between non-corrected data (first row), motion corrected data (second row) and fully processed data with combined motion and T_{2W} based EPI correction (last row). The weighted residuals sum of squares (WRSS) refers to an NNLS fit of the data, and proves that motion correction consistently enhances the tensor fit and results in lower residuals. The first column reports the non-weighted image estimated from the tensor fit with the undistorted contour of the brain overlaid in blue (derived from the T_{2W} image). EPI correction is clearly effective both in the frontal and occipital lobes, and improvements can be observed also in the center of the brain, for example at the cortico-spinal tracts on the fiber encoded T_{1W} (FET_1, DEC map overlaid on the T_{1W}).

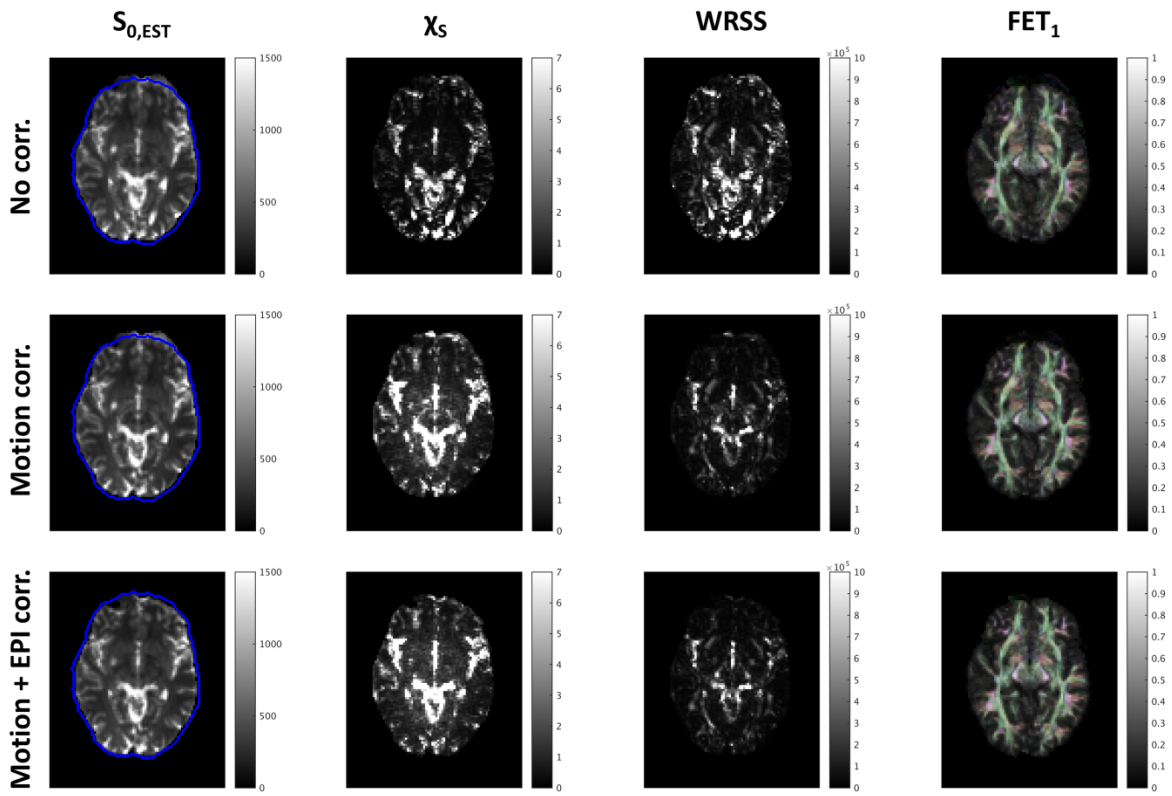

Figure 7 – Example of 3 pre-processing methods on the DTI fit of a HC data (included in this study). The first column shows the estimated non-weighted image with the non-distorted brain boundary in solid blue (derived from the T_{2W}), the second and third columns show respectively the χ_S value and the weighted sum of the residuals (WRSS), while the last column shows a fusion of the T_{1W} image and of the DEC map. The first row refers to no pre-processing, the middle to motion correction only, the last to combined motion and EPI distortions correction with Tortoise. The complete correction recovers the correct brain boundaries, shows a χ_S with less anatomical details than the other two, and results in the lowest WRSS values. Additionally, a higher correspondence to the T_{1W} image can be seen in the last column.

Results of the voxel-wise analysis performed with GLM in Eq. [29] are reported in **Figure 8** for some representative axial slices. Voxels where FRDA had statistically significant lower FA or higher MD/AD/RD values compared to HC are highlighted in red. Visual inspection of the main affected areas revealed a major involvement of the inferior and superior cerebellar peduncles, cerebral white matter, bilateral cortico-spinal tracts, bilateral optic radiations, corpus callosum and subcortical matter of pre-central and post-central gyri.

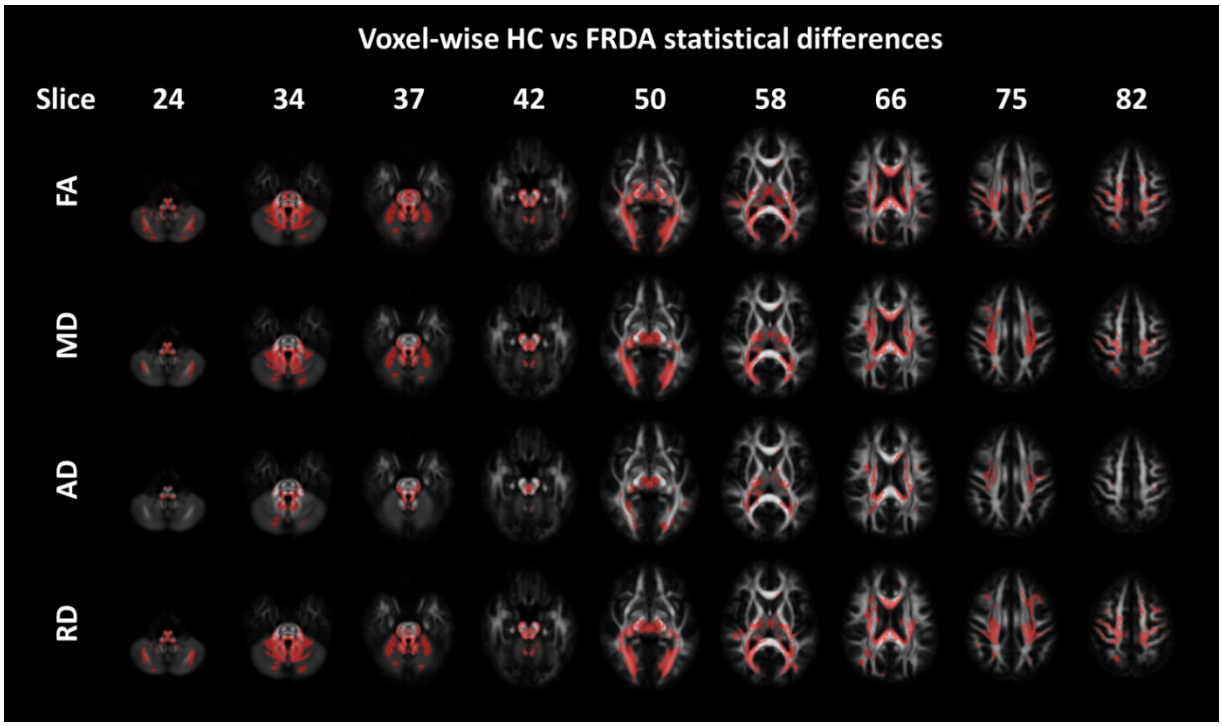

Figure 8 FA, MD, AD and RD voxel-wise differences between HC and FRDA are shown in red over an average FA map of HC. Most of the differences in FA are explained by increments of RD rather than AD, and are mainly located in the cerebellar white matter, cortico-spinal tracts and corpus callosum.

Reductions of FA are often (but now always) linked to increments of MD, due to the relations between the eigenvalues, however inspection of AD and RD maps revealed that the latter was the prominent cause of MD increments. The ROI analysis resulted in similar observations, with major involvement of the cerebellar white matter, cortico-spinal tracts and corpus callosum, as reported in **Table 2**. Only the diagnosis resulted to be a significant predictor of difference between the two groups, therefore the comparison could be essentially performed with a corrected two-sided t-test. Investigation of the covariates in the FRDA group using GLM in Eq. [30] resulted in no covariate being significant at voxel level, eventually due to an insufficient number of subjects, especially in consideration of the severe multiple comparison correction for the whole brain.

Table 2 Results of the GLM analysis of FA, AD, MD and RD between HC and FRDA, considering age and sex as covariates. Bold p-values are considered significant (less than 0.05).

Structure	Mean (HC)	Std (HC)	Mean (FRDA)	Std (FRDA)	Age (p-val)	Sex (p-val)	Group (p-val)	Age (β)	Sex (β)	Group (β)	Variation %
GLM Eq. [29] of FA											
Corticospinal tract L	0,516	0,024	0,478	0,032	0,745	0,916	**<0,001**	0,000	-0,001	**-0,038**	-7,38
Corticospinal tract R	0,510	0,026	0,467	0,030	0,605	0,870	**<0,001**	0,000	-0,002	**-0,043**	-8,46
Forceps major	0,506	0,030	0,447	0,032	0,302	0,149	**<0,001**	-0,001	0,017	**-0,063**	-11,83
Body of CC	0,627	0,042	0,574	0,046	0,937	0,907	**0,001**	0,000	0,002	**-0,054**	-8,56
Splenium of CC	0,654	0,030	0,614	0,031	0,406	0,510	**<0,001**	0,000	0,008	**-0,041**	-6,06
Inferior cereb. peduncle R	0,501	0,035	0,390	0,031	0,881	0,148	**<0,001**	0,000	-0,018	**-0,109**	-22,24
Inferior cereb. peduncle L	0,497	0,044	0,395	0,034	0,556	0,053	**<0,001**	0,000	-0,027	**-0,098**	-20,46
Superior cereb. peduncle R	0,550	0,040	0,369	0,042	0,105	0,838	**<0,001**	0,001	-0,003	**-0,180**	-32,95
Superior cereb. peduncle L	0,537	0,039	0,349	0,037	0,106	0,956	**<0,001**	0,001	-0,001	**-0,187**	-34,95
MCP and pontine cross. tract	0,490	0,027	0,453	0,031	0,732	0,520	**0,001**	0,000	-0,007	**-0,035**	-7,47
Post. thalamic r. and PLIC R	0,561	0,029	0,517	0,033	0,346	0,959	**<0,001**	-0,001	0,001	**-0,044**	-7,835
Post. thalamic r. and PLIC L	0,560	0,032	0,515	0,034	0,411	0,774	**<0,001**	0,000	0,004	**-0,046**	-8,044
GLM of MD ($mm^2/s \times 10^3$)											
Corticospinal tract R	2,187	0,125	2,356	0,169	0,175	0,539	**0,001**	0,004	-0,034	**0,175**	7,71
Forceps major	2,496	0,203	2,786	0,238	0,682	0,028	**<0,001**	0,002	-0,179	**0,317**	11,59
Splenium of CC	2,453	0,175	2,703	0,197	0,929	0,382	**<0,001**	0,000	-0,062	**0,260**	10,22
Inferior cereb. peduncle R	2,164	0,203	2,607	0,226	0,186	0,199	**<0,001**	-0,005	0,102	**0,426**	20,48
Inferior cereb. peduncle L	2,190	0,180	2,605	0,210	0,088	0,147	**<0,001**	-0,006	0,104	**0,398**	18,97
Superior cereb. peduncle R	2,984	0,286	4,099	0,409	0,207	0,512	**<0,001**	-0,008	0,087	**1,099**	37,36
Superior cereb. peduncle L	3,065	0,342	4,400	0,313	0,350	0,877	**<0,001**	-0,005	-0,019	**1,336**	43,55
Middle cereb. peduncle and pontine cross. tract	2,066	0,130	2,289	0,178	0,394	0,550	**<0,001**	-0,002	0,035	**0,217**	10,81
Post. thalamic r. and PLIC R	2,165	0,153	2,363	0,183	0,672	0,359	**0,001**	0,001	-0,059	**0,207**	9,14
Post. thalamic r. and PLIC L	2,209	0,135	2,407	0,206	0,964	0,262	**0,001**	0,000	-0,074	**0,209**	8,96
GLM of AD ($mm^2/s \times 10^3$)											
Superior cereb. peduncle R	1,646	0,093	1,865	0,117	0,380	0,435	**<0,001**	-0,002	0,031	**0,214**	13,32
Superior cereb. peduncle L	1,667	0,131	1,958	0,088	0,735	0,841	**<0,001**	-0,001	-0,008	**0,291**	17,42
Middle cereb. peduncle and pontine cross. tract	1,087	0,049	1,157	0,058	0,224	0,424	**0,001**	-0,001	0,016	**0,068**	6,49
GLM of RD ($mm^2/s \times 10^3$)											
Corticospinal tract L	0,496	0,036	0,551	0,056	0,193	0,330	**0,001**	0,001	-0,017	**0,058**	11,16
Corticospinal tract R	0,509	0,040	0,575	0,056	0,087	0,597	**<0,001**	0,002	-0,009	**0,068**	13,04
Forceps major	0,570	0,069	0,682	0,082	0,490	0,033	**<0,001**	0,001	-0,060	**0,121**	19,56
Body of CC	0,447	0,066	0,552	0,092	0,789	0,816	**<0,001**	0,000	-0,007	**0,106**	23,63
Splenium of CC	0,465	0,057	0,553	0,063	0,655	0,361	**<0,001**	0,000	-0,021	**0,091**	18,86
Inferior cereb. peduncle R	0,505	0,064	0,682	0,074	0,336	0,183	**<0,001**	-0,001	0,035	**0,171**	35,05
Inferior cereb. peduncle L	0,514	0,063	0,679	0,070	0,269	0,091	**<0,001**	-0,001	0,042	**0,158**	32,15
Superior cereb. peduncle R	0,669	0,100	1,117	0,150	0,167	0,560	**<0,001**	-0,003	0,028	**0,443**	66,92
Superior cereb. peduncle L	0,699	0,111	1,221	0,119	0,245	0,902	**<0,001**	-0,002	-0,005	**0,522**	74,73
Middle cereb. peduncle and pontine cross. tract	0,490	0,042	0,566	0,060	0,516	0,628	**<0,001**	-0,001	0,010	**0,075**	15,60
Post. thalamic r. and PLIC R	0,469	0,048	0,543	0,059	0,479	0,409	**<0,001**	0,001	-0,017	**0,077**	15,84
Post. thalamic r. and PLIC L	0,480	0,045	0,557	0,066	0,668	0,313	**<0,001**	0,000	-0,022	**0,081**	16,08

At ROI level, sex and tSARA were significant predictors of FA, MD and RD in the left internal capsule, and could significantly predict MD and RD in the posterior thalamic radiation. Details on the estimated effects can be found in **Table 3**.

Table 3 – Results of the GLM analysis in the FRDA group including DD, tSARA and sex. Bold p-values are considered significant (less than 0.05).

Structure	Mean	Std	Sex (p-val)	DD (p-val)	tSARA (p-val)	Sex (β)	DD (β)	tSARA (β)
GLM Eq. [30] of FA								
Anterior limb of internal capsule L	0,447	0,032	**0,047**	0,739	**0,004**	0,026	0,000	**-0,001**
GLM of MD ($mm^2/s \times 10^3$)								
Anterior limb of internal capsule L	2,786	0,238	**0,026**	0,701	**0,035**	**-0,249**	-0,002	**0,007**
Post. thalamic r. and PLIC L	2,703	0,197	**0,167**	0,689	**0,048**	**-0,133**	-0,002	**0,006**
GLM of RD ($mm^2/s \times 10^3$)								
Anterior limb of internal capsule L	0,682	0,082	**0,019**	0,835	**0,016**	**-0,085**	0,000	**0,003**
Post. thalamic r. and PLIC L	0,553	0,063	0,111	0,767	**0,025**	-0,047	-0,001	**0,002**

PLIC is the "Posterior Limbo of Internal Capsule". Post. Thalamic r. is the Posterior Thalamic Radiation.

DD was not significant in any of the evidenced regions, while gender was a useful predictor and showed significantly lower values for females (gender was a binary variable with Sex=1 for females). Interestingly, the functional score tSARA correlated positively with MD and RD, but negatively with FA. Being tSARA an inverse scale, where 0 corresponds to perfect functionality and 40 to complete impairment, this is in line with previous findings of lower FA and higher MD values in disease progressions.

Conclusions

We performed an explorative DTI study to investigate white matter alterations in a population affected by FRDA. Accurate pipelines available for DTI analysis were employed throughout the processing steps to achieve the highest statistical power given the limited sample size included in this study. We found major white matter alterations in the cerebellum, in the cortico-spinal tract and in the corpus callosum, areas that comply with the motor impairment and the symptoms that characterize the disease. The general trend that could be observed on the voxel-wise differences maps was a reduction of FA, linked to an increment of RD in the patients group. Previous studies with DTI have linked increased RD but almost constant AD values to myelin related impairments more than axonal inflammation (Aung, Mar, & Benzinger, 2013), situation that may be compatible with the etiology of FRDA. In addition to group comparisons, the correlation between DTI metrics and clinical covariates were evaluated. The GLM analysis showed that the functional scale tSARA

correlated with DTI metrics in the left interior capsule and thus part of the left cortico-spinal tract. These findings corroborate the idea of MRI and in particular of dMRI as tools to monitor microstructural damage over multiple stages of the disease.

CHAPTER III: CHARACTERIZATION OF THE TEMPORAL LOBE IN MULTIPLE SCLEROSIS PATIENTS WITH NODDI.

Introduction

During the last decade several studies have proposed novel ways to fit the dMRI signal and extract measures related to the biophysical substrate. Established techniques as ADC or DTI can be regarded as statistical models to describe the diffusion process, reason why they can be ideally applied to any biological tissue. In contrast, biophysical models describe the diffusion signal by accurate modeling of the tissue microstructure, combining observations from different fields, as microbiology and histology. They can be applied only to the specific tissue they have been designed for, but ideally provide biologically relevant and interpretable measures. A number of different models has been proposed to fit the diffusion signal in the brain, as for example ActiveAx (Alexander et al., 2010), AxCaliber (Assaf, Blumenfeld-Katzir, Yovel, & Basser, 2008), CHARMED (Assaf & Basser, 2005) and the "Neurite Orientation Dispersion and Density Imaging" (NODDI) (H. G. Zhang, Schneider, Wheeler-Kingshott, & Alexander, 2012). Among all these models, NODDI recently gained popularity not only in technical research but also in clinical studies, being the first to provide an intuitive biophysical description within clinically acceptable acquisition requirements. This chapter introduces the main concepts behind the NODDI model and presents an application of NODDI to monitor temporal lobe damage in Multiple Sclerosis (MS) we performed in collaboration with the MS Centre of Verona University Hospital (M Calabrese et al., 2016).

Multiple sclerosis is a degenerative disorder of the brain and of the spinal cord, characterized by progressive demyelination of the axons as result of inflammation processes (Compston & Coles, 2008). The disease is categorized "relapsing-remitting" (RRMS), when damage occurs during acute episodes followed by incomplete recovery and thus impairment accumulation over time, or progressive, with continuous tissue damage over time. Additional classifications of MS subtypes can be made between primary and secondary MS, as exemplified in **Figure 9**.

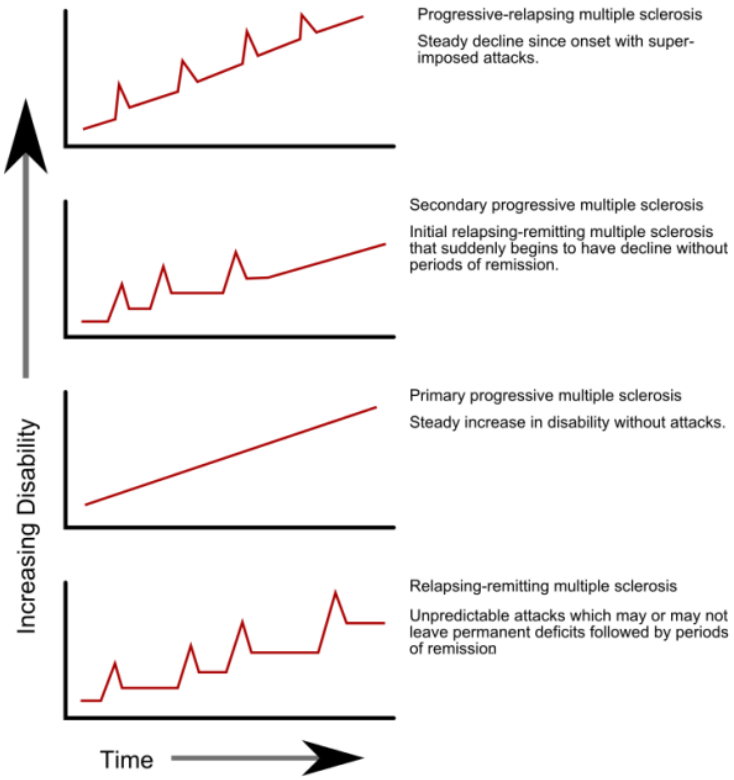

Figure 9 Four subtypes of multiple-sclerosis characterized by different progression over time.

The origin of MS remains unknown, however, it has been hypothesized to be an autoimmune disease triggered by environmental factors in individuals with genetic risk profiles. The immune system appears to have a key role, with abnormal migration of lymphocytes across the blood brain barrier, accumulation of macrophages and inflammatory cytokines in the sites of activation. MRI is a fundamental tool in MS diagnosis (Polman et al., 2005). Lesions appear with hyper-intense signal in T_{2W} images in their early stages, due to the longer T_2 time of fluids compared to tissues. Additional specificity in the differentiation of lesions may be achieved by inspection of the "black-holes" in T_{1W} images (Sahraian, Radue, Haller, & Kappos, 2010). In the past MS was considered a white matter disease, however, recent studies have proved that inflammation and damage occur also in gray matter (GM) and that GM lesions are a prominent cause of disability (Massimiliano Calabrese, Rinaldi, et al., 2010, 2010; Massimiliano Calabrese, Rocca, et al., 2010; Massimiliano Calabrese, Filippi, & Gallo, 2010; Rinaldi et al., 2010). In the current context of MS studies, it has been observed that epilepsy prevalence in MS patients is 3 times higher than in the normal population. However, the link between GM damage and epilepsy is not well known, despite previous studies on the topic (Massimiliano Calabrese et al., 2008; Truyen et al., 1996). The purpose of this study is

to further investigate this phenomenon with a comprehensive MRI protocol that includes a multi-shell dMRI acquisition.

Theory

DTI has been largely applied to study WM in MS studies. However, in this study we chose to employ the NODDI model in place of DTI following two main observations. Firstly, DTI can well describe the dMRI signal in WM with single fiber population, however, it lacks of specificity when applied to GM. The cortex is mainly populated by cell bodies and randomly oriented dendrites, that result in low apparent FA values with consequent low specificity of MD, AD and RD. Moreover, only data acquired in a specific and tissue dependent range of diffusion weightings can be appropriately fit with DTI. At strong diffusion weightings (i.e. above b=1500s/mm^2 in the brain) the contribution of membrane restrictions or water pools characterized by very slow diffusivity to the diffusion signal becomes prominent, and the signal deviates from the expected Gaussian decay (hence the name non-Gaussian diffusion). The NODDI framework explicitly models some of the main components of the brain tissue, as cell bodies, neurites and free water, and should thus provide more specific measurements. Additionally, NODDI can deal (and requires) data acquired both at low (in this study b=700s/mm^2) and strong (in this study b=2000s/mm^2) diffusion weighting. The need for more data than DTI results in prolonged acquisition time, but potentially delivers more information about the diffusion process. Three independent compartments without exchange are used to model the brain tissue in the NODDI framework: an isotropic diffusion compartment (ν_{iso}), that mainly accounts for the Cerebro-Spinal Fluid (CSF) or interstitial water outside cells, an intra-neurite compartment (ν_{ic}) to represent highly anisotropic structures as axons and dendrites, and an extra-neurite compartment (ν_{ec}) to account for hindered / tortuous diffusion of cell bodies (glia, macrophages, etc.). The general equation that summarizes the relation between the three compartments and the measured signals is:

$$S = S_0\left(\nu_{\text{iso}}S_{\text{iso}} + (1-\nu_{\text{iso}})(\nu_{\text{ic}}S_{\text{ic}} + \nu_{\text{ec}}S_{\text{ec}})\right) \quad [31]$$

subject to the constraint $\nu_{\text{ec}} = 1 - \nu_{\text{ic}}$. The normalized signals of the three compartments are defined as follows:

$$S_{\text{iso}} = e^{-b\cdot 3\text{x}10^{-3}} \quad [32]$$

$$S_{\mathrm{ic}} = \int f(\mathbf{n}) e^{-b d_{\parallel} (\mathbf{g}\cdot\mathbf{n})^2} \mathrm{d}\mathbf{n} \quad [33]$$

$$S_{\mathrm{ec}} = e^{-b\mathbf{g}^{\mathrm{T}} (\int f(\mathbf{n}) D(\mathbf{n}) \mathrm{d}\mathbf{n}) \mathbf{g}} \quad [34]$$

The formulation of the isotropic compartment follows a simple isotropic Gaussian decay with diffusion constant equal to that of water at 37 degrees. One of the innovations of the NODDI framework is the introduction of a spatial distribution function $f(\mathbf{n})$ to modulate Gaussian tensor-based decays. The simplest choice for $f(\mathbf{n})$ is the Watson distribution:

$$f(\mathbf{n}) = M\left(\frac{1}{2}, \frac{3}{2}, \kappa\right) e^{\kappa(\boldsymbol{\mu}\cdot\mathbf{n})^2} \quad [35]$$

where M references a confluent hyper-geometric function, and κ quantifies the orientation dispersion around the mean direction ($\boldsymbol{\mu}$) for each gradient direction ($\mathbf{n}$). A final note regards the diffusion tensors used in S_{ic} and S_{ec}: the first has only an axial (parallel) diffusion coefficient $d_{\parallel}$ and no perpendicular diffusivity, describing a zero-radius cylinder as done in a previous study (Behrens et al., 2003), while the latter constrains the perpendicular diffusivity to depend on the parallel through a tortuosity model (Szafer, Zhong, Anderson, & Gore, 1995). More details on the implementation of S_{ic} and S_{ec} can be found in to the original NODDI paper of Zhang et al. (H. G. Zhang et al., 2012). The basic NODDI framework has 4 degrees of freedom, given by the free parameters ν_{ic}, ν_{iso}, κ, μ, while $d_{\parallel}$ and d_{iso} are fixed to 1.7×10^{-3}mm^2/s and 3.0×10^{-3}mm^2/s respectively. Optionally, the framework allows to fit also the non-weighted signal S_0. κ is lower bounded to 0 but upper unbounded, therefore it is often replaced by the Orientation Dispersion (OD) parameter:

$$\mathrm{OD} = \frac{2}{\pi}\arctan\left(\frac{1}{\kappa}\right) \quad [36]$$

Differently from other frameworks as DTI, the NODDI fit does not rely on NLLS but instead on the minimization of a Rician Maximum Likelihood function (*RML*) that includes the measurement noise in the formulation (Sijbers & den Dekker, 2004):

$$RML = 2\log(\sigma^2) - \frac{S^2 + E^2}{2\sigma^2} + \log(S) + \mathrm{I}_0\left(\frac{S \cdot E}{\sigma^2}\right) \quad [37]$$

where S comes from the equation [31], E is the measured signal, σ is the noise standard deviation and I_0 the modified zero-order Bessel function.

Data & Methods

Twenty-three RRMS patients with epileptic seizures (RRMS/E) and twenty-three RRMS control patients without any story of seizures underwent MRI with a 3T Philips Achieva (Philips Medical Systems) at the MS Centre of Verona University Hospital. Only patients with seizures that could be explained by MS only were included in the RRMS/E group. Patients of both groups were diagnosed by an experienced neurologist according to the 2010 McDonald's criteria (Sadaka et al., 2012) and the Expanded Disability Status Scale (EDSS,(Kurtzke, 1983)). Seizures of the RRMS/E group were scored according to the International League against Epilepsy guidelines (Polman et al., 2011). A two shells dMRI sequence (T_E=109ms, T_R=12.5s, flip angle 90 degrees, SENSE factor 2, resolution 2x2x2mm^3, SPIR fat suppression) was acquired with 8 non-weighted volumes, 32 gradient directions at b=700s/mm^2 and 64 gradient directions at b=2000s/mm^2. Directions of both shells were evenly distributed on a half-sphere. In addition, other structural sequences were acquired for diagnosis, lesion identification and to support the dMRI pre-processing:

- 3D Fluid Attenuated Inversion Recovery (FLAIR) T_E/T_R 292/5500ms, Inversion Time (TI) 1650ms, resolution 1x1x1mm^3;
- 3D Double Inversion Recovery (DIR) T_E/T_R 292/5500ms, T_{I1} 525ms, T_{I2} 2530ms, resolution 1x1x1mm^3;
- 3D T_{1W} Fast Field Echo T_E/T_R 3.7/8.4ms, resolution 1x1x1mm^3;
- 3D T_{2W} Turbo Spin Echo (TSE) T_E/T_R 268/2600ms, resolution 1.7x1.7x1.7mm^3.

dMRI data was pre-processed with Tortoise to reduce motion, eddy currents and EPI artifacts using the T_{2W} sequence as non-distorted reference. The NODDI model was fitted on the complete 2 shells dMRI acquisitions using the MATLAB Toolbox available at http://mig.cs.ucl.ac.uk. ROIs delineating the hippocampus, the parahippocampus, superior – medial – inferior temporal gyrus, temporal pole, fusiform gyrus, cingulate gyrus and insular cortex were derived from T_{1W} data using the automated, volume based Advanced Normalization Tools (ANTs) pipeline (Das, Avants, Grossman, & Gee, 2009) and the Multi-Atlas Label Fusion (MALF) technique (H. Wang et al., 2013). The MALF approach requires a training set of labeled brains to perform the segmentation of each subject. For this purpose, we employed the dataset publicly available from the 2012 MICCAI Multi-Atlas Labeling Challenge, that consists of 30 labeled brains, that were non-linearly registered with ANTs to each patient's space. The first non-weighted image of the dMRI data was non-linearly

registered to the T_{1W} space of each subject using the T_{2W} as intermediate step to improve the registration quality. For this step, the non-linear deformation field was constrained to the phase encoding direction (Posterior-Anterior).

DIR and FLAIR images were assessed by consensus of experienced observers to compute the number of gray matter lesions (GMLs) and white matter lesions (WMLs) respectively. Group comparisons were performed to assess difference in the distributions of the covariates and clinical variables in the two groups. Differences of WMLs were tested through analysis of variance (ANOVA), while GMLs and EDSS, that were non-normally distributed, were tested through the Mann-Whitney U-Test. Difference of female/male ratio and age were tested with Pearson's chi-square. The association between the presence of seizures (binarized) and MRI derived parameters (GMLs, NODDI indices) was evaluated for each ROI using a GLM with logistic regression.

Results

Clinical variables, MRI derived covariates and the p-value of the hypothesis tests of RRMS and RRMS/E patients are reported in **Table 4**.

Table 4 Demographic and clinical variables of the RRMS and RRMS/E groups. Only EDSS and GMLs were differently distributed in the two groups.

	RRMS (N=23)	RRMS/E (N=23)	p-value
Female:male	16:7	15:8	0.100
Age (years)	42.4 ± 10.3	45.7 ± 7.8	0.290
Disease duration (years)	5.2 ± 2.4	5.5 ± 2.6	0.415
EDSS, median	1.5	3.5	<0.001
Epilepsy duration (years)	NA	4.3 ± 2.4	
WMLs	9.6 ± 4.1	10.3 ± 5.1	0.154
WML volume (cm^3)	4.1 ± 4.3	4.9 ± 4.4	0.102
GMLs	2.0	5.0	<0.001
Patients with CLs (%)	60.8%	91.3%	0.034

MRI: magnetic resonance imaging; RRMS: relapsing remitting MS; RRMS/E: RRMS with epilepsy; EDSS: Expanded Disability Status Scale; WML: T2 white matter lesions; GML: grey matter lesion. CL: Cortical Load

Age, gender and disease duration did not differ significantly among the two groups, while the EDSS score was higher for RRMS/E than RRMS. WMLs and the WML volume were also not significantly different, however, GMLs were significantly higher in the RRMS/E group. The different distribution of GMLs could be directly observed on DIR images, as shown in

Figure 10. 208 GMLs were observed in 21 out of 23 RRMS/E, while only 93 GMLs were observed in 14 out of 23 RRMS.

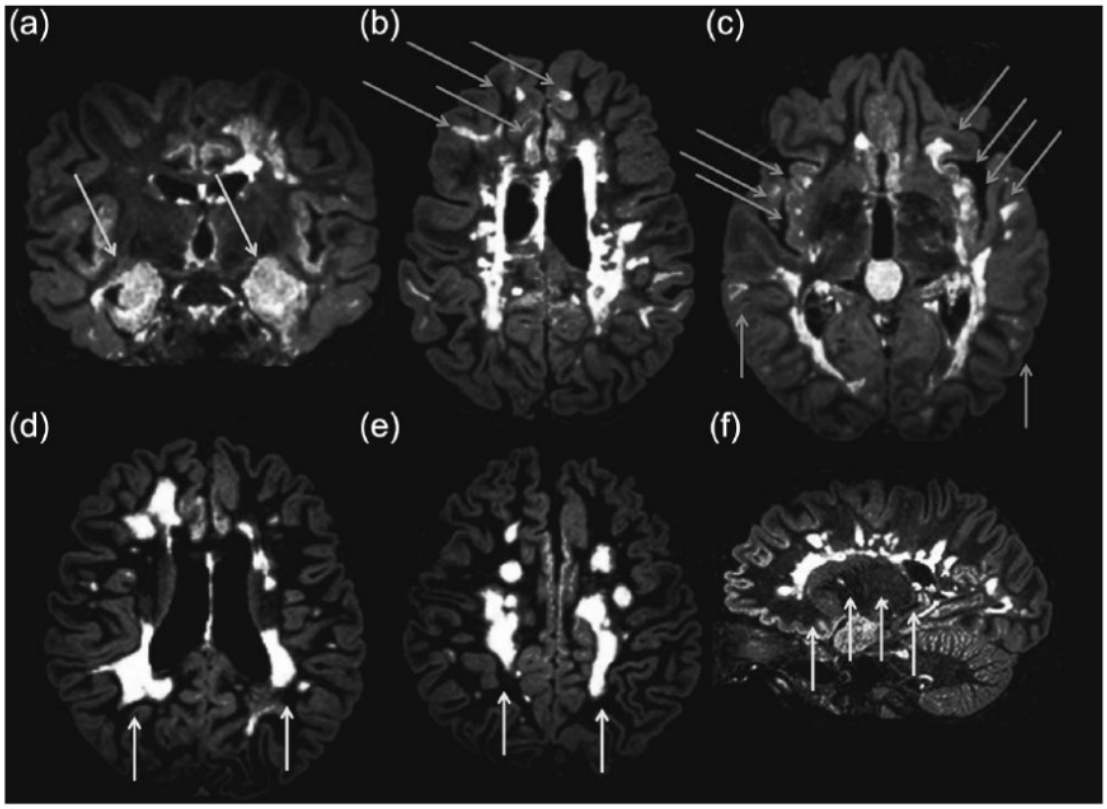

Figure 10 3D DIR of three RRMS/E (a,b,c) and three RRMS (d,e,f) patients without history of seizures. RRMS/E show severe hyppocampal demyelination (arrows, a) and several gray matter lesions (arrows,b) including insular cortex (arrows,c). RRMS patients do not show any GML withstanding the severe WML (arrows, d,e,f).

Significant statistical differences of the NODDI metrics among the two groups were found in many of the analyzed ROIs. In particular, v_{iso} was significantly higher for the RRMS/E group in all the considered regions. v_{ic} was observed to be increased (between 11.2% and 18.3%) in all ROIs of RRMS/E compared to RRMS, however p-values below 0.05 were found only in the inferior temporal gyrus and in the insular cortex. Finally, RRMS/E had higher OD values in the hippocampus, parahippocampus and insular cortex. Relative and absolute differences of the metrics in the two groups and p-values of the tests can be found in **Table 5**, while examples of NODDI maps with overlaid the cortical MALF parcellation can be seen in **Figure 11**.

Table 5 – ROIs for which statistically different NODDI indices were found among the two groups. v_{iso} was significantly different among all temporal lobe ROIs, suggesting atrophy in the RRMS/E group.

Structure	OD	p-value	v_{iso}	p-value	v_{ic}	p-value
Hippocampus	0.025 (4.9%)	0.021	0.092 (17.3%)	0.023	0.060 (10.3%)	-
Parahippocampus	0.022 (4.5%)	0.023	0.072 (14.9%)	-	0.067 (10.6%)	-
Superior temporal gyrus	0.005 (1.0%)	-	0.142 (31.2%)	0.001	0.075 (18.0%)	-
Middle temporal gyrus	0.004 (0.8%)	-	0.125 (28.9%)	0.007	0.077 (19.0%)	-
Inferior temporal gyrus	0.007 (1.5%)	-	0.124 (31.4%)	0.003	0.090 (20.6%)	0.019
Temporal pole	0.015 (3.0%)	-	0.097 (19.6%)	0.006	0.075 (16.4%)	-
Fusiform gyrus	0.013 (2.5%)	-	0.115 (30.7%)	0.017	0.080 (17.7%)	-
Cingulate gyrus	0.006 (1.3%)	-	0.114 (23.7%)	0.015	0.081 (18.6%)	-
Insular cortex	0.021 (4.2%)	0.028	0.129 (34.9%)	0.002	0.090 (19.1%)	0.041
Superior frontal gyrus	0.005 (1.0%)	-	0.120 (02.9%)	0.011	0.091 (15.5%)	0.058
Whole temporal lobe	0.012 (2.4%)	0.025	0.124 (28.6%)	0.011	0.090 (15.3%)	0.042

RRMS: relapsing remitting MS; RRMS/E: RRMS with epileptic seizures; ODI: orientation dispersion index; v_{iso} volume fraction of the isotropic compartment; v_{ic} intra-neurite volume fraction

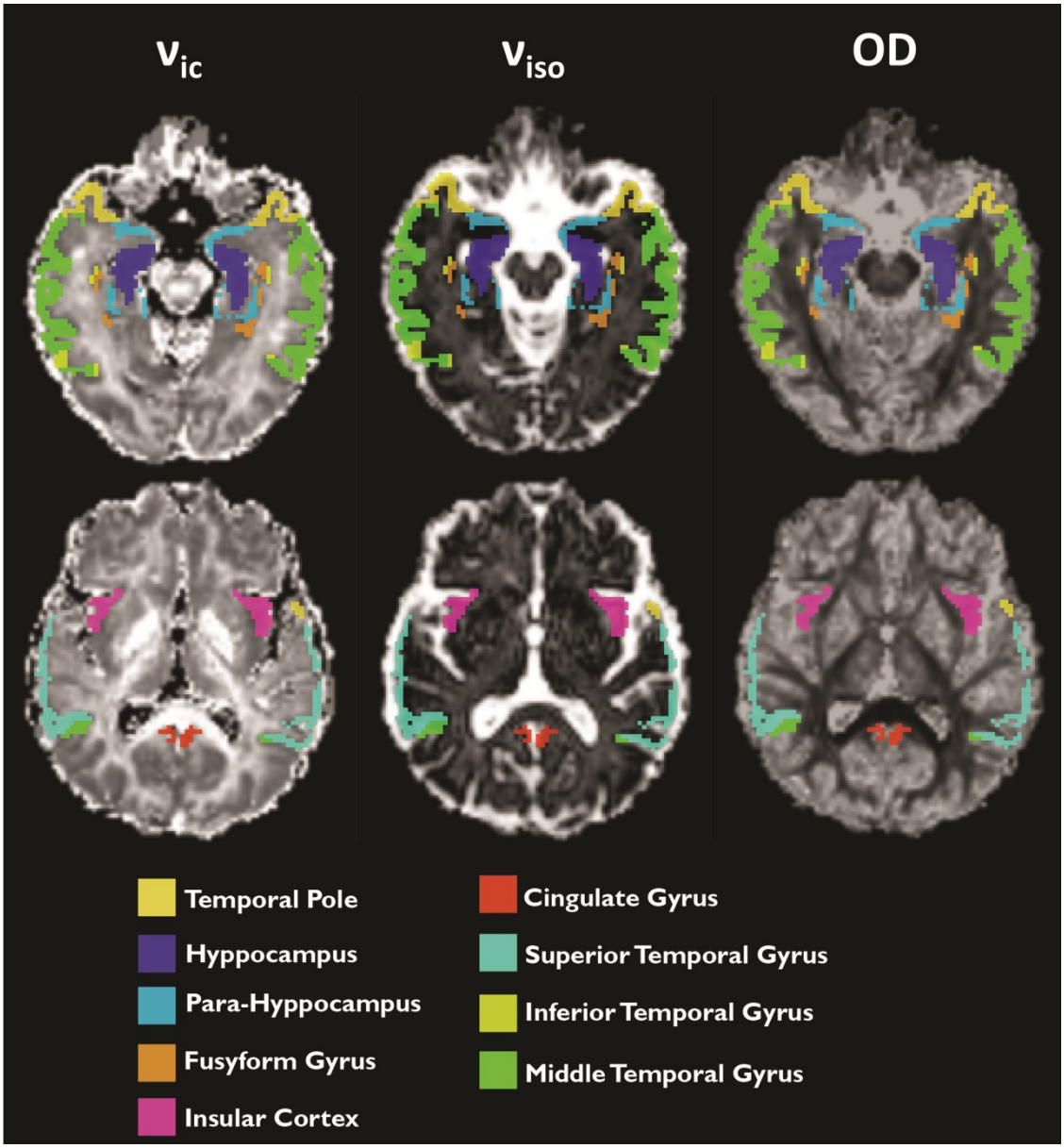

Figure 11 Example of the temporal lobe parcellation obtained with the MALF technique over-imposed on the NODDI maps Intra-Cellular Volume Fraction (v_{ic}, first column), Isotropic Volume Fraction (v_{iso}, middle column) and Orientation Dispersion (OD, last column).

Conclusions

In this study we employed the NODDI model to investigate microstructural alterations of the temporal lobe cortex in MS patients with and without epileptic seizures. Our findings suggest that patients in the RRMS/E group had a significantly higher number of gray matter lesions, as observed on DIR images. In this context, the NODDI model showed increased atrophy in the whole temporal lobe of the RRMS/E than RRMS. Indeed, the increment of v_{iso} in the RRMS/E group can be explained by an increment of free water, due to inflammation

processes, or increased partial volume effects due to atrophy. In this latter case, the consequent reduction of the cellular component, including both neurites and cell bodies, justifies the increment of the free water component. We observed higher v_{ic} values of RRMS/E compared to RRMS, values that were statistically different between the two groups in some cortical areas, implying an impaired ratio of axons over cell bodies, probably due to a reduction of the latter due to atrophy. The final observation that OD was increased in the hippocampal area supports the idea of less coherent or more demyelinated fibers in that area, consistently with observations on DIR images. Biophysical models as NODDI open a new perspective on the applicability of dMRI to the investigation of GM in clinical studies. Although these techniques require the acquisition of more data and have a more complex mathematical formulation than DTI, they potentially provide metrics that are more specific, pushing the field toward the definition of microstructure specific indices.

CHAPTER IV: TISSUE SPECIFIC MODELING WITH SPHERICAL DECONVOLUTION

Introduction

In Chapter III it was observed that DTI is well suited to describe dMRI signals of a single fiber population (i.e. a single dominant anisotropic structure) and within diffusion weightings where the Gaussian assumption holds. However, recent evidence showed that a large part of white matter contains two or even three major fiber orientations (Jeurissen, Leemans, Tournier, Jones, & Sijbers, 2013), that are characterized by a number of geometrical configurations, as branches, kisses, intersections (**Figure 12**).

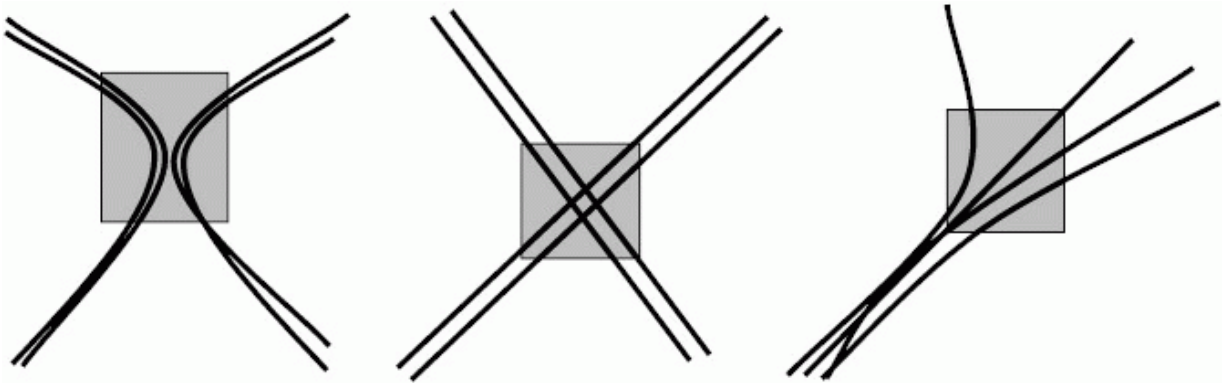

Figure 12 Example of fibers configurations that cannot be properly modeled with the DTI framework. Kissing fibers are shown on the left, crossing fibers in the middle, diverging/converging fibers on the right.

Additionally, the acquisition and interpretation of data at strong diffusion weighting may benefit the investigation of complex multi domain tissues as gray matter, but also the detection of multiple fiber orientations in white matter (Dell'acqua et al., 2005). This chapter deals with a method, presented as conference proceedings at ISMRM 2015, to segment brain tissues based on their specific diffusivity properties, then shows its application to healthy controls and a patient affected by MS (Alberto De Luca et al., 2015b). The idea behind this method was inspired partly from the NODDI formulation and partly from a model-free technique, the Multi-Shell Multi-Tissue approach (MSMT,(Jeurissen, Tournier, Dhollander, Connelly, & Sijbers, 2014)). The model-free approach offers a number of advantages over classic multi-compartment models, as it relies on very few assumptions about the underlying tissues. However, with such approaches it is generally difficult to derive biophysically meaningful parameters. The model that we developed describes the brain tissue with three

compartments, each devoted to one of the main tissue types found in the brain, but uses ideas from the MSMT approach to reduce the number of estimated parameters and their uncertainty.

Theory

Spherical Deconvolution (SD) is an approach alternative to multi-compartment models to describe the diffusion signal. Instead of providing an explicit model that is fit with Least-Squares or similar approaches, SD requires the construction of a dictionary matrix of size *n*x*p*, where *n* is the number of acquired DWIs and *p* the number of entries in the dictionary. The technique essentially consists in finding the linear combination of the columns of the dictionary that best explains the measured signal. Denoting with *S* the measured signal, with U the dictionary matrix and p the amplitude of the columns of U (deconvolution vector), the general formulation of SD is:

$$S = \mathrm{U}\mathrm{p} \qquad [38]$$

$$\mathrm{p} = \mathrm{U}^{-1}S \qquad [39]$$

The major difference with model fit approaches is that no assumptions are made about the number of signal components and no parameters are estimated, but only the relative amplitudes of the columns of U. For this reason, SD is often regarded as a model-free approach. However, this nomenclature should be interpreted with caution, as the columns of U may be generated with parametric or geometric models that still require the tuning of some parameters. The first application of SD in the human brain in conjunction with the diffusion tensor was proposed by Dell'Acqua and colleagues (Dell'acqua et al., 2005), where the authors used the DTI model to generate the columns of U. Tournier and colleagues (J-Donald Tournier, Calamante, Gadian, & Connelly, 2004) proposed the usage of Spherical Harmonics (SH) basis in place of the diffusion tensor to achieve better angular resolution. Independently from the choice of the basis function used to generate the dictionary, SD suffers of issues and limitations that are well known in any field dealing with deconvolution. Firstly, the problem is ill-posed, i.e. Eq. [38] may have multiple solutions to the problem. Additionally, the problem is generally ill-conditioned, meaning that the number of rows of U is generally much smaller than the number of the columns, thus the inversion problem in Eq. [39] is extremely prone to numerical errors and to noise. As a result, small changes in *S* lead to great changes in the reconstructed vector p. Some methods have been proposed to mitigate these issues, as the

Constrained Spherical Deconvolution (CSD) (J-Donald Tournier et al., 2008), or the modified Dumped "Richardson-Lucy" (mDRL) algorithm (Dell'acqua et al., 2010). Another viable way, that has not been well explored in the dMRI context is the regularized Non-Negative Least Squares (NNLS) approach. CSD coupled with SH basis is probably the most popular SD technique in the current literature about dMRI deconvolution. However, this chapter is developed around mDRL, while more details about the NNLS approach will be discussed in Chapter VI in a different application. Before introducing the signal model used in this work, it is useful to present the Multi-Shell Multi-Tissue (MSMT) technique. The CSD approach to Eq. [39] is to solve a constrained least-squares problem:

$$\begin{cases} \mathrm{x} = \underset{\hat{\mathrm{x}}}{\operatorname{argmin}} \dfrac{1}{2} \|\mathrm{C}\hat{\mathrm{x}} - \mathrm{d}\|_2^2 \\ \mathrm{Ax} \geq 0 \end{cases} \quad [40]$$

where A is a matrix relating the deconvolution coefficients to the signal amplitudes while imposing positivity, x is the deconvolution vector, C is the dictionary built with SH basis and d the data acquired with different diffusion gradient directions but a specific diffusion weighting. In most applications of CSD the vector C is estimated directly from the data (response function), i.e. picking voxels with single fiber population and deriving the SH decomposition of the average signal. Eq. [40] can be extended to support data acquired at multiple diffusion weighting:

$$\begin{cases} \hat{\mathrm{x}} = \underset{\mathrm{x}}{\operatorname{argmin}} \dfrac{1}{2} \left\| \begin{bmatrix} \mathrm{C}_1 \\ \vdots \\ \mathrm{C}_\mathrm{m} \end{bmatrix} \mathrm{x} - \begin{bmatrix} \mathrm{d}_1 \\ \vdots \\ \mathrm{d}_\mathrm{m} \end{bmatrix} \right\|_2^2 \\ \mathrm{Ax} \geq 0 \end{cases} \quad [41]$$

Where d_i is the vector of data acquired with different diffusion gradient directions and the i-th diffusion weighting, m is the number of diffusion weightings and C_i the corresponding SH basis dictionary. The extension of Eq. [41] to include *n* tissue types (*n* response functions) is the foundation of the MSMT framework:

$$\begin{cases} \begin{bmatrix} \hat{x}_1 \\ \vdots \\ \hat{x}_n \end{bmatrix} = \underset{\begin{bmatrix} x_1 \\ \vdots \\ x_n \end{bmatrix}}{\operatorname{argmin}} \dfrac{1}{2} \left\| \begin{bmatrix} \mathrm{C}_{1,1} & \cdots & \mathrm{C}_{1,\mathrm{n}} \\ \vdots & \ddots & \vdots \\ \mathrm{C}_{\mathrm{m},1} & \cdots & \mathrm{C}_{\mathrm{m,n}} \end{bmatrix} \begin{bmatrix} x_1 \\ \vdots \\ x_n \end{bmatrix} - \begin{bmatrix} \mathrm{d}_1 \\ \vdots \\ \mathrm{d}_\mathrm{m} \end{bmatrix} \right\|_2^2 \\ \begin{bmatrix} \mathrm{A}_1 & 0 & 0 \\ 0 & \ddots & 0 \\ 0 & 0 & \mathrm{A}_n \end{bmatrix} \begin{bmatrix} x_1 \\ \vdots \\ x_n \end{bmatrix} \geq 0 \end{cases} \quad [42]$$

For the analysis of brain dMRI data the authors proposed to use 3 tissue classes, i.e. WM, GM and CSF. GM and CSF were described with direction independent signals (isotropic diffusion, zero-order SH). The simplified formulation of the problem takes the following form:

$$S = S_0(f_{GM}\mathrm{C_{GM}} + f_{WM}\mathrm{C_{WM}} + f_{CSF}\mathrm{C_{CSF}}) \quad [43]$$

where f_x are the fractional amplitudes of each tissue type and C their response functions, that are estimated from chosen representative voxels. The choice of picking a response function for each subject arises concerns about the comparability of fractions estimated from different subjects or from the same subject over multiple time-points. Moreover, it implicitly assumes the diffusion properties of each tissue type to be constant throughout the brain, assumption that may hold for CSF but is probably less trivial for different gray matter areas. Finally, no measures of diffusion are quantified for any of the analyzed tissue classes. We proposed a different formulation to address these observations:

$$S = S_0\Big(f_{FREEWATER}e^{-b\cdot 0.003} + (1 - f_{FREEWATER})\Big(f_{ISO}e^{-bD_{ISO}} + (1 - f_{ISO})(K \cdot SD_{ANISOTROPIC})\Big)\Big) \quad [44]$$

With "*FREEWATER*" we denote a compartment characterized by isotropic diffusion and diffusion coefficient $3\text{x}10^{-3}\text{mm}^2/\text{s}$ (diffusion constant of water at 37 °C). "*ISO*" was attributed to an isotropic diffusion compartment with diffusion coefficient $0 \leq D_{ISO} < 3\text{x}10^{-3}\text{mm}^2/\text{s}$. Finally, $SD_{ANISOTROPIC}$ refers to an anisotropic compartment that is modeled with SD, choice that avoids the introduction of additional parameters while preserving the ability to follow complex fiber architectures. In its final formulation, that is schematized in **Figure 13**, the model resembles an extended "Ball and stick" model (Behrens et al., 2003), with an arbitrary number of sticks and with the addition of free water.

The columns of the deconvolution matrix U used to derive $SD_{ANISOTROPIC}$ were generated with the DTI model for the same diffusion directions and weighting used in the acquisition scheme and imposing the following eigenvalues for the diffusion tensor: $\lambda_1 = 1.6\text{x}10^{-3}\text{mm}^2/\text{s}$, $\lambda_2 = \lambda_3 = 0.3\text{x}10^{-3}\text{mm}^2/\text{s}$.

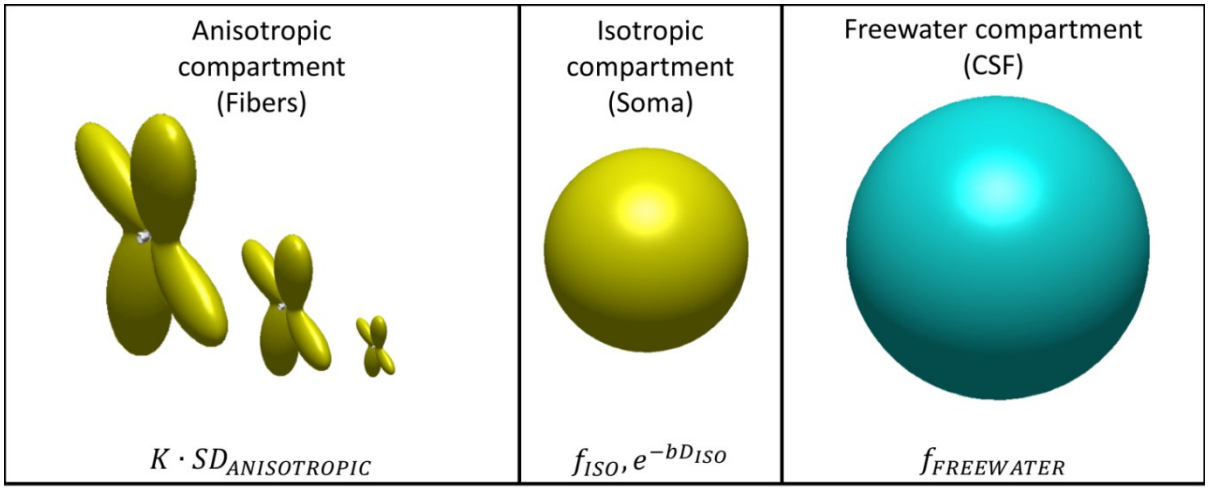

Figure 13 Schematic representation of the three compartments included in our proposed framework. Two of the three compartments are isotropic Gaussian decaying compartments, one with fixed diffusivity (free water), one estimated but bounded. The anisotropic compartment is derived with spherical deconvolution, therefore only its fraction is estimated.

The deconvolution operation was performed with the mDRL algorithm cycling 400 iterations. Recalling the notation used in Eq. [39], the procedure can be written as an iterative algorithm:

$$[\mathrm{p}^{(\mathrm{k}+1)}] = [\mathrm{p}^{(\mathrm{k})}]\left(1 + [\mathrm{u}^{(\mathrm{k})}]\left(\frac{\mathrm{U^T S} - \mathrm{U^T U p}^{(\mathrm{k})}}{\mathrm{U^T U p}^{(\mathrm{k})}}\right)\right) \quad [45]$$

where u is a vector damping each element of p, and k is the current iteration. The output of the mDRL algorithm was thresholded above its mean value, to decimate small lobes and penalize non-sharp deconvolution results, then normalized and multiplied by U to obtain $SD_{ANISOTROPIC}$. In Eq. [44] it is noticeable that $SD_{ANISOTROPIC}$ is multiplied by the parameter K, with the purpose of scaling the signal to better fit voxels characterized by different response functions (i.e. diffusivity values different from those imposed to generate U). The fit of Eq. [44] was performed with non-linear least squares using the Trust Region Reflective algorithm and imposing the following physiologically feasible constraints on the parameters:

- $f_{FREEWATER}$ and f_{ISO} between 0 and 1;
- D_{ISO} between 0 and 1.3×10^{-3} mm^2/s;
- K between 0.7 and 2.

Among the advantages of this approach we underline that it provides fractional coefficients that are bounded between 0 and 1, as well as voxel-wise estimation of a diffusion coefficient specific to gray matter.

Data & Methods

dMRI and T_{1W} data of 3 healthy subjects were downloaded from the Human Connectome Project (HCP, (McNab et al., 2013; Van Essen et al., 2013)) 3T database. The T_{1W} scan was performed with the following acquisition parameters: Magnetization Prepared Rapid Acquisition Gradient Echo (MPRAGE), T_E=2.14 ms, TI=1s, T_R=2.4s, resolution 1x1x1mm^3. dMRI data was acquired following a blip-up blip-down phase-encoding paradigm to perform accurate EPI correction and least-squares signal reconstruction (Andersson et al., 2003). The dMRI acquisition was performed with the following parameters: T_E=89.5ms, T_R=5.52s, resolution 1x1x1mm^3. dMRI data included 18 non-weighted images and 90 gradient directions evenly distributed on half sphere at b=1000,2000,3000s/mm^2, for a total of 288 volumes. Data of the HCP was employed for development and validation of this model as it is of public domain, thus improving studies repeatability, and it is characterized by high acquisition quality, guaranteed by customized hardware and dedicated gradient amplifiers capable of generating RF pulses up to G=300mT/m. An explorative application of this method was also performed on the data of a patient affected by MS (male, 42 years old). The subject underwent an MRI session with a Philips Achieva 3T scanner at the MS Centre of Verona University Hospital. The acquisition included a 3D T_{2W} TSE scan (T_E/T_R 268/2600ms, resolution 1.7x1.7x1.7mm^3), a 3D FLAIR volume (T_E/T_R 292/5500ms, Inversion Time (TI) 1650ms, resolution 1x1x1mm^3) and a dMRI acquisition (T_E=109ms, T_R=12.5s, flip angle 90 degrees, SENSE factor 2, resolution 2x2x2mm^3, SPIR fat suppression) with 32 directions at b=700s/mm^2, 64 directions at b=2000s/mm^2 and 7 non-weighted volumes. dMRI data from the HCP project was pre-processed with the "Topup" and "Eddy" tools of FSL (Andersson & Sotiropoulos, 2016). The first estimates a warp field from the data acquired with opposite phase-encodings to correct for geometric distortions caused by B_0 inhomogeneity and eddy currents, the second performs motion correction in concatenation with the pre-computed warp field, then performs data reconstruction using both acquisitions and a least squares approach. dMRI data of the MS subject was acquired only with PA phase-encoding and was pre-processed with Tortoise using the T_{2W} image as reference. T_{1W} data was processed with the N4 tools of ANTs (Tustison et al., 2010) to reduce intensity field biases, then the standardized FSL anatomical pipeline "fsl_anat" was

performed. This pipeline serially applies common FSL tools as the "Brain Extraction Tool" (BET, (S. M. Smith, 2002)), that performs brain extraction (also called skull removal), and FAST ((Y Zhang, Brady, & Smith, 2001)) to perform the actual tissue segmentation into gray matter, white matter and cerebrospinal fluid. FAST, that is one of the most common tool for brain tissue segmentation, outputs the Partial Volume Estimation (PVE) maps for each tissue class. dMRI data was fitted with Eq. [44] to derive voxel-wise maps of f_{ISO}, $f_{FREEWATER}$ and D_{ISO}. Assessment of the goodness of fit was performed to ensure the voxel-wise residuals had zero mean (one sample t-test), and were normally distributed after variance normalization (chi-square test). Additionally, voxel-wise R^2 values and estimates precision were evaluated, with the latter expressed as percentage coefficient of variation, $CV_{\%}$. R^2 is not a good metric to compare non-linear regressions (Spiess & Neumeyer, 2010), however, it still is an informative metric about the explained variance. Statistics of $CV_{\%}$ were evaluated where each parameter was meaningful, i.e. statistics for f_{ISO} and D_{ISO} were computed in GM, statistics of $f_{FREEWATER}$ in CSF (masked using the PVE map). T_{1W} data of each subject was rigidly aligned to the first non-weighted dMRI volume with ANTS using the Normalized Mutual Information metric (Avants et al., 2011). The rigid transformation was sufficient to obtain proper alignment of the data thanks to the full correction of EPI geometric distortions. Spatial correspondence between the segmentation obtained with T_{1W} derived GM – WM – CSF PVE and the corresponding maps f_{ISO}, $1\text{-}f_{ISO}$, $f_{FREEWATER}$ was evaluated with a custom metric. In particular, the fractional maps provided by the algorithm (A) were compared with the PVE segmentation (B) obtained with FSL FAST on the T_{1W} scan using the following agreement metric:

$$AG = 1 - |A - B|/(A \cup B). \quad [46]$$

The agreement between the fractional maps and the PVE segmentation was further exploited with a linear regression: for each tissue class both segmentations were thresholded at different values, from 0 to 1 with step 0.05, then the number of voxels above the thresholds was counted. On the resulting vectors of each tissue class X, respectively $CO_{X,PVE}$ for PVE and $CO_{X,f}$ for the corresponding map estimated from our model, we performed the linear regression

$$CO_{X,PVE} = CO_{X,f} \cdot m + const \quad [47]$$

and computed its adjusted R^2 value.

Results

Data downloaded from the HCP database was fit with Eq. [44] as mentioned above, then goodness of fit was assessed with statistical analysis of the voxel-wise residuals. The residuals were overall zero-averaged, and only a small percentage of voxels, between 0.09% (HCP subject 1) and 0.23% (HCP subject 3), deviated from the null hypothesis. None of the chi-square tests performed on the weighted residuals rejected the null-hypothesis of the data coming from a standard normal distribution. Average voxel-wise R^2 values were between 0.98±0.03 (HCP subject 3) and 0.99±0.02 (HCP subject 1), and although R^2 is not a good metric for non-linear least squares regressions, it suggests an overall appropriate fit of the data. Visual inspection of the residuals weighted by the a-posteriori variance further confirmed the randomness of the fit. **Figure 14** shows the mean ± standard deviation of the average weighted residuals computed in GM and WM (segmented with the T_{1W} derived PVE maps) of HCP S1.

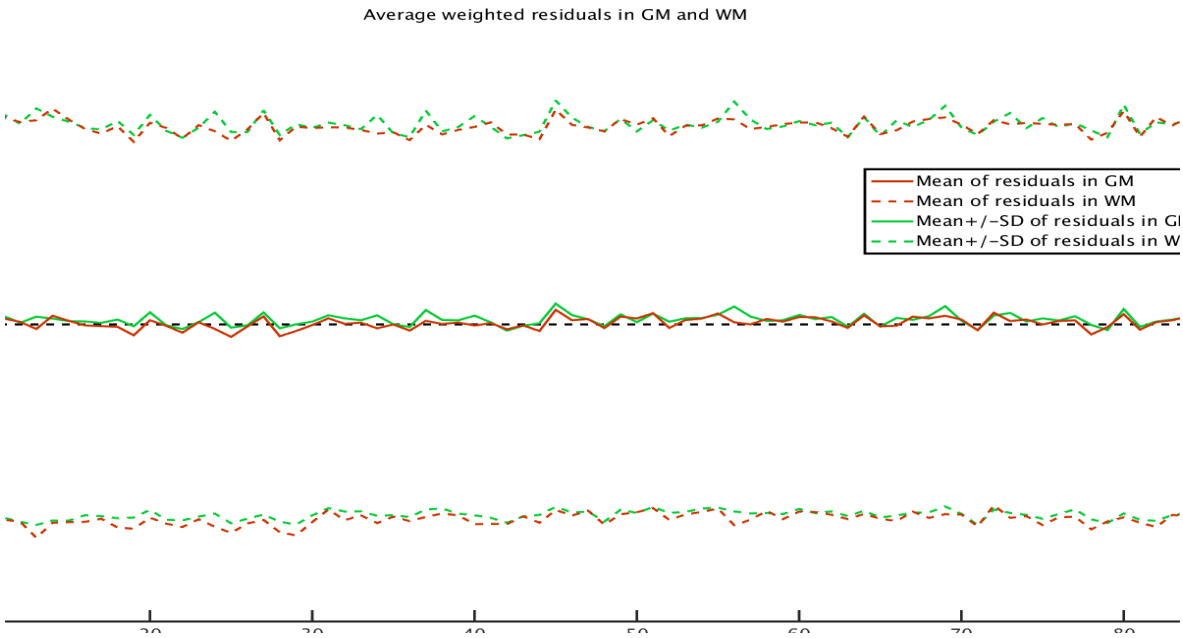

Figure 14 Mean (solid lines) and mean ± standard deviation (dotted lines) of the average weighted residuals computed in the GM (red) and WM (green) of HCP S1. WM and GM were segmented using the PVE maps computed on T_{1W} data. Residuals were randomly distributed with zero mean in both cases.

A middle axial slice for each of the estimated parametric maps of the three HCP subjects is reported in **Figure 15**. It is appreciable that f_{ISO} assumed high values in the cortical area, while 1- f_{ISO} was conversely high in white matter. Finally, $f_{FREEWATER}$ assumed high values in regions known to be dominated by CSF, but it was non-zero also in tissue voxels. The

estimated D_{ISO} values, that appeared to be very specific of the cortical area, were around $0.7x10^{-3}mm^2/s$. Color maps representative of the DW tissue segmentation were created by assigning $f_{FREEWATER}$ to the blue channel, f_{ISO} to the green channel and 1- f_{ISO} to the red channel. Same procedure was followed for the T_{1W} PVE segmentation computed by FSL FAST. The RGB maps, both shown in **Figure 15** for each subject, had high spatial agreement, although the cortical layer appears to be thinner in the DW segmentation. Eventually, this may be due to the dominant influence of CSF on the dMRI signal, given its long T_2. Moreover, the compartments modeling CSF and GM were both characterized by isotropic Gaussian decay, thus their identifiability might be low in situations of small partial volume effects.

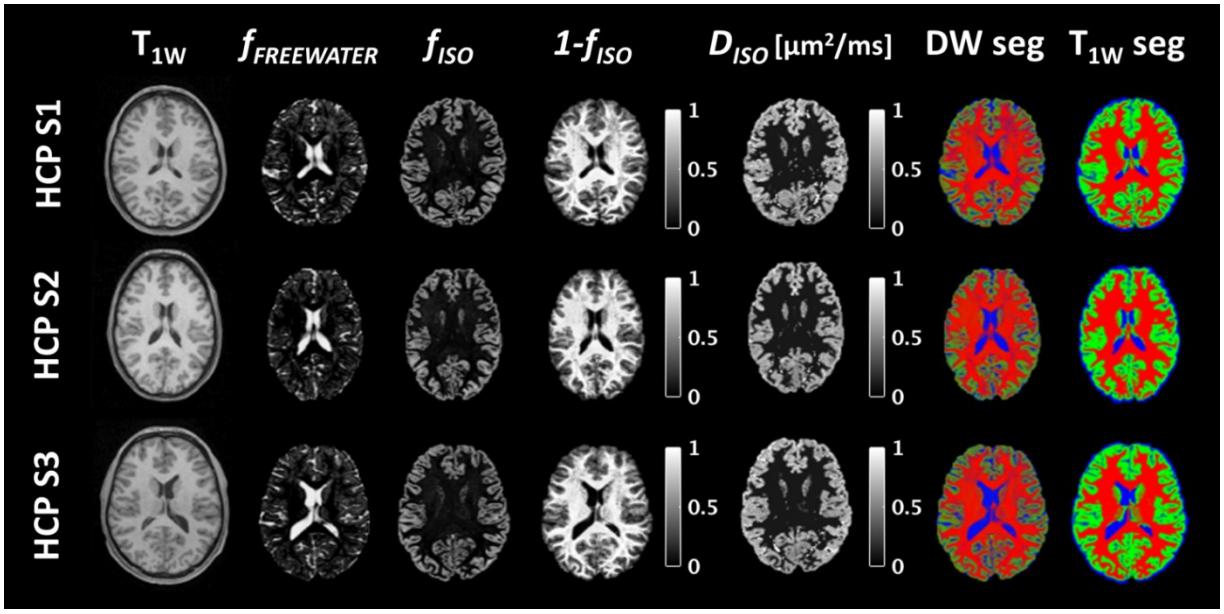

Figure 15 A middle axial slice of the T_{1W} images of the three HCP subjects (first column), and the corresponding parametric maps derived with our model (columns 2 to 5). The high spatial correspondence between the parametric maps and the biological tissue they should describe is appreciable. Last two columns show the segmentation RGB maps from DW and T_{1W} respectively, obtained assigning gray matter to green, white matter to red and cerebrospinal fluid to blue.

Quantitative agreement between each f_x map and the corresponding T_{1W} derived PVE map were computed for each subject thresholding the maps at different values between 0 and 1, then the agreements were averaged to obtain **Figure 16**.

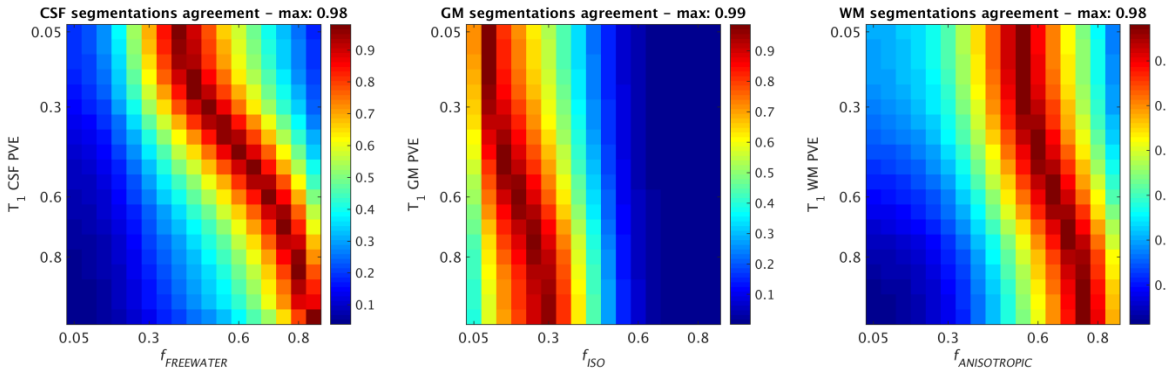

Figure 16 Spatial agreements between the fractional maps estimated from our model and the PVE maps provided by FSL FAST. Agreements were obtained with variable thresholds for both maps. From left to right CSF, GM and WM. All three classes show good linear agreement and high correspondence.

The agreements appeared to be consistent across subjects and high for a wide range of thresholds. **Table 6** reports the adjusted R^2 values of the linear regression between the two corresponding segmentation maps, that were very high and proved a good linear correlation, especially between the PVE of WM and $f_{ANISOTROPIC}$.

Table 6 Adjusted R^2 of the linear regression for each tissue class between the cumulative agreement masks between maps provided by our model and the segmentation provided by FSL FAST.

Adjusted R^2 of the $CO_{X,PVE}$ vs $CO_{X,f}$ regression			
Subject	WM	GM	CSF
HCP S1	0,97	0,80	0,83
HCP S2	0,97	0,77	0,82
HCP S3	0,97	0,76	0,82

The median values of $CV_{\%}$ on HCP S1-S2-S3 data were 20-16-17% for $f_{FREEWATER}$, 24-27-28% for f_{ISO}, and 16-17-17% for D_{ISO}.

We applied our method to a patient affected by MS as proof of concept, obtaining the maps shown in **Figure 17**. Some lesions could be observed on the T_{1W} image, however, the FLAIR acquisition offers a better contrast, highlighting four periventricular lesions and a number of smaller alterations in WM and close to the cortex. Interestingly, $f_{FREEWATER}$ showed higher values in some but not all the lesions, that were conversely highlighted by very high diffusion values in the D_{ISO} map. In agreement with results on the HCP data, f_{ISO} maps had high values

mainly in the brain cortex, but in addition showed high values in the lesions observed on the FLAIR image, as well as in other non-previously observed spots.

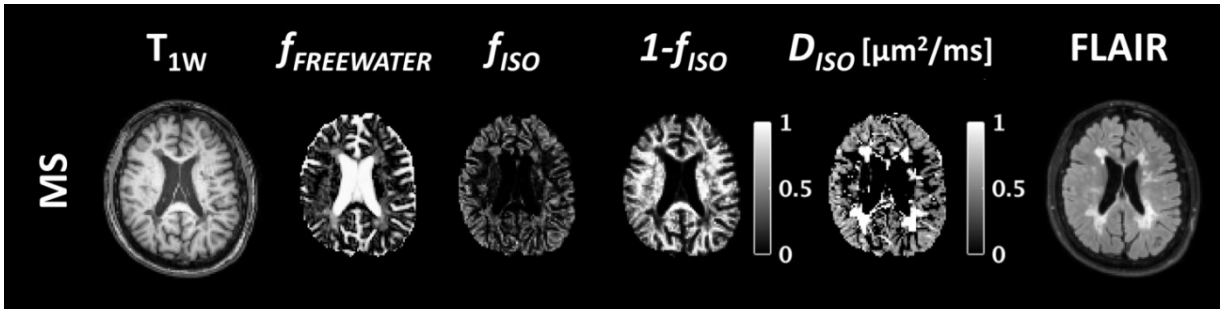

Figure 17 Middle axial slice of T_{1W}, diffusion derived maps and FLAIR of an MS patient. Lesions observable on the FLAIR image are visible as very high D_{ISO} values, increased f_{ISO} and increased $f_{FREEWATER}$.

Conclusions

With this work we introduced a novel quantification scheme for dMRI data that combines spherical deconvolution with multi-compartment modeling to perform tissue type segmentation and provide a diffusivity metric specific to GM (D_{ISO}). This approach can be used to compute tissue segmentation when no structural data is available. Nonetheless, the segmentation here provided is based on the diffusion properties of the tissues, therefore it is not expected to perfectly match that obtainable from T_{1W} data, that is known to have a slower response to underlying microstructural changes. Indeed, the comparison between the two segmentations may highlight early tissue alterations with stronger contrast. The initial experience with data of an MS subject, sampled with a clinically compatible protocol, supported the sensitivity of this technique. Further work will be needed to derive quantitative diffusivity indices related to the anisotropic compartment. It is important to point out some limitations of this work, that leave open space to further improvements. The deconvolution operation based on mDRL algorithm produces less sharp peaks than the CSD approach based on spherical harmonics, and requires the initialization of the deconvolution dictionary with arbitrary parameters. Interestingly, this also comes with the benefit of a more standardized analysis, differently from classic CSD techniques where a response function is picked for each subject and eventually for each tissue (MSMT). However, the minimum perpendicular diffusivity assumed for the anisotropic compartment is $0.3 \times 10^{-3} mm^2/s$, but to emulate a perfect ball and stick model a minimum value of zero should be allowed. Another limitation tackles the simplified formulation of the model, that does not take into account links between

different compartments as suggested by other models, as for example the tortuosity in NODDI. Eventually, the inclusion of similar links between the isotropic and anisotropic compartments might further enhance the performances of this approach. Finally, the fit of Eq. [44] is performed through non-linear Least-Squares with the Trust-Region Reflective Algorithm, that although robust may provide local non-optimal solutions, and is much slower than the algorithm employed in the MSMT approach, that solves a constrained linear system. Approaches as parallel computing could help reducing the computation time, while local minima could be avoided by smart initialization strategies as grid search.

CHAPTER V: INTRA-VOXEL INCOHERENT MOTION AND NON-GAUSSIAN DIFFUSION OF THE SKELETAL MUSCLE

Introduction

Most of the developments and applications of dMRI have involved the brain, however, the technique was originally applied to the body, and the skeletal muscle was one of the first imaged tissues (Tanner, 1979). The Gaussian diffusion model has been applied to the skeletal muscle both in its isotropic (ADC) and anisotropic (DTI) formulations to investigate its healthy architecture (Froeling et al., 2012; Galbán, Maderwald, Uffmann, de Greiff, & Ladd, 2004; Zijta et al., 2011), changes in disease (Bonati, Hafner, et al., 2015; Hooijmans et al., 2015; Ponrartana et al., 2014) and the effects of training (Filli, Boss, et al., 2015; Froeling et al., 2015). In Chapter III it was observed that the Gaussian diffusion model can be applied only in a specific range of diffusion weightings, and that signals acquired above b=1500s/mm^2 in the brain are affected by non-Gaussian diffusion. This is the case also for the skeletal muscle. However, the acquisition of muscle data at strong diffusion weighting is technically challenging, reason why this phenomenon has not been extensively investigated. Jensen et al. (Jensen et al., 2005) proposed the "Diffusion Kurtosis Imaging" (DKI) model as an extension of DTI to quantify non-Gaussian diffusion through the concept of kurtosis. Being an extension of DTI, DKI is a model of the diffusion process and does not make any assumption on the analyzed tissues, and actually is one of the few choices to quantify the non-Gaussian behavior of the dMRI signal in the skeletal muscle (Marschar et al., 2015). Previous studies on the brain (Guglielmetti et al., 2016; Pang et al., 2015) and on animals (Cheung et al., 2009) showed that kurtosis might achieve higher sensitivity to microstructural changes than DTI, therefore its clinical applicability to the skeletal muscle may be of great interest. dMRI acquisition protocols employed for the brain can be adapted to acquire data of the skeletal muscle, however, the much shorter T_2 of the muscles leads to significantly reduced SNR at identical echo time. Additionally, fat is more abundant than in the brain and has a more complex composition, worsening the efficiency of fat suppression. A recent review by Oudeman et al. (Oudeman et al., 2015) summarizes these issues and also points out the effects of other covariates on the acquired signals. An additional source of variability in the dMRI signal is blood perfusion. Since the early days of dMRI, it was observed that the ADC model was not able to describe in-vivo data at low diffusion weighting (D Le Bihan et

al., 1986), where the water flowing in the micro-vascular network significantly contributed to the measured diffusion weighted signal. Such effect, named pseudo-diffusion, was described in the "Intra-Voxel Incoherent Motion" (IVIM) framework. Some recent works have recognized blood perfusion as a confounding factor for ADC estimations (Iima & Le Bihan, 2016; Denis Le Bihan, 2013; Luciani et al., 2008), however few is known about its effect on DTI or DKI estimations. In this chapter we aim to address the applicability and the underpinnings of DTI, IVIM and DKI in the context of the skeletal muscle, showing the results of a study we recently published (Alberto De Luca, Bertoldo, & Froeling, 2016). Using both simulations and real data, we investigated the effects of perfusion on DTI and DKI estimates and the repeatability of the estimates. Finally, the cross-correlations between the computer parameters, including DTI and DKI parameters, were evaluated.

Theory

In dMRI the Gaussian diffusion is generally assumed, but at least three different diffusion regimes have been previously reported in literature: DTI, bi-exponential pseudo-diffusion regime at low b-values (IVIM) and non-Gaussian diffusion (DKI) at high b-values. The IVIM model was introduced by Le Bihan and colleagues (D Le Bihan et al., 1986), and essentially expresses the acquired signal S as the sum of two non-exchanging compartments:

$$S = S_0\left((1-f)e^{-b\cdot \mathrm{ADC}} + fe^{-bD^*}\right) \quad [48]$$

where S_0 is the non-weighted signal. **Figure 18** shows a pictorial representation of the dMRI signal as sum of the tissue and perfusion signals. The parameter f in Eq. [48] quantifies the signal offset and thus the bias of the data at high b-values (the difference between the black solid line and circles in **Figure 18**). Differently, D^* determines the perfusion signal decay at low b-values (solid red lines in **Figure 18**) but does not influence the signal bias for high b-values. It should be noted that Eq. [48] implicitly assumes no water exchange takes place between the vascular and extra-vascular pool within the diffusion experiment time (Hazlewood, Chang, Nichols, & Woessner, 1974). When these assumptions are not met, models accounting for water exchanges should be considered, as the "Random Permeable Barrier Model" (Eric E. Sigmund et al., 2014). As observed in Chapter II and Chapter IV, the magnitude of ADC is generally between 0 and $3\text{x}10^{-3}\text{mm}^2/\text{s}$, while D^* can be 100 times higher.

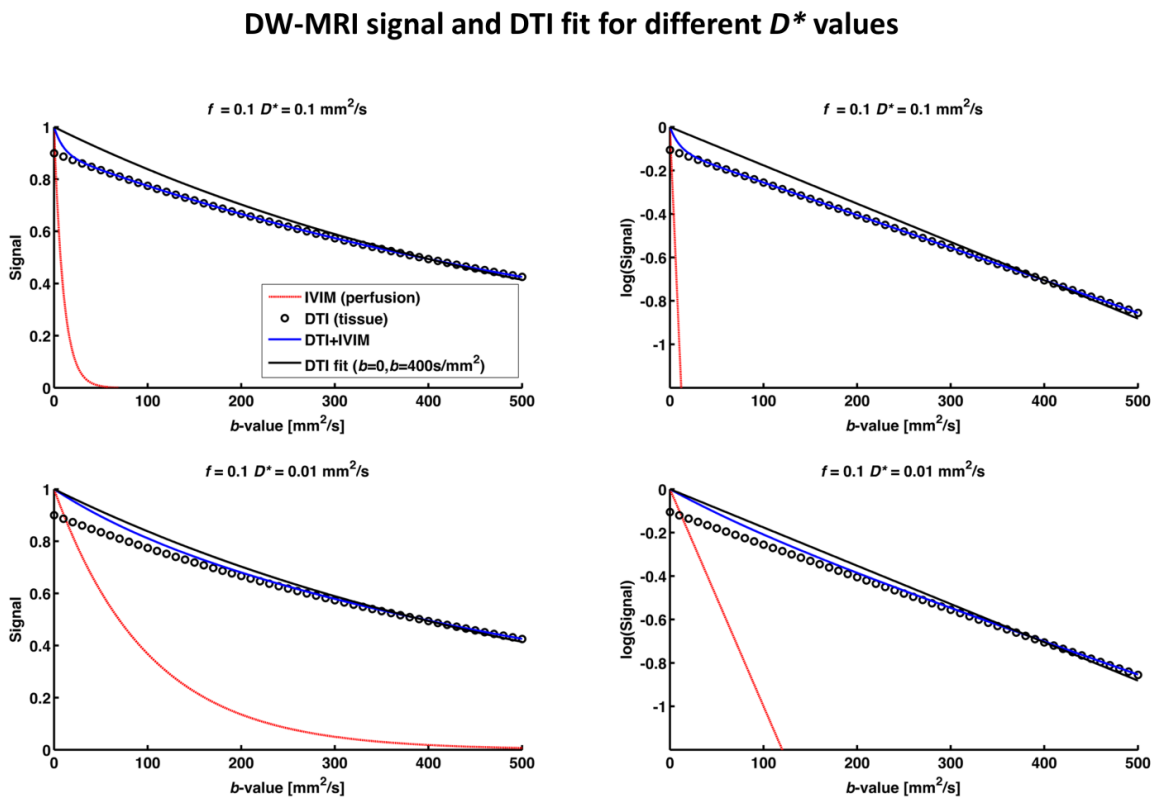

Figure 18: An example of normalized dMRI signal (left column) and its logarithm (right column), generated with MD=1.5μm^2/ms, perfusion signal fraction 10% and two D^* values (first row D^*=100mm^2/s, second row D^*=10mm^2/s). Black circles are the tissue signal fraction that does not decay from 1 due to the perfusion signal fraction. The black solid line represents the DTI fit obtained acquiring only b=0 and b=400s/mm^2, which over-estimated MD (1.8μm^2/ms). The bias in DTI fit is determined purely by the perfusion fraction regardless of D^*.

Several strategies have been proposed to fit the IVIM model (Cho et al., 2015; Filli, Boss, et al., 2015) and to overcome fitting instability and issues due to the high variability of the signal generated from the micro-vascular network at low diffusion weighting, and to the multi-exponential formulation of the model. The DTI model can be extended to also take in account the signal loss due to perfusion, although extra data at low b-values is needed. Incorporating the IVIM equation [48] in the full tensor model (Chapter I, Eq. [18]), the bi-exponential signal equation becomes:

$$S_{\text{IVIM,DTI}} = S_0(fe^{-bD^*} + (1-f)e^{-b\mathbf{g}^{\mathbf{T}}\bar{D}\mathbf{g}}) \quad [49]$$

Perfusion free MD values (MD_{LIN}) can alternatively be obtained using data acquired at multiple high b-values, where the contribution of fast de-phasing spins from the vascular and micro-vascular compartments is negligible and low enough such that the assumption of Gaussian diffusion is approximately valid. With this simpler approach, the effect of perfusion on MD can be minimized while still estimating f, however, values of D^* cannot be computed.

Given S_0 acquired at b=0s/mm^2, MD_{LIN} and the intercept S_0^* can be computed with linear fit of the high b-values data, then f can be estimated as follows:

$$f = \frac{S_0 - S_0^*}{S_0} \quad [50]$$

Jensen et al. (Jensen & Helpern, 2010; Jensen et al., 2005) proposed the DKI framework as a convenient extension of the DTI model to account for non-Gaussian signals. DKI essentially descends from the Taylor expansion of log(S) (Chapter I, Eq. [20]) in successive powers of the term b:

$$\log(S) = \log(S_0) - bD + \frac{1}{6}b^2D^2(K-3) + O(b^3) \quad [51]$$

where K is named apparent kurtosis coefficient, and under the short pulse condition ($\delta \to 0$) quantifies the excess of kurtosis. Given the probability distribution function $P(\mathbf{s},t)$ of a water molecule to undergo a displacement $\mathbf{s}$ in a time t, it is possible to define the average function operator:

$$\langle F(\mathbf{s}) \rangle = \int d^3\mathrm{s}\, P(\mathbf{s},t) F(\mathbf{s}) \quad [52]$$

Considered the gradient direction $\mathbf{g}$, the excess of kurtosis in the time domain is defined as:

$$K(t) = \frac{\langle (\mathbf{g}\cdot\mathbf{s})^4 \rangle}{\langle (\mathbf{g}\cdot\mathbf{s})^2 \rangle^2} - 3 \quad [53]$$

Eq. [51] can be written for each acquired gradient direction, therefore the result can be generalized to define the kurtosis tensor $\overline{K}$ and spatially describe the non-Gaussian diffusion process:

$$\begin{aligned} \log(S) &= \log(S_0) - b\sum_{i=1}^{3}\sum_{j=1}^{3} \mathbf{g}_i\mathbf{g}_j\overline{D}_{ij} \\ &+ \frac{1}{6}b^2\left(\frac{1}{3}\sum_{i=1}^{3}\overline{D}_{ii}\right)\sum_{i=1}^{3}\sum_{j=1}^{3}\sum_{k=1}^{3}\sum_{l=1}^{3} \mathbf{g}_i\mathbf{g}_j\mathbf{g}_k\mathbf{g}_l(\overline{K}_{ijkl} - 3) + O(b^3) \end{aligned} \quad [54]$$

$\overline{K}$ is a fourth order tensor with dimension 9x9 and thus 81 elements, but, thanks to symmetry constraints, only 15 elements have to be determined. Nonetheless, the simultaneous estimation of $\overline{D}$ and $\overline{K}$ results in a problem with 21 unknowns. The definition of low and high b-values in which each regime is valid is tissue dependent. The low b-value threshold

essentially depends on the micro-vascular architecture, while the high *b*-value threshold is determined by the membranes and the internal structure of the cells. For the skeletal muscle, we considered low *b*-values $b \leq 200 s/mm^2$ (Cho et al., 2015), where the contribution of fast de-phasing spins from the vascular and micro-vascular compartments is non-negligible. The assumption of Gaussian diffusion is approximately valid for *b*-values between 200 (Cho et al., 2015; E. E. Sigmund et al., 2012) and $700 s/mm^2$, given that the effect of kurtosis on the signal at $b=700 s/mm^2$ is around 5% for values typical of the skeletal muscle (i.e. $MD=1.4 \times 10^{-3} mm^2/s$, $K=0.3$). In this work we employed a simplified formulation of the DKI model with a single *K* parameter (isotropic kurtosis) in place of the $\overline{K}$ tensor:

$$S_K = S_0 e^{-b\mathbf{g}^{\mathbf{T}}\bar{D}\mathbf{g}+\frac{1}{6}b^2D^2(K-3)} \quad [55]$$

where *D* is the mean diffusivity computed from $\overline{D}$, and *K* is the dimensionless isotropic kurtosis. Eq. [55] can be extended with the IVIM model similarly to Eq. [49], to compute kurtosis while correcting for perfusion with IVIM:

$$S_{\text{IVIM,DKI}} = S_0(fe^{-bD^*} + (1-f)e^{-b\mathbf{g}^{\mathbf{T}}\bar{D}\mathbf{g}+\frac{1}{6}b^2D^2(K-3)}) \quad [56]$$

A previous work from Lu et al. (Lu et al., 2012) proposed the extension of the isotropic IVIM model with isotropic kurtosis, however their model had 4 degrees of freedom (Eq. [56] has 10 free parameters as it accounts for the full diffusion tensor) and could not be used to infer the effect of perfusion on DTI/DKI parameters.

Data & Methods

Two similar experiments including simulated and real data were designed to elucidate the effects of IVIM on DTI and DKI. *Experiment I* evaluated the effects of perfusion on DTI metrics and the efficacy of IVIM correction, while *Experiment II* investigated the same effects on DKI metrics. In addition, the correlation between DTI and DKI parameters and the correlation between longitudinal variations of the same parameters were evaluated. Simulations for *Experiment I* were performed using Eq. [49] and two *f* values, $f=5\%$, that is the average value we observed in-vivo, and $f=15\%$, that is the highest value we observed in-vivo in muscle, consistently with previous studies (Filli, Boss, et al., 2015; Filli, Wurnig, et al., 2015; Hiepe et al., 2014; Nguyen et al., 2016; Qi, Olsen, Price, Winston, & Park, 2008). Simulations for *Experiment II* were generated with Eq. [56] and four combinations of biologically feasible *f* and *K* values: ($f=5\%$, $K=3$), ($f=15\%$, $K=3$), ($f=5\%$, $K=3.5$), ($f=15\%$,

K=3.5). Both simulations were performed aligning the diffusion tensor with the coordinates axis, using the x-axis for the major eigenvector and imposing MD=1.3x10^{-3}mm^2/s, FA=0.34, that are values commonly observed in muscles. The simulated diffusion gradients scheme featured 12 non-weighted images (b=0s/mm^2), 6 gradient directions at b=2,5,10,20,50,100,200s/mm^2, 10 gradient directions at b=400s/mm^2, 15 gradient directions at b=700s/mm^2, 25 gradient directions at b=1000s/mm^2 and 30 gradient directions at b=1300s/mm^2. A graphical representation of the acquisition protocol and of the models associated to each gradient weighting is reported in **Figure 19**.

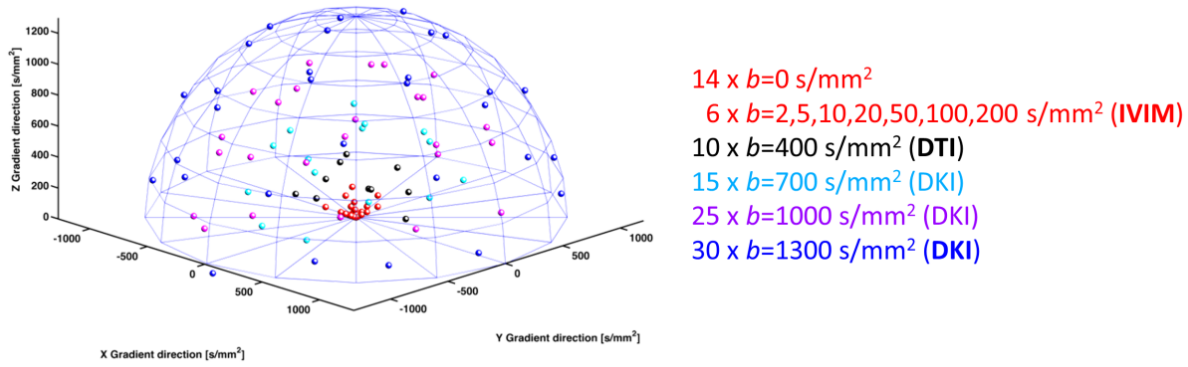

Figure 19 Visual representation of the acquired dMRI protocol on the half sphere. Directions were optimized by electro-static repulsion in each shell. The protocol included 14 non-weighted volumes, 42 volumes for IVIM, 10 volumes for DTI and 60 volumes for DKI.

Each simulation was repeated 5000 times with addition of Rician noise to achieve SNR levels 10, 30 and 500 (respect to the b=0s/mm^2 volumes). Statistical analysis of the simulations was performed computing the 25, 50 and 75 percentile of MD, FA, *K* (*Experiment II*) and *f* (IVIM extended models only). The relative bias of the estimates median value from the imposed settings was determined for each simulation and SNR level. MRI data of five healthy volunteers (3 males, 2 females, ages 28±5 years) was acquired twice, in 7 days interleaved MRI sessions, with a 3T Philips Achieva scanner (Philips Medical System, Best, The Netherlands). Dixon and dMRI of the right calf were acquired with a receive/transmit 16 channels kneel coil and the following specifications:

- 3D Fast Field Echo (FFE) Dixon with isotropic 1x1x1mm^3 resolution, field of view 240x240x150mm^3, 3 echoes, first echo time T_{E1}=3.57ms, echo spacing δT_E=1.08ms, repetition time T_R=5.53ms, flip angle 15°, sensitivity encoding SENSE factor 2;

- 2D EPI Spin-Echo dMRI with Stejskal-Tanner gradients, T_E=55ms, T_R=6.5s, SENSE=2.5, 1 signal average, voxel size 2.5x2.5x5mm^3, same field of view of Dixon, maximum gradient strength 62mT/m, EPI echo train length 39, same gradients scheme used in simulations, triple fat suppression with SPectrally selective Adiabatic Inversion Recovery (SPAIR), Slice-Selective Gradient Reversal (SSGR) (Nagy & Weiskopf, 2008; Park, Kim, & Cho, 1987) and olefeinic chain suppression (Williams et al., 2013);
- A noise measurement was performed at the end of each dMRI acquisition and was used for SNR quantification.

Volume agreement masks were computed for the corresponding time-points of each subject to consider the same anatomy through all statistical analysis. Muscle masks were generated with FSL BET on the first non-weighted volume of the first time-points, projected on the corresponding volume of the second acquisition, and finally back-projected to obtain common masks. These steps were performed with the non-rigid b-spline registration implemented in Elastix (Klein, Staring, Murphy, Viergever, & Pluim, 2010). Regions of interest (ROIs) were delineated on the Dixon water signal images, that feature high resolution and combine good contrast of muscle tissue with fat suppression. Muscles Tibialis Anterior, Tibialis Posterior, Fibularis Longus, Soleus (SOL), Gastrocnemius Medialis (GM) and Gastrocnemius Lateralis (GL) were manually drawn for each time-point. Dixon water signal images were registered to the first non-weighted image of the corresponding dMRI data using a non-rigid b-spline transformation to account for EPI distortions. dMRI data was pre-processed with a second order equation to correct for the b=0s/mm^2 signal drift (Vos et al., 2016), then combined eddy currents and motion artifacts correction was performed with affine registration of each diffusion weighted volume on the first with Elastix. Rotation of the b-matrix was performed accordingly (Leemans & Jones, 2009). Visual inspection of the data was performed after the pre-processing step to evaluate chemical shift artifacts and signal dropouts due to muscle contraction (Steidle & Schick, 2015). Six different model fits, 3 for each experiment, were implemented in MATLAB R2014b.

In particular, for *Experiment I*:

- Data acquired with b=0,400s/mm^2, that is a commonly used single-shell DTI protocol, was fitted with Eq. [18] using Linear Least-Squares (LLS) (results referred as [DTI-

LIN]) and with Eq. [18] using a custom Non-Linear Least-Squares (NLLS) estimator ([DTI-NONLIN]);

- Data corresponding to $0 \leq b \leq 400 s/mm^2$ was fitted with Eq. [49] using a custom NLLS algorithm ([DTI-IVIM]).

For *Experiment II* a similar procedure was followed:

- Data corresponding to $b=0,400,700,1000,1300 s/mm^2$ was fitted with Eq. [55] using LLS ([DKI-LIN]) and with Eq. [55] using NLLS ([DKI-NONLIN]);
- The complete data was fitted with Eq. [56] using NLLS ([DKI-IVIM]).

All NNLS algorithms used in this work were based on the constrained "Trust-Region Reflective" algorithm implemented in MATLAB R2014b (routine *lsqnonlin*). A multi-scale fitting approach was implemented to reduce the sensitivity to noise and optimize the guess of initial values. The voxel-wise fit was performed by averaging the neighbor signals within a 2D square, with progressive decrement of the square's size up to a single voxel fit. The multi-scale fit of each voxel V can be schematized with the following steps:

1. LLS fit of V's signal with the DTI model to initialize the diffusion tensor;
2. Average the signals in a 5x5 neighborhood of V and perform the NNLS fit of the chosen model;
3. Repeat step 2 with 3x3 and 1x1 neighborhoods using the previous fit results as starting points.

The following constraints were used for the optimization procedure:

- diagonal elements of the diffusion tensor between 0 and $3x10^{-3}$ mm^2/s;
- transverse elements of the diffusion tensor between $-3x10^{-3}$ and $3x10^{-3}$ mm^2/s;
- f between 0 and 1;
- D^* between $1x10^{-2}$ and 1 mm^2/s;
- K between 2 and 10;
- S_0 greater than 0.

The fitting of [DTI-IVIM] and [DKI-IVIM] was performed simultaneously including all parameters, providing good results while avoiding the need of subdividing data with arbitrary thresholds. Goodness of the voxel-wise fit was assessed with the Shapiro-Wilk test and one-sample t-test to ensure they were normally distributed and with zero mean. The average SD

of the residuals was computed as percentage of the average b=0s/mm^2 for each time-point and model, then minimum and maximum values were compared to the average measured SD. Additionally, the coefficients of variation (CV) of each parameter and the cross-correlations were computed to quantify the precision of the estimates and eventual model induced correlations between the parameters. For linear models [DTI-LIN] and [DKI-LIN] the covariance matrix associated to each voxel was computed as:

$$\mathrm{COV} = (X^T X)^{-1}\sigma^2 \quad [57]$$

where X is the design matrix of the linearized DTI/DKI models and σ^2 is the variance of the fit residuals. For non-linear models, the covariance matrix associated to each voxel can be computed from the Jacobian (J, matrix of the partial derivatives) provided by the non-linear optimizer:

$$\mathrm{COV} = (J^T J)^{-1}\sigma^2 \quad [58]$$

The covariance matrices of all subjects were averaged, then the Pearson correlation between each parameter was computed as:

$$CORR(X,Y) = \frac{COV(X,Y)}{\sqrt{COV(X,X)}\sqrt{COV(Y,Y)}} \quad [59]$$

where X and Y are two different parameters of the models.

Statistical analysis of MRI data of *Experiment I* was performed computing the 25, 50 and 75 percentile of FA, MD, f and D^* for each of the six muscle ROIs, as previously did for simulations. MD_{LIN} values were computed using the data at b=200s/mm^2 and b=700s/mm^2 and considered to be free of perfusion and kurtosis effects. The Pearson correlations between the median values of MD_{LIN} in each of the six ROIs and the corresponding median values of MD estimated with the three DTI models were evaluated. Pearson correlations between median f values estimated with [DTI-IVIM] and the corresponding median values of FA, MD, AD and RD were computed for each ROI. Reproducibility of the computed IVIM and DTI parameters across two time-points was investigated with Bland-Altman plots (Bland & Altman, 1986), including the evaluation of repeatability coefficients and repeatability index (RI) (Froeling et al., 2010). Statistical analysis of *Experiment II* was similarly performed, including 25, 50 and 75 percentile plots of FA, MD, AD, RD and K; Pearson correlations between MD and MD_{LIN}; correlations of the DTI and DKI parameters with f estimated with

[DKI-IVIM] and repeatability analysis. Finally, *Experiment II* included a Pearson correlation analysis of kurtosis and diffusivity metrics (MD, AD and RD), as well as the correlations analysis of their inter-scan variations (δK, δMD, δAD and δRD).

Results

Figure 20 reports the outcome of simulations for *Experiment I* (**Figure 20A**) and *Experiment II* (**Figure 20B**). *Experiment I* shows that both [DTI-LIN] and [DTI-NONLIN] did not recover the imposed MD values in the f=5% simulation, with an estimation bias of almost 10% at SNR=30. FA estimated with the two models was less affected by the perfusion bias than MD, with errors at SNR=30 of -1.2% and -5% respectively. The biases became more prominent at higher perfusion level (f=15%), as estimation errors of MD reached +30%, while errors on FA were between -14.7% ([DTI-NONLIN]) and -19% ([DTI-LIN]).

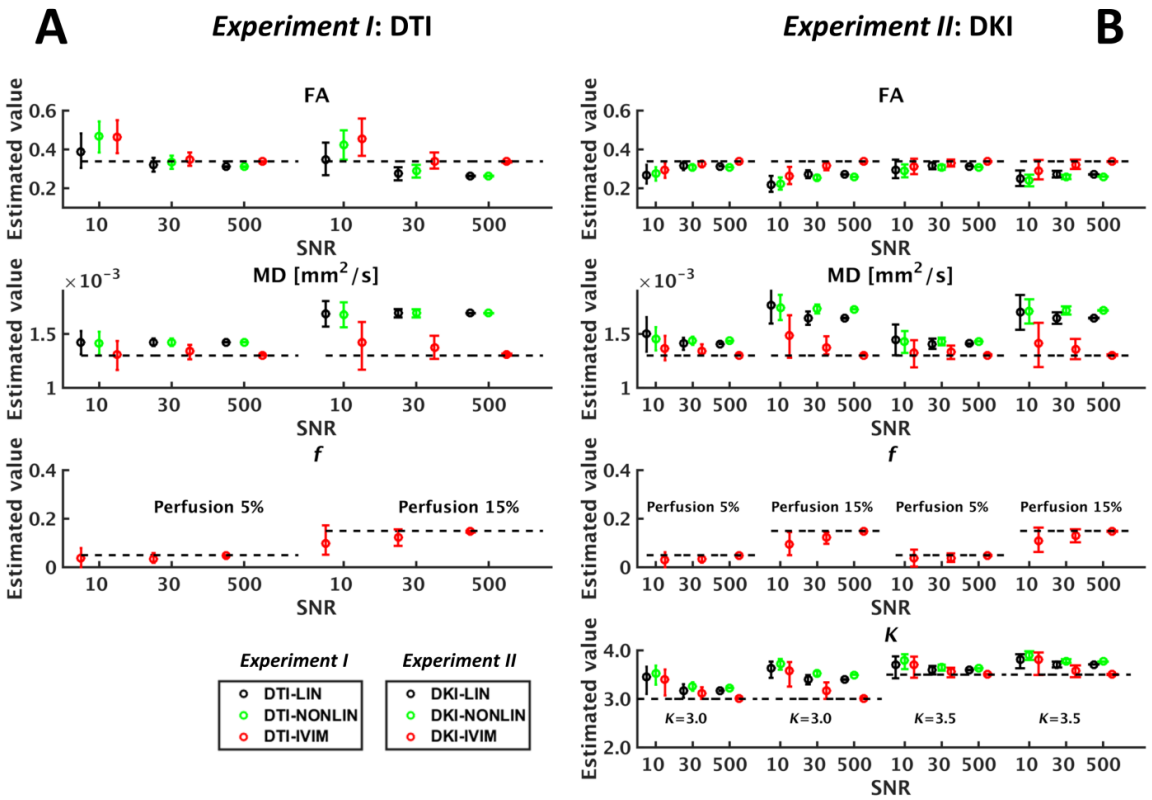

Figure 20 Results of simulations for *Experiment I* ((A) f=5% and f=15%) and *Experiment II* ((B) 4 simulations with f=5%, 15% and K=3, 3.5) for SNR levels 10, 30 and 500. The points represent the median values and the error bars the 25 and 75 percentile. Dashed black lines are the imposed values for the simulated setting. If sufficient SNR is provided, IVIM corrected models can correctly recover the imposed values in both experiments. Non corrected models lead to biased estimations even at very high SNR. If IVIM is not included, blood perfusion influences estimations of FA, MD (DTI and DKI models) and K.

Differently from non-corrected DTI models, [DTI-IVIM] estimated FA and MD values close to imposed values, with biases at SNR=30 between 0.6% and 3.3% for FA and between 3.0% and 5.9% for MD. At very low SNR all models resulted in unreliable estimates, however values of MD using [DTI-IVIM] were closer to the imposed value. Simulations of *Experiment II*, shown in Figure 2B, prove that in analogy with *Experiment I*, *f*=5% led to biases in the estimation of FA (max -24.6%) and MD (max 33.3%) with [DKI-LIN] and [DKI-NONLIN]. Additionally, *K* was also overestimated up to +17.6%. Errors at SNR=30 were strongly reduced by the IVIM corrected model [DKI-IVIM], which resulted in maximum estimation errors of -7.1% for FA, +5.7% for MD and +5.8% for *K*. Moreover, the model asymptotically approaches true values, thus higher SNR results in less bias. For completeness, the relative errors at SNR=30 of the computed parameters for all simulations of both experiments are reported in **Table 7**

Table 7 – Relative errors of models in *Experiment I* and *Experiment II* for different simulated settings at SNR=30. The lowest errors for each simulation are highlighted in bold.

SNR=30					
Simulations - *Experiment I*: *DTI*					
		***f*=5%**	***f*=15%**		
[DTI-LIN]	**FA**	-5,0%	-18,9%		
	MD	9,6%	30,2%		
[DTI-NONLIN]	**FA**	**3,2%**	-14,8%		
	MD	9,5%	30,2%		
[DTI-IVIM]	**FA**	3,3%	**0,6%**		
	MD	**3,0%**	**5,9%**		
	f	-29,7%	-18,0%		
Simulations - *Experiment II: DKI*					
		***f*=5%,*K*=3**	***f*=15%,*K*=3**	***f*=5%,*K*=3.5**	***f*=15%,*K*=3.5**
[DKI-LIN]	***K***	5,9%	13,5%	2,9%	6,1%
	FA	-7,1%	-19,8%	-7,1%	-19,7%
	MD	8,5%	26,9%	8,4%	26,7%
[DKI-NONLIN]	***K***	8,7%	17,6%	4,3%	8,1%
	FA	-9,8%	-24,6%	-9,2%	-23,7%
	MD	10,6%	33,3%	10,1%	32,3%
[DKI-IVIM]	***K***	**3,6%**	**5,8%**	**1,6%**	**2,5%**
	FA	**-4,5%**	**-7,1%**	**-2,8%**	**-4,8%**
	MD	**3,4%**	**5,7%**	**2,5%**	**4,3%**
	f	-34,0%	-18,2%	-23,8%	-12,9%

Figure 21 shows an example of the dMRI data of one subject after pre-processing, as well as the ROIs used to segment the muscles. The overall data quality was adequate, and the images at b=1300s/mm^2 still show consistent anatomical contrast. The average SNR of each shell was computed using the noise measurement as reference, and was 46±4 at b=0s/mm^2, 45±4 at b=2s/mm^2, 44±4 at b=5s/mm^2, 44±4 at b=10s/mm^2, 43±4 at b=20s/mm^2, 40±3 at b=50s/mm^2, 37±3 at b=100s/mm^2, 31±3 at b=200s/mm^2, 23±2 at b=400s/mm^2, 15±1 at b=700s/mm^2, 10±1 at b=1000s/mm^2, 7±1 at b=1300s/mm^2. The presence of residual artifacts was visually assessed and no chemical shift artifacts were observable, however 1 to 3 signal dropouts on 136 volumes were noticed. After pre-processing, MRI data was fitted as reported in the Methods section to obtain parametric maps, as reported in **Figure 22**.

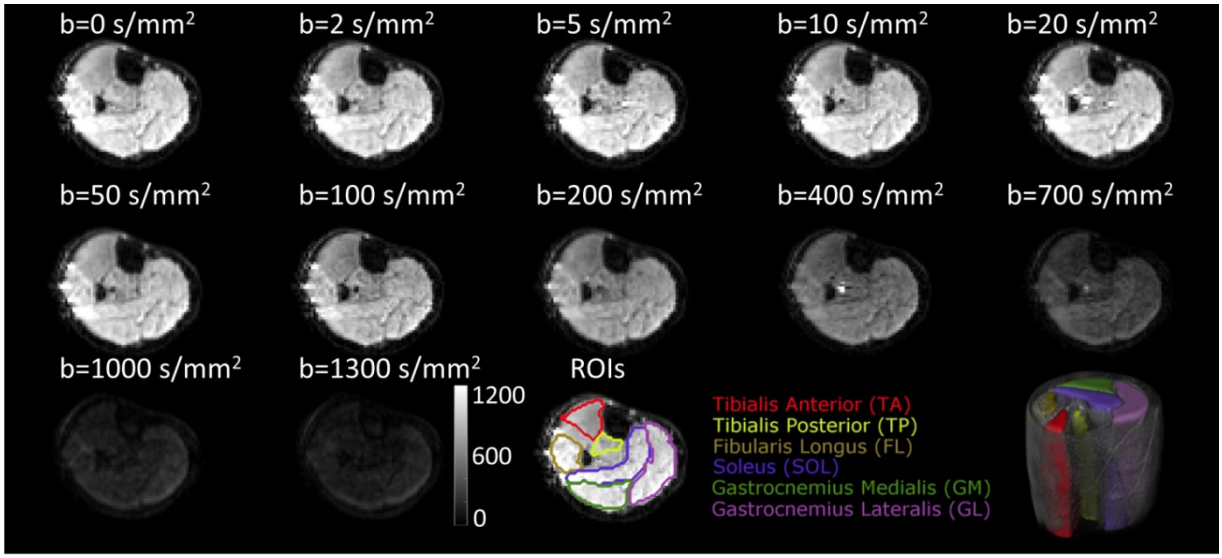

Figure 21 Example of acquired data showing a middle slice for each acquired b-value, including the non-weighted image. All the slices are shown with the same MRI signal range (in arbitrary units), as represented by the gray scale bar. Last image shows the color based representation of the ROIs over imposed to the b=0s/mm^2 image. The bottom right corner shows a 3D rendering of the acquired FOV and the ROIs inside the calf volume.

All estimated b=0s/mm^2 matched the corresponding average measure, and FA, MD, K and f maps were homogeneous inside the muscle volume (green solid line in **Figure 22**). D^* maps were more prone to noise than those of the other parameters, especially in correspondence of f values approaching 0, where the estimation of D^* becomes ill-conditioned. Blood vessels can be identified as bright spots on MD maps of non-IVIM corrected, but not on MD maps of [DTI-IVIM] and [DKI-IVIM]. Compared to the first, the latter were flatter and lower valued, in line with simulations. Blood vessels can instead be retrieved on the f maps of IVIM models, consistently with the formulation of the models. Kurtosis maps were consistent

across DKI models, but those estimated with [DKI-LIN] had voxels with $K<3$ (negative kurtosis when defined as excess kurtosis) in lower SNR regions.

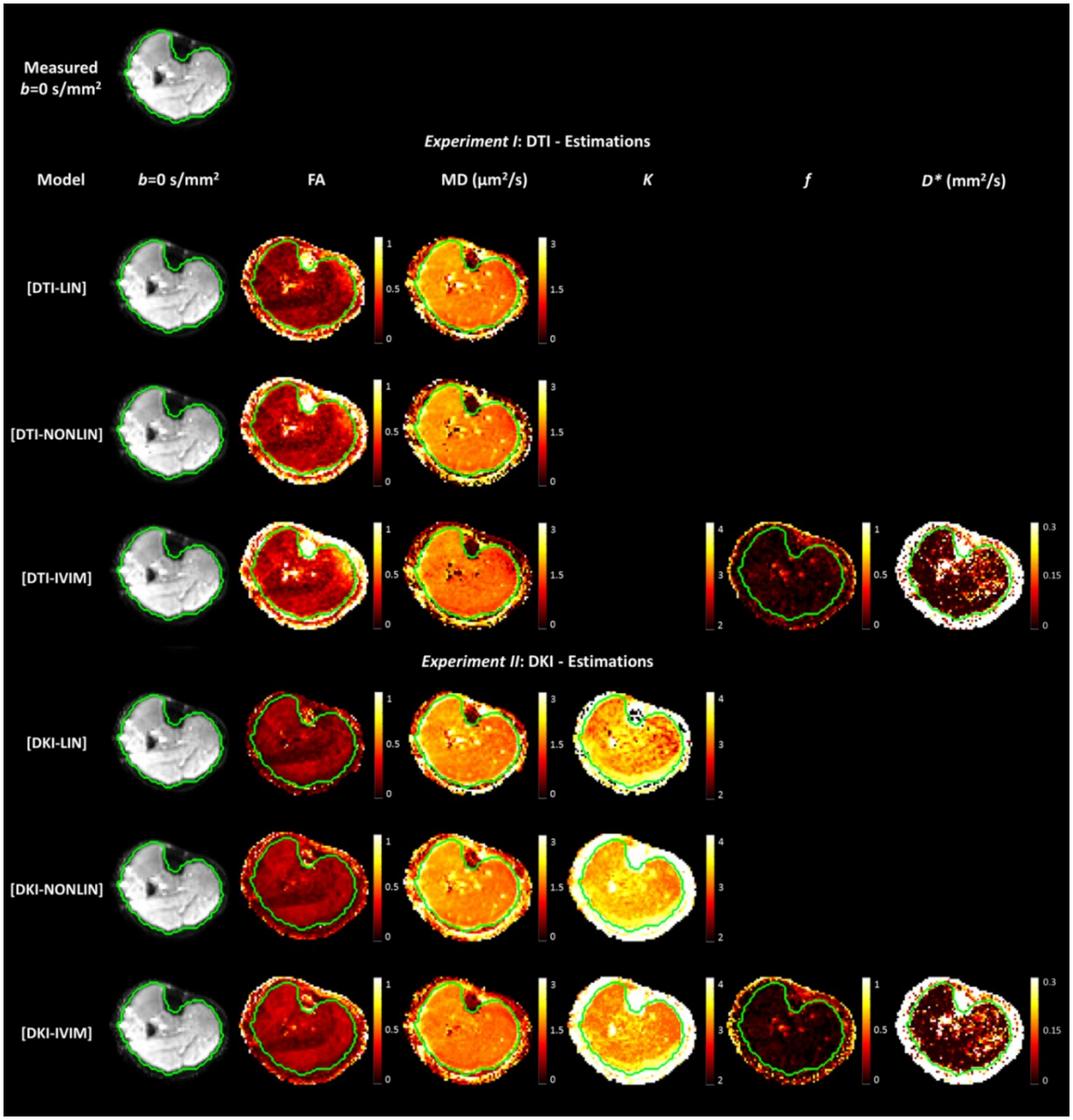

Figure 22 The first row is the average b=0s/mm^2 of all measurements. Solid green lines contour the muscle area of the calf. The other rows show an example of the parameter estimations obtained on the same slice with the three DTI (*Experiment I*) and the three DKI (*Experiment II*) based methods. MD maps of [DTI-IVIM] and [DKI-IVIM] are characterized by lower and more heterogeneous values (row 4 and 7, column 3). Similar observations are valid for K maps of [DKI-IVIM] (row 7 column 4). The agreement between the estimated b=0s/mm^2 and the measured map is noticeable for all the models, as is the global quality of the parameter maps. All the parametric maps show spurious values in correspondence of the subcutaneous fat due to its inherently low SNR. Some residual olefinic fat can be noticed in the K map in the Gastrocnemius area. D^* maps show higher values in correspondence of blood vessels and some bright spots when f values approach zero.

The *K* map from [DKI-IVIM] showed lower values in the vessel regions while the high kurtosis values over muscles GM and GL were preserved. The analysis of the fit residuals showed that they were normally distributed in 96.3% of the total voxels (Shapiro-Wilk test) with zero mean in 99.8% of the total voxels (one sample t-test). Some outliers corresponding to spontaneous signal dropouts were revealed by inspection of the residuals, however being maximum 3 on 136 volumes they did not influence the fit results. The average SD measured was between 2.1% and 4.7% of the average b=0s/mm^2, while the average SD computed a posteriori from the residuals of all models was between 3.7% and 13.3% of the average b=0s/mm^2 data. The CVs of the parameters were generally less than 20% with the exceptions of cross-elements of the diffusion tensor D_{XY}, D_{XZ}, D_{YZ} and D^*.

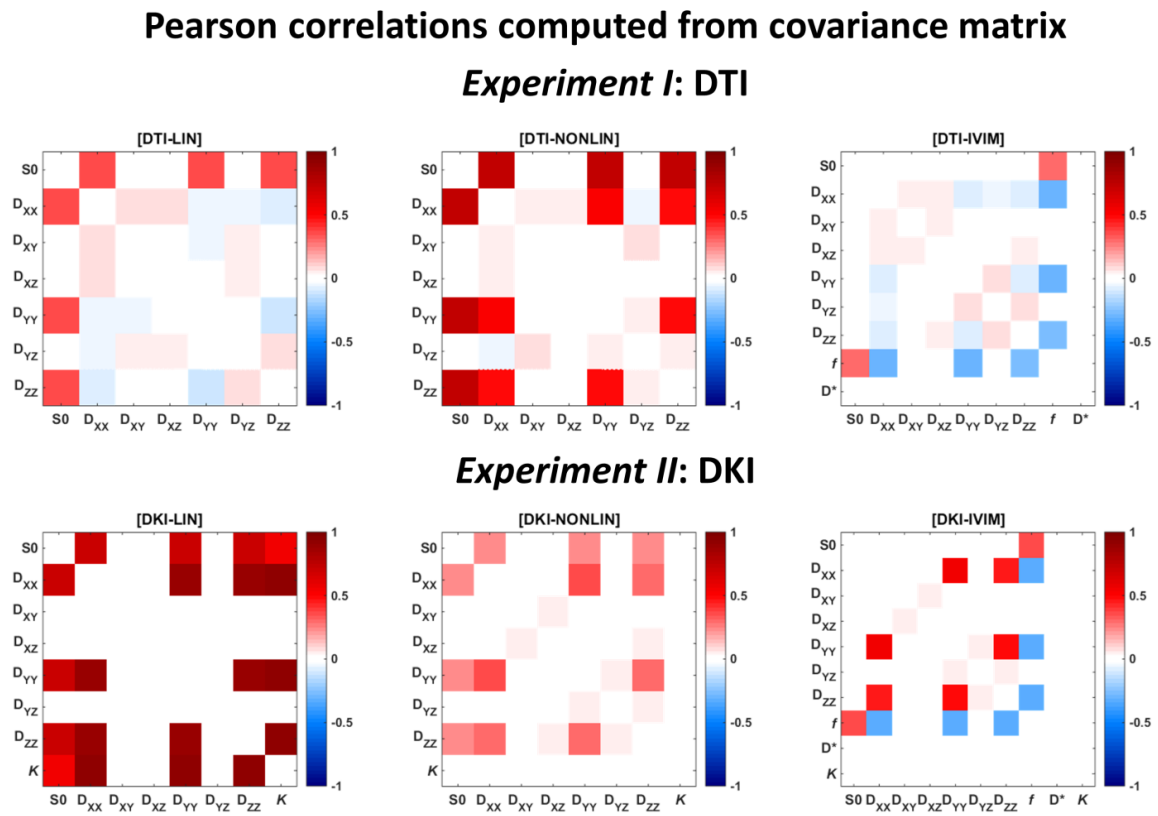

Figure 23 Pearson correlation matrices of the three DTI models in *Experiment I* and the three DKI models in *Experiment II*. Correlations were computed from the average covariance matrix associated to the ROIs of the subjects. Dependence of axial diffusivity elements on the non-weighted image was revealed for [DTI-LIN], [DTI-NONLIN], [DKI-LIN] and [DKI-NONLIN]. Additionally, *K* estimations from [DKI-LIN] depended on S_0. Inclusion of IVIM in [DTI-IVIM] and [DKI-IVIM] removed the effect of S0 on D_{XX}-D_{YY}-D_{ZZ} and on K ([DKI-IVIM]).

The mean CV of D_{XY} varied from 94% ([DKI-NONLIN]) to 250% ([DTI-NONLIN]); the mean CV of D_{XZ} was between 51% ([DKI-NONLIN]) and 125% ([DTI-NONLIN]); the mean CV of D_{YZ} was between 48% ([DKI-NONLIN]) and 122% ([DTI-NONLIN]). The average CVs of D^* were 106% for [DTI-IVIM] and 79% for [DKI-IVIM].

The Pearson correlations between the parameters were computed from the covariance matrices, and are shown in **Figure 23**. Estimates of the non-weighted signal S_0 were strongly correlated with the estimates of the diagonal diffusivity elements D_{XX}-D_{YY}-D_{ZZ} for all models except [DTI-IVIM] and [DKI-IVIM]. Given that the signal of blood is generally hyper-intense compared to that of tissues due to its longer T_2, these cross-correlations explicitly link increments of S_0 to increments of diffusivity. Interestingly, [DTI-IVIM] and [DKI-IVIM] showed no cross-correlation between S_0 and elements of the diffusion tensor or K (that was instead strongly correlated with S_0 for [DTI-LIN]). For these models f correlated positively with S_0 (supporting the observation on the T_2 of blood) and negatively with the diffusion tensor elements. Despite the relatively high number of free parameters of [DKI-IVIM], most of them were not correlated, and in particular K was not correlated with any of the others. The only exception to this observation was represented by the axial diffusivity elements, although this could be ascribed to the apparent low anisotropy of muscle cells, where increments of diffusivity in one direction are probably linked to increments in the other two spatial directions. All these findings represent an important theoretical basis for the correlation analysis we later performed, as no model effects appear to artificially boost the estimates. The 25, 50 and 75 percentile of FA, MD, f (only for [DTI-IVIM], [DKI-IVIM]) and K (*Experiment II* only) were computed for each ROI and time-point, resulting in the colored areas shown in **Figure 24**. Only voxels within the agreement masks, that included 24 to 28 (out of 30) common slices, were included in the statistical analysis. Results of the three DTI models employed in *Experiment I* (**Figure 24A**) were in agreement with simulations, and [DTI-IVIM] estimated lower, less variable MD values and higher FA values compared to non-corrected DTI models. Similarly, in *Experiment II* (**Figure 24B**) [DKI-IVIM] estimated lower MD and K values, and higher FA compared to [DKI-LIN] and [DKI-NONLIN], in line with simulations. The perfusion signal fraction was mostly between 0.02 and 0.18 in the muscle ROIs, while D^* values were between 0.01 (lower bound of the constraints) and 0.2mm^2/s (data not shown in this text). From both experiments it was noticed that high values of f estimated by the IVIM-corrected models matched high MD values of the non-corrected models.

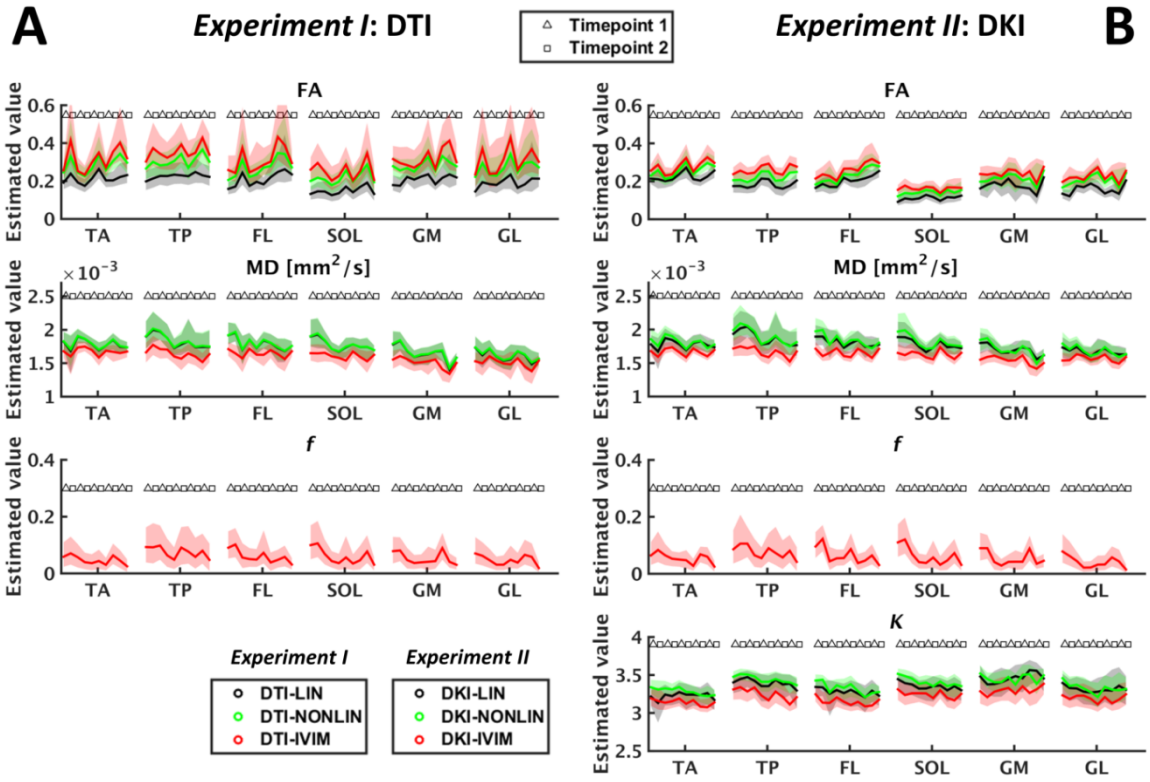

Figure 24 Shaded areas delimit values between the 25 and the 75 percentile interval of FA, MD, *f* and *K* (B only) for the six considered ROIs. Solid lines are the corresponding median values. Percentiles were computed for each time point of the five acquired subjects, resulting in 10 values for each ROI. A and B show the results respectively for the three different DTI (*Experiment I*) and DKI (*Experiment II*) models. Perfusion signal fraction estimations from models [DTI-IVIM] and [DKI-IVIM] were similar with values mostly between 5% and 10%. Compared to non-IVIM models (black and green), MD estimations from the IVIM models (red) were lower and more constant across time-points and subjects (second row), while FA values were higher (top row). For *Experiment II*, *K* estimated from IVIM-corrected models was lower, as was expected from simulations results.

MD_{LIN} was computed by linear regression of the data at b=200s/mm^2 and b=700s/mm^2, then its correlation with MD of the six models were computed, as reported in **Figure 25**. All correlations were significant for both DTI and DKI models. However, the highest correlations were observed for [DTI-IVIM] and [DKI-IVIM]. The slopes of the linear regressions of [DTI-LIN] and [DTI-NONLIN] (*Experiment I*, **Figure 25A**) were 1.20 and 1.18 respectively, and a positive offset on the y-axis was noticeable. In contrast, the regression line of [DTI-IVIM] had an almost unitary slope (1.05) and had the smaller vertical offset compared to [DTI-LIN] and [DTI-NONLIN]. Correlations with models of *Experiment II* (**Figure 25B**) showed similar results, with all the models estimating greater values of MD than DTI models due to the presence of *K* in the formulation. Both [DKI-LIN] and [DKI-IVIM] had an almost

unitary slope, however, MD values of the first had a greater vertical offset than those of the latter.

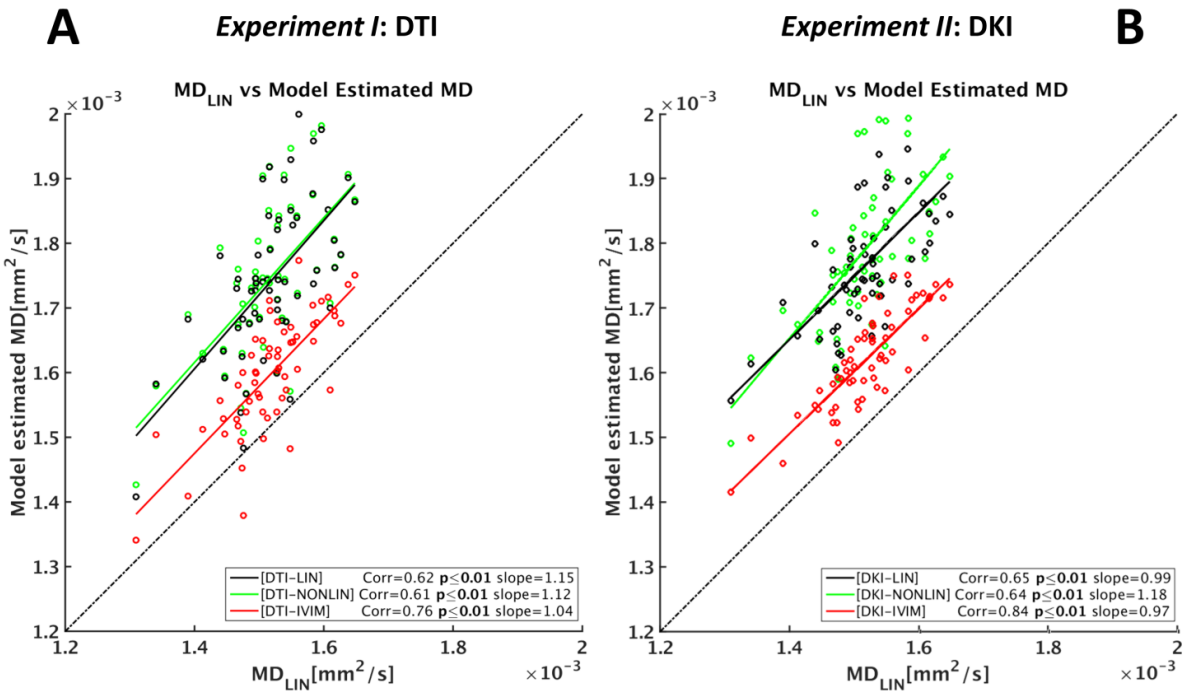

Figure 25 Points represent median MD values of each muscle ROI of all subjects computed with the three models in *Experiment I* (A) and the three models in *Experiment II* (B). On the x-axis, the corresponding median MD values computed from b=200s/mm^2 and b=700s/mm^2 is reported. Solid lines represent the linear regression of the estimates; the dashed black line is the ideal line. (A) [DTI-LIN] and [DTI-NONLIN] have a regression slope 20% greater than the ideal line and a positive offset. [DTI-IVIM] results in the higher Pearson correlation, regression slope more close to 1, and the smallest offset. (B) [DKI-IVIM] shows the highest correlation, slope close to 1, and the smallest vertical offset among DKI models.

The results of the correlation analysis between f estimated with [DTI-IVIM] and the DTI parameters FA, MD, AD and RD of *Experiment I* are shown in **Figure 26A**. All parameters estimated with [DTI-LIN] and [DTI-NONLIN] except for FA positively correlated with f, meaning that they linearly increased with the signal fraction of blood. Conversely, none of the parameters from [DTI-IVIM] showed significant correlations. Inter-scan reproducibility of FA, MD, AD, RD and f was evaluated with Bland-Altman plots, as reported in **Figure 26B**. The mean differences between two measures were close to zero and none of the distributions showed any trend. Repeatability indices of all models were very similar, and can be found in **Table 8**.

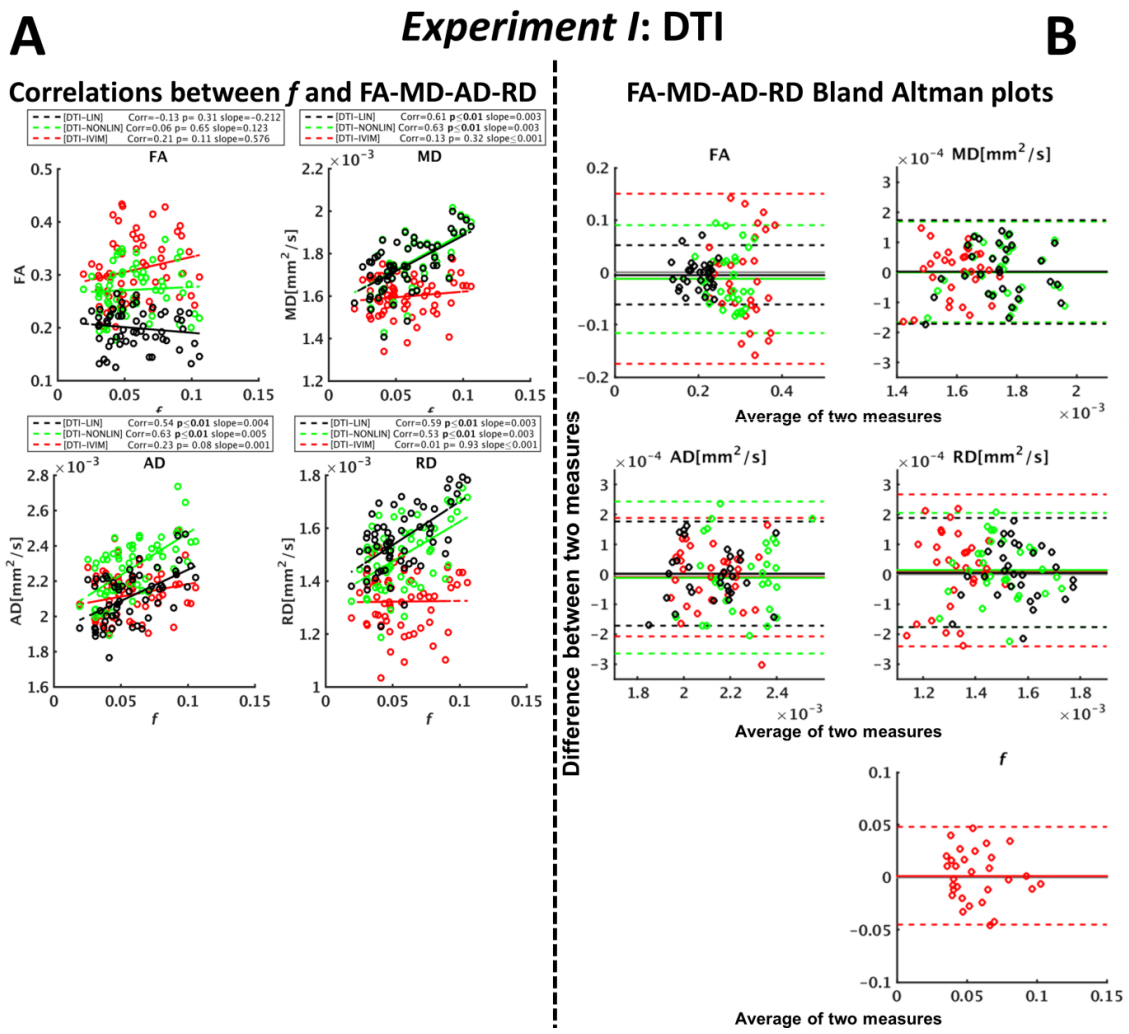

Figure 26 A) the correlation of *f* with FA, MD, AD and RD for *Experiment I*. Points are the median value for each ROI of the six muscle ROIs from both measurements of all five subjects (60 points in total). IVIM correction removed the correlation between *f* and MD-AD-RD, that was significant and high for both non IVIM models (i.e. [DTI-LIN] and [DTI-NONLIN]). The linear regression slope for model [DTI-IVIM] was less than 4 times those of the non-corrected models (0.001 versus 0.003 and 0.004). FA was not correlated with f for all the considered models. B) Bland-Altman plot of MD-AD-RD and *f*. The points represent the pair of values for each of the six muscle ROIs and for each of the 5 subjects (30 points in total). Solid lines show the mean of the difference for each model, dashed lines delimit the 95% confidence interval. No trends appear visible for any of the considered models, and the average time-point variation of MD, AD and RD is close to zero.

Table 8 – Reproducibility analysis of MD, AD, RD) for *Experiment I*.

Bland Altman analysis *Experiment I: DTI*				
		Mean	**CR(1.96xStd)**	**RI**
[DTI-LIN]	**MD(x 10^3)**	0,002	0,172	9,9%
	AD(x 10^3)	0,003	0,175	8,3%
	RD(x 10^3)	0,005	0,183	11,7%
[DTI-NONLIN]	**MD(x 10^3)**	0,001	0,167	9,6%
	AD(x 10^3)	-0,012	0,254	11,2%
	RD(x 10^3)	0,014	0,191	12,8%
[DTI-IVIM]	**MD(x 10^3)**	-0,001	0,167	10,5%
	AD(x 10^3)	-0,010	0,198	9,3%
	RD(x 10^3)	0,012	0,254	19,2%

The same analysis was repeated for *Experiment II*, as reported in **Figure 27A**, that shows the correlations between *f* estimated by [DKI-IVIM] and *K*, FA, MD, AD and RD. In addition to significant correlations between *f* and MD, AD and RD, the [DKI-LIN] and [DKI-NONLIN] showed a significant correlation between estimations of *f* and *K*. In line with *Experiment I*, the correlations were lost when IVIM correction was performed. Indeed, none of the metrics provided by [DKI-IVIM] was correlated to the perfusion signal fraction. Inspection of Bland-Altman plots (**Figure 27B**) revealed that the mean differences between two measures were close to zero for all estimated values, and no trends were visible. A small offset in the inter-scan difference (y axis) was observed for *K*. The confidence interval of [DKI-IVIM] was comparable to that of [DKI-NONLIN] for diffusivity parameters but greater for *K*. Repeatability indices of the Bland-Altman analysis of *Experiment II* are reported in **Table 9**.

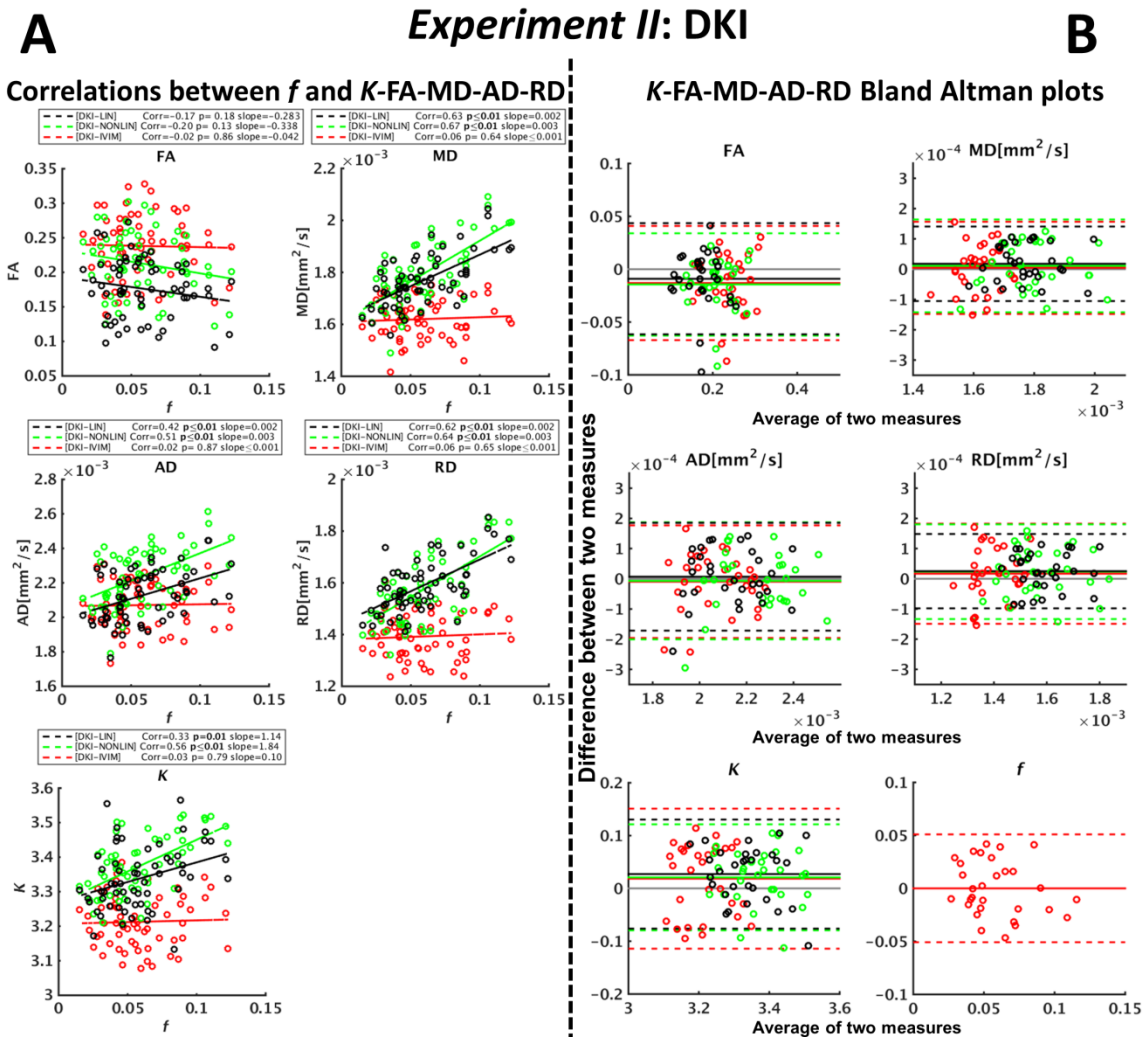

Figure 27 A) Correlations of *f* with K-MD-AD and RD for the models in *Experiment II*. Points are the median value of the estimates for each ROI. IVIM correction eliminated the correlation between *f* and diffusivities, as well as the correlation between *f* and *K*. Correlations were instead significant and considerable for all non-corrected models. B) Bland-Altman plot of *K*, MD,AD,RD and *f*. The points represent the values of the six muscle ROIs for each of the 5 subjects (30 points in total). Solid lines show the mean of the difference for each model, dashed lines delimit the 95% confidence interval. No trends appeared visible for any of the considered models, and the average time-point variation of MD, AD and RD was close to zero. A small offset was revealed for *K*, independently from the considered model.

Table 9 – Reproducibility analysis of MD, AD, RD and *K* for *Experiment II*.

		Bland Altman analysis		
		Experiment II: DKI		
[DKI-LIN]	**MD(x 10^3)**	0,018	0,123	7,0%
	AD(x 10^3)	0,007	0,178	8,4%
	RD(x 10^3)	0,025	0,123	7,7%
	K	0,027	0,103	3,1%
[DKI-NONLIN]	**MD(x 10^3)**	0,011	0,153	8,5%
	AD(x 10^3)	-0,007	0,194	8,7%
	RD(x 10^3)	0,024	0,157	10,0%
	K	0,021	0,100	3,0%
[DKI-IVIM]	**MD(x 10^3)**	0,004	0,154	9,5%
	AD(x 10^3)	-0,010	0,186	9,0%
	RD(x 10^3)	0,017	0,166	11,9%
	K	0,018	0,133	4,1%

Figure 28A shows the correlation between *K* and MD, AD and RD for the [DKI-IVIM] model. MD and AD estimations showed significant correlations with *K* only for [DKI-NONLIN] and for [DKI-IVIM] respectively. Conversely, RD estimations were consistently correlated to *K* with all three models. Although some of the correlations were significant ($p<0.05$), the correlation coefficients were low, with values between 0.3 and 0.42 and the dispersions around the regression line were considerable. Moreover, perfusion did not appear to consistently affect the relationship between tensor derived quantities and kurtosis, as correlations were similar for all considered models. Relative inter-scan variations δMD, δAD, δRD and δK were computed for each pair of time-points with [DKI-IVIM], after which the correlation between δK and each diffusion parameter variation was evaluated (see **Figure 28B**). Although the range of δK was modest, between -4% and 4%, significant and strong positive correlations of δK with δMD, δAD and δRD were consistent independent from the used fitting algorithm (except for δAD-δK with [DKI-LIN]). The correlation was the strongest when IVIM correction was included.

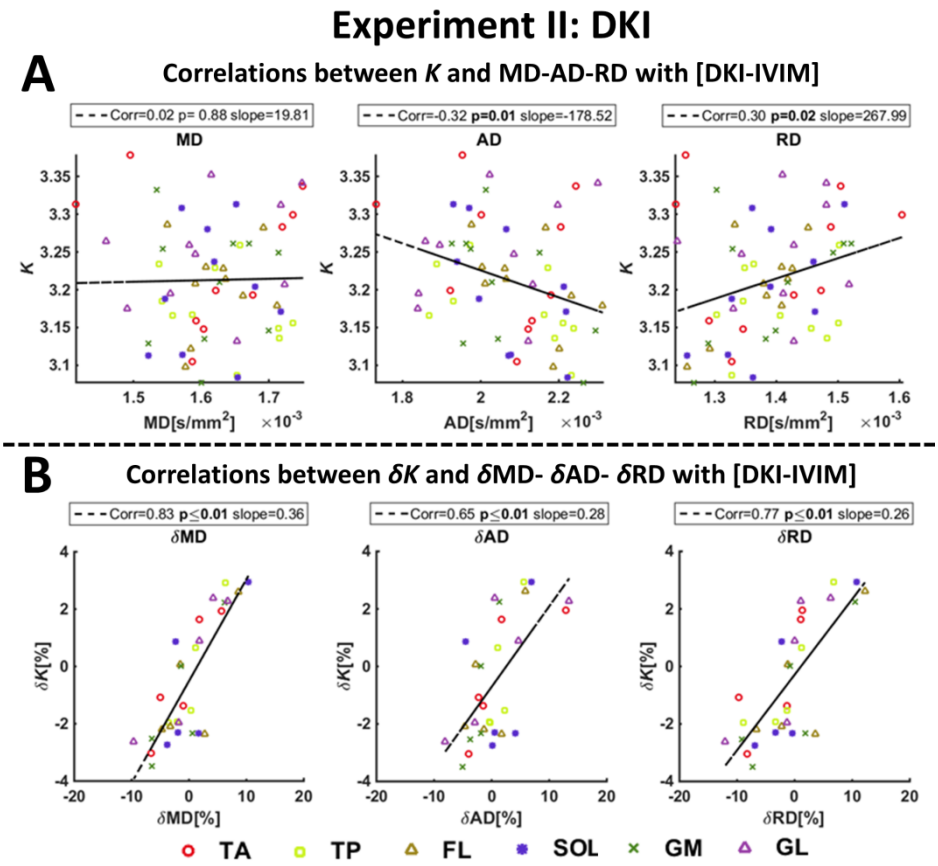

Figure 28 A) Correlations between *K* and MD, AD, RD, for [DKI-IVIM]. Points are the median value of estimates for each of the six muscle ROIs. The black dashed line is the linear-regression line. MD did not show consistent correlations with *K*. In contrast, RD was positively correlated with *K* while AD negatively. B) Correlations between δK and δMD, δAD, δRD for [DKI-IVIM]. Points are the relative inter-scan difference between corresponding median values of the estimates for each of the six muscle ROIs. A strong correlation between δMD, δAD, δRD and δK was revealed.

Conclusions

In this study we show that the contribution of the micro vascular network to the diffusion signal is non-negligible and that it should be considered as a potential bias source for DTI and DKI estimates. To perform an appropriate analysis, we employed an extensive acquisition protocol, that may be shortened to obtain bias free tensor fit, quantify *f* and *D** in clinically acceptable times. These parameters do not just describe a potential artifact source but also a biological process that can be of interest when investigating the dynamics of perfusion after exercises (Froeling et al., 2015; Hiepe et al., 2014; Nguyen et al., 2016) or in presence of disease (Bane et al., 2016; Concia et al., 2014; Schneider et al., 2016). Considering that DTI is often used to perform group comparisons, the nuisance effect of *f* could further increase the variance of diffusion metrics within groups and reduce statistical power. Additionally, in presence of diseases characterized by permanent alterations of *f*, the usage of non-perfusion

corrected models would result in over/under estimation of the diffusion metrics with consequent misinterpretation of the underlying micro-structural process. Numerical simulations showed that not-accounting for perfusion leads to systemic over-estimation of MD and under-estimation of FA proportionally to the perfusion signal fraction. The biases observed for [DTI-LIN] and [DTI-NONLIN], that are commonly used DTI schemes, are in the order of magnitude of FA and MD alteration revealed by DTI in a population affected by Duchenne dystrophy (Hooijmans et al., 2015). The simulations also showed that data at adequate SNR is mandatory to obtain meaningful estimates, therefore an SNR equal or greater than 30 is strongly recommended. Higher SNR values are still beneficial for the accuracy of f and K in model [DKI-IVIM], especially if the fit is performed with standard NNLS. Results obtained on MRI data were in line with results of simulations. The estimated perfusion signal fraction was between 0 and 20%, well matching the simulated f=5% and f=15% values used in simulations. MD values estimated with [DTI-IVIM] and [DKI-IVIM] were lower and more constant across subjects and ROIs than estimations of non IVIM-corrected models. Furthermore, MD values from IVIM-corrected models were similar to MD_{LIN} and with the smallest offsets if compared to MD from the others. Interestingly, previous studies reported higher MD values from DKI models compared to DTI (Cheung et al., 2009; Veraart et al., 2011; Wu & Cheung, 2010), thus justifying the residual vertical offset of [DKI-IVIM].

Experiment II proved that perfusion affects DKI estimates similarly to DTI and has an effect on the estimation of kurtosis. To conclude, some limitations of this work should be mentioned. The limited number of subjects does not allow a comprehensive description of the healthy population, although the effects of age and gender on DTI estimates have already been investigated. In this work only isotropic IVIM and isotropic kurtosis were considered in order to reduce model complexity, however, a recent work (Karampinos, King, Sutton, & Georgiadis, 2010) highlighted the potential anisotropy of IVIM, and kurtosis is known to be direction dependent. The anisotropy of IVIM might affect the anisotropic part of the diffusion tensor, but should not bias the quantification of MD. Even if these approximations should be sufficient to extensively characterize the effects of perfusion on DTI and DKI estimates, further investigations on direction dependent effects may be of interest.

CHAPTER VI: NON-EXPLICIT MODELING OF BRAIN DIFFUSION REGIMES FOLLOWING A BLIND DECONVOLUTION APPROACH.

Introduction

In the previous chapters, multi-compartment modeling of the dMRI signal was presented as an effective way to overcome the limitations of the DTI model and to derive additional parameters, potentially delivering higher specificity to the different components of the tissues. One of the problems often faced when designing multi-compartment models is the choice of the optimal number of components, that is intrinsically voxel dependent due to the heterogeneity of the biological environment. A possible strategy is to follow some established model design criteria as the Akaike Information Criteria or the Bayesian Information Criteria, although these techniques do not necessarily converge to the "most physiological" model. Fitting each voxel with a different model is not a viable way as it potentially leads to incomparable metrics, therefore a globally optimal model is often chosen and used for the whole data. Recently, some approaches as the "Semi-Continuous Multi-Compartmental IVIM model" (Keil, Madler, Schild, & Hadizadeh, 2015; Madler & Coenen, 2013; Madler, Hadizadeh, & Gieseke, 2013) have been proposed to infer the optimal number of components directly from the data. The purpose of the study included in this chapter, which preliminary results have been presented at the "ISMRM Diffusion Workshop 2016" (Alberto De Luca, Bertoldo, Arrigoni, et al., 2016), is to generalize a similar approach to investigate the diffusion compartments in the brain using dMRI data acquired with two different sequences. In particular, data acquired with classic PGSE and with Flow-Compensated Asymmetric Bipolar gradients is fit with a dictionary based blind deconvolution approach, to corroborate the applicability of this technique to different sequences and to characterize their intrinsic signal differences.

Theory

The PGSE sequence has been introduced in Chapter I as an extension of the Spin-Echo with sensitization to molecular displacement. Computation of the first and second order derivatives of the gradients shows that the sequence is sensitive not only to displacement but also to velocity (1^{st} derivative) and accelerations (2^{nd} derivative), thus phenomena as vascular

motion, brain pulsatility, breath, patient motion, etc. Named G(t) the employed gradient waveform as function of time, the moments of order 0, 1 and 2 are respectively:

$$m_0 = \int_0^{TE} \gamma G(t) dt \quad [60]$$

$$m_1 = \int_0^{TE} \gamma t G(t) dt \quad [61]$$

$$m_2 = \int_0^{TE} \gamma t^2 G(t) dt \quad [62]$$

The left column of **Figure 29** shows a schematic representation of three gradients design used for diffusion sensitization, respectively Stejskal-Tanner (used in this study), 1st order compensated bipolar gradients and 2nd order flow compensated asymmetric bipolar gradients (used in this study).

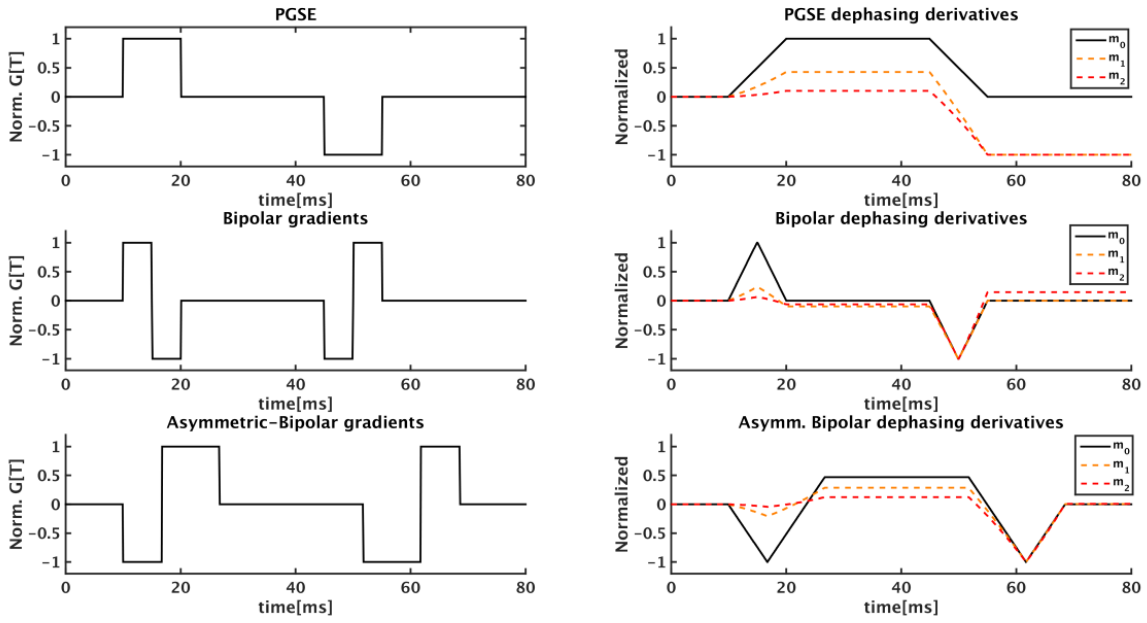

Figure 29 Left column is a schematic representation of diffusion gradient design for the Stejskal-Tanner Pulsed-Gradient Spin Echo (PGSE) (first row), the bipolar gradients (middle row) and the asymmetric-bipolar gradients (last row). Right column shows the phase accumulation (signal attenuation) of a static spin due to derivatives of order 0 (m_0, displacement), 1 (m_1, velocity) and 2 (m_2, acceleration). The PGSE signal suffers extra attenuation from phenomena as bulk motion. The bipolar gradient design suppresses contributions from the first order, while appropriate design of the asymmetric-bipolar profiles allows to achieve full suppression of derivatives up to the second order.

The right column of **Figure 29** shows the cumulative dephasing of the signal due to motion, velocity and acceleration. Bipolar gradients can effectively suppress the contribution of

velocity but not acceleration, that is achieved only by the complete asymmetric-bipolar design. Previous works investigated the applicability of this gradient scheme in the context of IVIM (Wetscherek, Stieltjes, & Laun, 2015) and cardiac dMRI (Stoeck, von Deuster, Genet, Atkinson, & Kozerke, 2016). The fit of the dMRI signals (S) and the simultaneous compartmental decomposition were performed with a technique based on the Pseudo-Continuos Multi-Compartment deconvolution (Madler & Coenen, 2013). For this purpose, a dictionary of diffusion signals (U) with 300 entries was built. Each column of U represented an isotropic Gaussian decaying signal with diffusion coefficient in the log-spaced range [0.1-1000]x$10^{-3}$$mm^2$/s. A constant column representing zero diffusion was added to the dictionary to account for plateauing of the signals at strong diffusion weightings (similarly to Kurtosis). The diffusion spectrum (χ) was computed with L_2 regularized non-negative least squares (NNLS):

$$\begin{cases} \chi = \min_{\hat{\chi}} \|U\hat{\chi} - S\|_2^2 + \gamma\|\hat{\chi}\|_2^2 \\ U\hat{\chi} \geq 0 \end{cases} \quad [63]$$

where γ is a regularization constant. The decomposition operation can be performed voxel-wise to obtain a diffusion spectrum for each voxel, then peaks can be either visually inspected or, if prior knowledge is available, integrated in specific diffusion ranges to isolate the contribution of different modes more conveniently. Named D_{INF} and D_{SUP} the lower and upper bounds of the diffusion interval of interest, its signal contribution (A_D) can be computed as:

$$A_D = \frac{\int_{D_{INF}}^{D_{SUP}} \chi(D)dD}{\int_0^{1mm^2/s} \chi(D)dD} \quad [64]$$

Data & Methods

Five healthy controls were acquired with a 3T MRI scanner (Philips Medical Systems) equipped with an 8ch head coil. The acquisition protocol included two multi-shell dMRI acquisitions, the first with Stejskal-Tanner (ST) gradients, the second with flow-compensated Asymmetric-Bipolar (AB) gradients. Echo Time (TE) and Repetition Time (TR) of both sequences were very similar, respectively TE=133/135ms and TR=9.4/9.5s while all the remaining parameters were identical, including SENSE=2.5 and resolution 2.5x2.5x2.5mm^3. The acquired gradient directions, identical for both acquisitions, included 3 orthogonal

directions at b=0,5,10,15,20,30,40,50,75,100,150,200,300,400,500,750s/mm^2 and 30 gradient directions at b=1000s/mm^2. Pre-processing of both sequences included affine registration of each volume to the first non-weighted to minimize motion and eddy currents artifacts with Elastix (Klein et al., 2010), then the b-matrix was rotated accordingly (Leemans & Jones, 2009). Additionally, the BET tool of FSL was employed to create a brain-only mask used in subsequent statistical analysis. The deconvolution step was performed in MATLAB R2013b using NNLS and imposing a regularization value γ=0.001, first averaging the signal of the whole brain to achieve very high SNR, then voxel-wise. The distribution of the voxel-wise deconvolution spectra was computed as mean + 2 standard deviation of the voxel-wise profiles. Voxel-wise fractional maps were created integrating the diffusion spectra in specific diffusion ranges, that were established by prior knowledge and observation of the whole brain diffusion spectra. In particular, the following diffusion intervals were integrated: [0.1,2]x10^{-3}mm^2/s corresponding to the tissue signal fraction, [2,6]x10^{-3}mm^2/s corresponding to the free water signal fraction, [6,1000]x10^{-3}mm^2/s corresponding to the vascular and micro vascular signal fraction.

Results

Figure 30 shows the whole brain deconvolution spectra and the voxel-wise distributions of each subject for both the ST and AB acquisition. Sharp but different peaks were observed in the whole brain spectra (**Figure 30**, columns 1 and 3) of ST and AB. For 4 out of 5 subjects four distinct peaks were consistently observed in ST, and their corresponding diffusion values were attributable to known biophysical sources. A first peak was located next to 0.6x10^{-3} mm^2/s, diffusion value close to that of the brain tissue. A second peak was close to 3.0x10^{-3} mm^2/s, diffusivity of free water at 37 degrees, while the last two peaks had values around 10 and 200mm^2/s, respectively diffusion values observed in the micro-vascular and vascular networks. The only remarkable difference was represented by the ST sequence of subject S1, for which only 3 peaks were observed. However, the first appears to be the average of the two observed for the other subjects. Only two peaks were observed for the AB gradients of all subjects, none above 10x10^{-3}mm^2/s, consistently with the intrinsic insensitivity of the sequence to bulk motion. However, even if the two observed peaks were similar across the five subjects, they were different from those observed with ST data. The averaging operations performed collapsing all voxels to a single enhances the SNR but might eventually introduce additional variability due to the spatial heterogeneity of the brain.

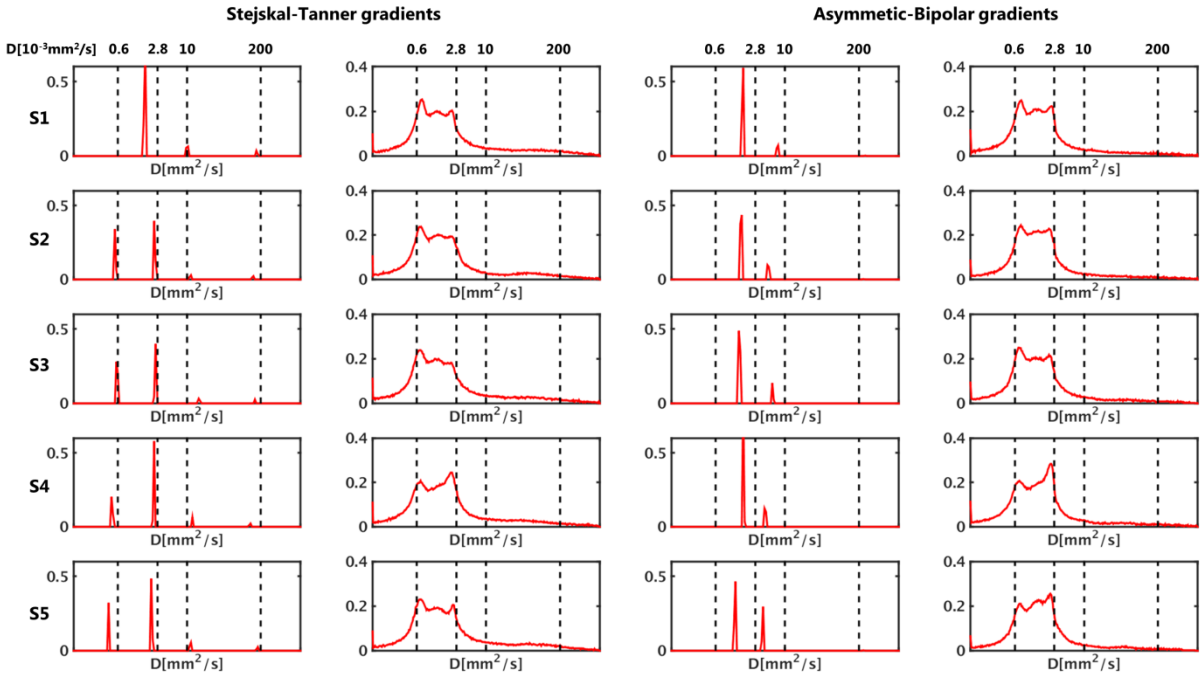

Figure 30 First and third columns show the diffusion spectra of the whole brain of 5 healthy subjects with ST and AB gradients respectively. Second and fourth columns are the mean + 2 standard deviation of the voxel-wise diffusion spectra. Four peaks were observed in average ST data (except for S1), two in the pseudo-diffusion range (IVIM), one close to the diffusivity of free water at 37°, and one assigned to the average diffusivity of tissues in the brain. Diffusion spectra of the average AB data showed no diffusion in the IVIM range, however, the two revealed peaks were different from ST. Voxel-wise spectra distribution were more similar across ST and AB data but not as sharp as the peaks of the averaged signal. Conversely, a continuum of compartments was observed.

For this reason, voxel-wise distributions, shown in columns 2 and 4 of **Figure 30**, might help providing a better characterization of the two sequences. Voxel-wise distributions appeared very similar across subjects and more consistent between ST and AB data. The peaks at $0.6x10^{-3}mm^2/s$ and $2.8x10^{-3}mm^2/s$ could still be distinguished with an additional peak around $1.3x10^{-3}mm^2/s$, however, diffusion compartments could not be segregated but conversely appeared as a continuum. Nonetheless, the tail of the AB distribution was remarkably lower than ST, although not completely null. Voxel-wise fraction maps were created integrating the diffusion spectra of each voxel in the diffusion intervals mentioned above, obtaining the maps reported in **Figure 31**. The maps were consistent across subjects and further highlighted the differences between ST and AB especially in the IVIM range, as the IVIM contribution was more visible for ST than AB. Overall all maps, including FW, had good agreement with the expected anatomy, although some noise artifacts were observable. Finally, tissue and FW maps were very similar between AB and ST.

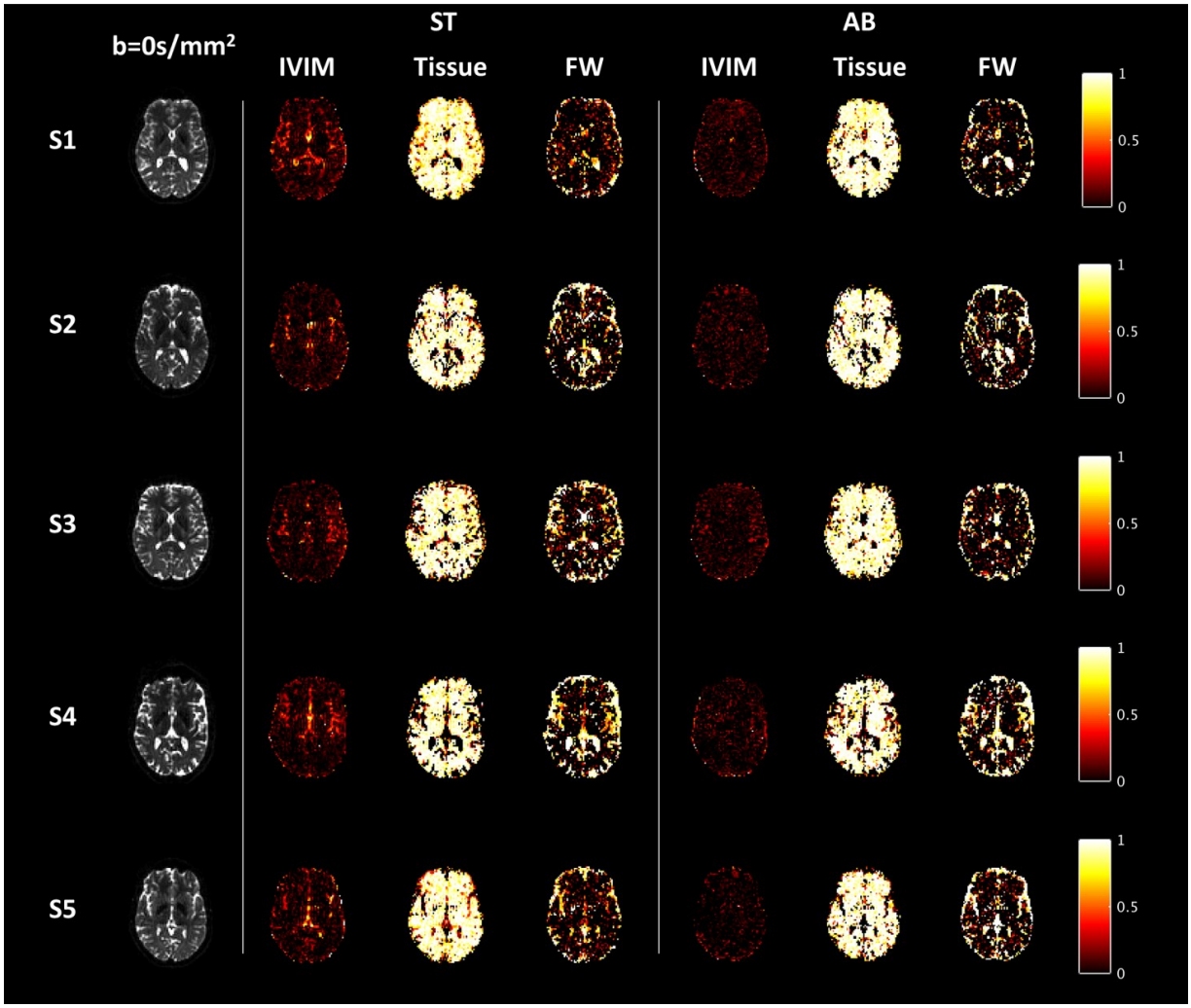

Figure 31 Fractional maps of IVIM, Tissue and FW obtained by integration of the ST-AB deconvolution profiles of each subject. Integration intervals were respectively $[6x10^{-3}, 1]mm^2/s$, $[1x10^{-4}, 2x10^{-3}]mm^2/s$, $[2x10^{-3},6x10^{-3}]mm^2/s$. The IVIM signal component of ST is consistently higher than AB, while FW is comparable.

Conclusions

In this work we proved the applicability of a regularized deconvolution approach to non-explicitly fit the dMRI signal with multiple compartments. The technique, that takes approximately one second per voxel, can be applied to both Stejskal-Tanner and flow-compensated gradients. Results are consistent with the specific properties of the sequences, in particular with the reduced sensitivity of AB to flow. The signal decomposition obtained at whole brain level was biophysically meaningful, especially on ST data, where all observed compartments could be ascribed to known physiological components of the brain tissue. This technique is potentially applicable to any district of the body as no hypothesis on the structure of the tissues are made, however, some limitations apply and should be further exploited in

future works. Firstly, in this work we did not deal with the optimization of the L_2 regularization parameter, however, it is expected to affect the results. Additionally, many works have shown that the L_1 penalty term is more parsimonious in the number of recovered components, although slower, as in contrast to L_2 regularization it does not have a closed form solution. Other solution techniques, as Monte Carlo Markov Chain or Genetic Algorithms could also be taken in consideration in place of NNLS to solve the matrix inversion. Finally, more should be investigated on the repeatability and consistency of the results, testing the consistency of the results across differently sampled data of the same subjects. In conclusion, this algorithm can be employed to quickly investigate diffusion regimes in the brain and eventually as a pre-processing tool to perform IVIM correction on the data before proceeding further processing with other techniques.

CHAPTER VII: OTHER RESEARCH ACTIVITIES

A connectivity study of Williams Syndrome

Williams syndrome (WS) is a neurodevelopmental disease caused by a genetic mutation that leads to the deletion of 20+ genes on the long arm of chromosome 7 (Francke, 1999; Jackowski et al., 2009; Martens, Wilson, & Reutens, 2008). Affected children are characterized by well-defined facial traits, mental impairment, low IQ but high verbal skills, and are very prone to sociality. Previous MRI studies of this disease mainly focused on volumetric analysis and Voxel Based Morphometry (VBM, (Ashburner & Friston, 2000)). Results point toward an overall reduction of gray matter volume in the frontal lobe, parietal lobe, temporal lobe, occipital lobe. Additionally, reduced volumes of the corpus callosum, cerebellum and brainstem have been reported. These findings arise the doubt of a lack of specificity of volumetric techniques in the characterization of the disease. Moreover, controversial reports of increased cerebellar and corpus callosum volumes have also been reported, further entangling the findings. Diffusion MRI application has also been partially explored in WS. Hoeft et al. (Hoeft et al., 2007) reported abnormal FA values in the right superior longitudinal fasciculus. Marenco et al. (Marenco et al., 2007) analyzed some major white matter bundles, including the inferior fronto-occipital fasciculus and the inferior and superior longitudinal fasciculus. They found increased anterior-posterior and reduced left-right fiber directionality compared to controls. Based on this evidence, that suggests dMRI as a promising explorative tool in WS, we performed a structural connectivity study of WS patients and healthy controls as attempt to provide a comprehensive description of brain structure alteration in this syndrome.

MRI acquisition was performed at 3T with a Philips Achieva scanner (Philips Medical System, The Best, Netherlands) on ten healthy controls (HC), 7 of which females, with mean age 23±5 years, and 9 patients affected by WS, 3 of which females, mean age 22±5 years). Acquired sequences included a high resolution T_{1W} FFE sequence, (voxel resolution 1x1x1mm^3, matrix size 256x256x160, T_E/T_R 3.86/8.40ms, SENSE 2), a T_{2W} TSE sequence (voxel resolution 1.5x1.5x1.5mm^3, matrix size 160x146x110, T_E/T_R 100/4700ms, SENSE 2, SPIR fat suppression) and a two-shell dMRI acquisition (voxel resolution 2.2x2.2x2.2mm^3, matrix size 112x112x80, T_E/T_R 100/8800ms, SENSE 2). The dMRI sequence featured 78 volumes acquired with Posterior-Anterior (PA) phase encoding (9 b=0s/mm^2, 16 directions at

b=300s/mm^2, 53 directions at b=1100s/mm^2) and 13 volumes (7 b=0s/mm^2, 6 directions at b=1100s/mm^2) acquired with the Anterior-Posterior (AP) phase encoding. T_{1W} data was processed with the N4 tool of ANTS (Tustison et al., 2010) to mitigate the intensity inhomogeneity bias, then skull removal and tissue type segmentation were performed with the FSL (Y Zhang et al., 2001) tools to obtain GM, WM and CSF partial volume maps. Both AP and PA dMRI data were pre-processed with the DIFFPREP module of TORTOISE (Pierpaoli et al., 2010) to remove motion and eddy current artifacts. Additionally, complete correction of EPI distortions was performed with DR-BUDDI (Irfanoglu et al., 2015) taking advantage of the AP and PA dMRI and of the T_{2W} acquisition. DR-BUDDI is a software package developed to work with TORTOISE that estimates the distortion field induced by B_0 field inhomogeneity (Andersson et al., 2003). The distortion field, constrained to act on the phase encoding axis, is computed by minimizing a two terms energy function. The first term minimizes the voxel-wise distance between tensors computed on the AP and PA data, while the second term forces AP and PA geometry to collapse on the distortion free T_{2W}. If the whole dMRI protocol is acquired with AP and PA encoding, both acquisitions are moved according to compensate the deformation field and their least-squares reconstruction is computed, thus enhancing data SNR. However, such acquisition scheme doubles the acquisition time, thus the choice of acquiring only a small amount of data in the AP encoding in our study. In this case, DR-BUDDI uses the deformation field to correct the geometric distortions of the PA data but no SNR boost is achieved.

After pre-processing, dMRI data acquired at b=0s/mm^2 and b=1100s/mm^2 was processed for the connectivity analysis. The first part of the connectivity pipeline consists in the creation of the individual tractogram, step that we performed with MRtrix (http://www.mrtrix.org, version 313) using the Constrained Spherical Deconvolution (CSD) approach (J-Donald Tournier et al., 2008). Even though CSD is generally performed with diffusion data acquired at b-values higher than 1100s/mm^2, this approach is still viable and is more robust to the crossing fibers problem compared to the DTI based fiber-tracking. The response function was computed for each subject using an FA threshold equal to 0.7 and a spherical harmonics decomposition of order 4, then CSD was performed on the data of each subject to reconstruct the corresponding Fiber Orientation Distribution (FOD). Fiber-tracking was performed using the iFOD2 (Jacques-Donald Tournier, Calamante, & Connelly, 2010) method and the default/optimized tracking parameters shipped with the package. 20 million streamlines were generated for each subject using the GM/WM interface (derived by MRtrix from the

GM/WM T_{1W} segmentation) as seed and the Anatomically Constrained Tractography (ACT,(R. E. Smith, Tournier, Calamante, & Connelly, 2012)) technique. The GM/WM seeding has been shown to reduce the influence of fiber bundles size on the final track density (Girard, Whittingstall, Deriche, & Descoteaux, 2014), while ACT ensures only anatomically feasible tracks are retained, i.e. tracks that connect two GM areas through WM. Spurious tracks terminating into CSF, into WM or never leaving GM are therefore not included in the tractogram. After the fiber-tracking step, the tractogram was filtered with the SIFT technique (R. E. Smith, Tournier, Calamante, & Connelly, 2013), pruning 10M of the 20M streamlines, obtaining the final 10M streamlines tractogram. The SIFT filtering ensures proportionality between the voxel-wise FOD and the streamlines count through each voxel. The AAL atlas (Tzourio-Mazoyer et al., 2002) was non-linearly registered to the diffusion space of each subject with ANTs using the T_{1W} and the T_{2W} image as intermediate targets, then connectivity matrices (connectoms) of each subject were built assigning the tracks to each node with a local search algorithm (maximum search radius 2mm). For the statistical analysis of the resulting group-wise connectivity matrices the Network Based Statistics package (NBS, (Zalesky, Fornito, & Bullmore, 2010)) was employed to perform two-sample one-sided t-tests. In particular, the tested metric was the normalized connection probability and the tests were corrected for multiple comparisons with FDR using a critical threshold equal to 0.05 and 50000 permutations. **Figure 32** shows an axial and a sagittal view of the connections that resulted statistically more probable in WS than HC. Most of the altered connections pointed out a posterior – anterior and intra-hemispheric pattern, while few different trans-hemispheric connections were observed, in line with previous works (Hoeft et al., 2007; Marenco et al., 2007). Most of the different connections originated from the bilateral superior occipital lobe, that appeared to be the prominent hub of these networks. Our results proved also an involvement of the right parahippocampal and calcarine areas, as well as of part of the cerebellum.

These results are now being collected in a manuscript that will be submitted to a peer reviewed international journal in the field of neurology.

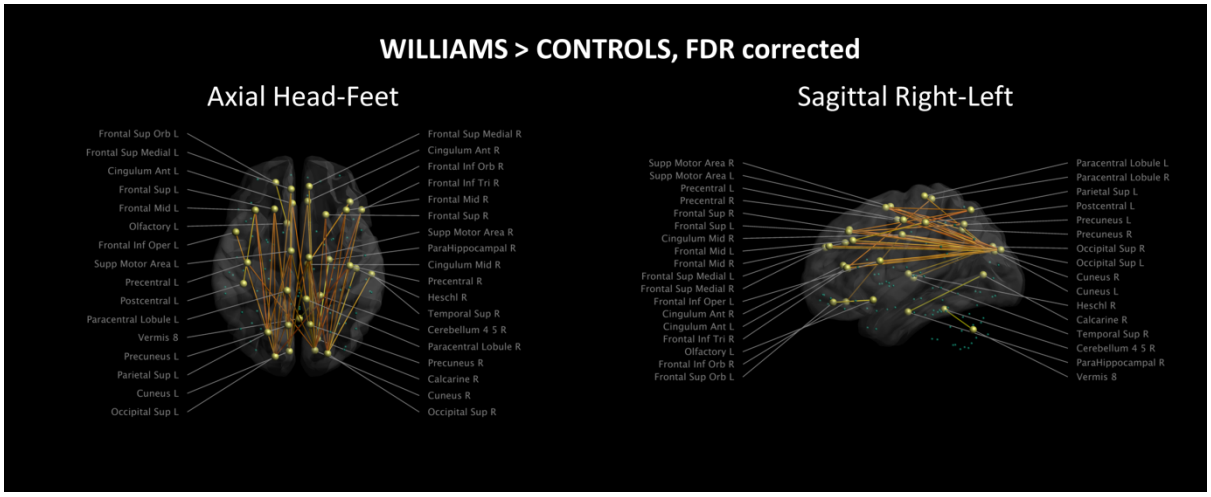

Figure 32 Results of the statistical analysis of WS connectome versus HC connectome. Small green spheres are edges without any significantly different connection between the two groups. Yellow spheres are edges which probability where significantly greater in WS than HC. Most of the altered connections were intra-hemispheric and in AP direction. The figure was created with ExploreDTI (http://www.exploredti.com).

Multi-parametric assessment of thigh muscles in patients with rare congenital myopathies: preliminary results.

Muscular dystrophies are a family of diseases that affect muscle cells leading to either muscle specific and system effects. Dystrophy subtypes have very different etiology, progress and severity on specific districts. Limb Girdle Muscular Dystrophies (LGMD) are characterized by progressive weakness that begins from the proximal limb muscles (Nigro, Aurino, & Piluso, 2011). One of the most common LGMD types is LGMD2A, due to high heterozygote frequency. It is caused by mutations of Calpain 3, a protein that has an important role in the M-lines functionality during sarcomere extension (Ojima et al., 2010). Mutations of the Dysferlin protein is the prominent cause of LGMD2B, the second most common type of LGMD. The protein is naturally involved in calcium-mediate sarcolemma resealing (Bansal et al., 2003), and mutations result in a number of effects that include higher inflammatory status than LGMD2A (Fischer et al., 2005). Beside hematic and genetic tests, MRI is the most used imaging tool to support the diagnosis of dystrophies (Díaz-Manera, Llauger, Gallardo, & Illa, 2015). Some studies characterized the degeneration pattern and the evolution of the diseases with T_{1W} or Short Tau Inversion Recovery (STIR) imaging, a sequence that enhances fat suppression and has good inflammation contrast (Mercuri et al., 2005; Pichiecchio et al., 2016; Polavarapu et al., 2016; Sarkozy et al., 2012; Stramare et al., 2010). Other studies characterized muscle tissue changes through Dixon imaging (Bonati,

Schmid, et al., 2015; Fischer et al., 2016; Fischmann et al., 2013; Leung, Carrino, Wagner, & Jacobs, 2015; Løkken, Hedermann, Thomsen, & Vissing, 2016; Willis et al., 2014) and T_2 quantification (Fischer et al., 2016; Janssen, Voet, Geurts, van Engelen, & Heerschap, 2016; R. J. Willcocks et al., 2014; Rebecca J Willcocks et al., 2016), while dMRI is less explored (Hooijmans et al., 2015; Ponrartana et al., 2015). This brief overview of the current literature well shows the usefulness of multiple MRI techniques in the investigation of muscular diseases.

On this basis, we performed a study of patients affected by LGMD2A and LGMD2B investigating the integration and complimentary of Dixon imaging, T_2 quantification and dMRI. Eleven healthy controls, 5 males and 6 females with age 45±10 years, 7 patients affected by LGMD2A, 2 males and 5 females with age 39±7 years, 7 patients affected by LGMD2B, 3 males and 4 females with age 48±7 years, were acquired with a 3T Philips Achieva scanner at IRCCS E. Medea (Bosisio Parini, LC, Italy). The acquisitions, performed with the 16 channels bed coil and the 16 channels torso coil, included a 12 echoes gradient-echo sequence Dixon (resolution 1x1x5mm^3, $T_E/\delta T_E/T_R$=2.7/1.2/16ms) for fat fraction (FF) quantification, a 15 echoes spin-echo sequence for T_2 quantification (resolution 1.7x1.7x5mm^3, $T_E/\delta T_E/T_R$=9.3/12.5/14300ms), and a multi-shell dMRI sequence (T_E/T_R=42/7000ms, resolution 1.5x1.5x6mm^3, 5 volumes at b=0s/mm^2, 16 directions at b=250,400s/mm^2). Clinical evaluations of muscular strength of quadriceps and adductors, according to the "Medical Research Council for muscular strength" (MRC), were available for each patient. T_2 quantification was performed voxel-wise with a mono-exponential model using in-house software written in MATLAB. dMRI data was pre-processed registering each volume to the first b=0s/mm^2 with Elastix to attenuate motion and eddy currents artifacts. DTI quantification was performed with Camino (Cook et al., 2006) using the RESTORE approach on the two-shells to minimize IVIM effects, as discussed in Chapter V. Involuntary patient motion and muscle contractions may alter the geometry of the muscles over different sequences, therefore affine transformations are generally not sufficient to achieve geometrical alignment of the data. However, non-linear transformations of volumes with different contrasts is generally difficult. We achieved optimal results using the affine/b-spline transformation shipped with Elastix to first compute the transformation from the Dixon to dMRI space, registering the Dixon Water Signal image to the first b=0s/mm^2 dMRI volume. Subsequently we used the same transformation to move the 6th echo of the T_2 sequence to the Dixon Fat Signal image, that was then concatenated with the previous to move both T_2 and

FF to the dMRI space. Regions of interest (ROIs) of the Posterior Muscles (PM), Anterior Muscles (AM), Gracilis muscle (GR) and Sartorius muscle (SR) were manually delineated on the Dixon of each subject, then median values of the metrics were computed for each ROI and subject, and used in subsequent analysis.

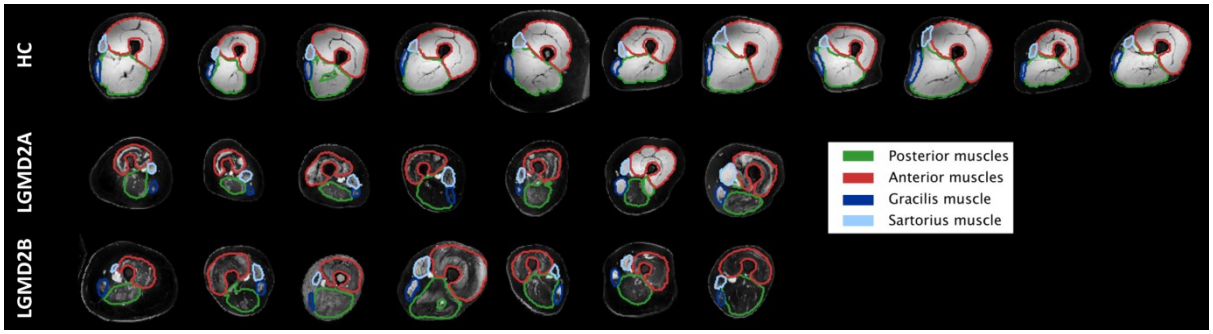

Figure 33 A middle axial slice of the Dixon water signal image of each subject. Images are overlaid with the manually delineated ROIs of all the subjects and represented in the dMRI space. Patients of both groups showed high fat infiltration and atrophy. ROIs were drawn following the native borders of the muscles, that were still visible in the water signal image.

Figure 33 shows an example of the Dixon water signal images of each subject, with the four ROIs overlaid. Patients of both groups were characterized by high fat infiltration and atrophy. Previous study evidenced that fat biases dMRI metrics in highly infiltrated patients, given its intrinsically lower SNR and the incompleteness of fat suppression (Froeling, Nederveen, Nicolay, & Strijkers, 2013; Hooijmans et al., 2015). Fat is also expected to affect T_2 quantification, given that its transversal relaxation time is much longer than that of muscles. The problem may be solved by discarding voxels with FF above a certain threshold, especially when dealing with low to mild fat infiltrated patients. However, within the ROIs of patients, the percentages of voxels with FF≤30% were between 2 and 36%. Instead of discarding voxels, we attempted to describe the bias induced by fat on the other metrics with multi-variate modeling. In particular, for each MRI metric, the following GLM was fit:

$$\mathrm{MRI}_{\mathrm{metric}} = \beta_0 + \beta_1 \mathrm{FF} + \beta_2 \mathrm{DIAGNOSIS}$$

where DIAGNOSIS was a categorical variable. The model was fit considering the median values of each ROI and subject altogether, then the metrics were individually corrected for fat effect but not for disease effect subtracting only the β_1FF term. The results of the process are shown in **Figure 34**. For all the parameters both FF and the diagnosis resulted to be

significant predictors. The adjusted R^2 of the GLM was 0.97 for T_2, 0.56 for MD and 0.68 for FA.

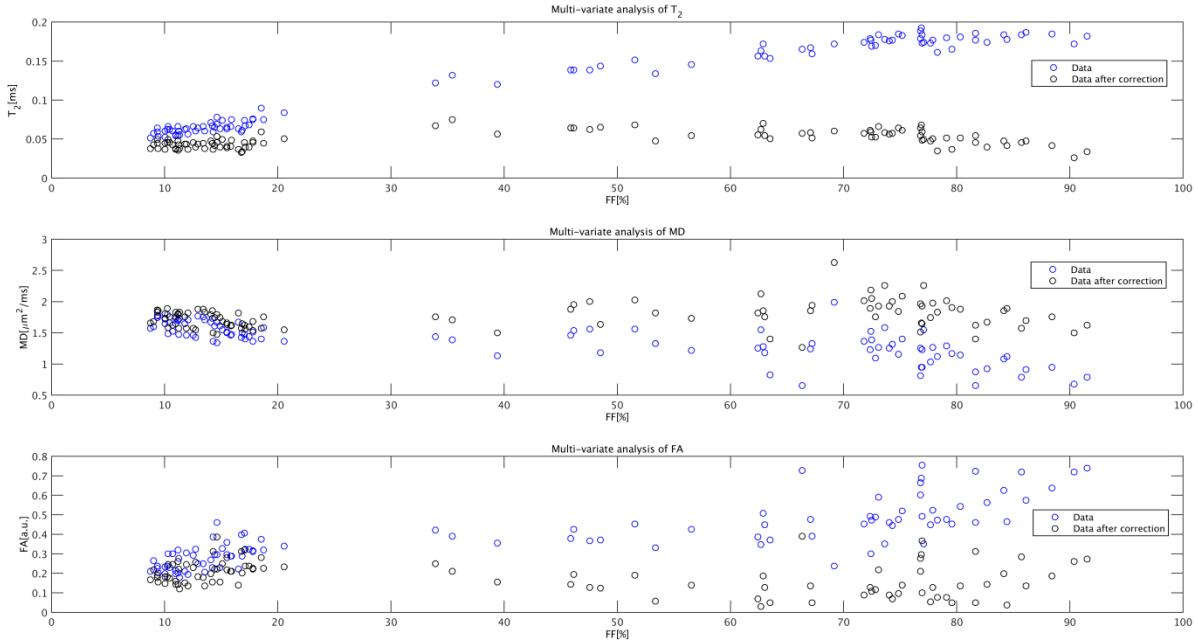

Figure 34 Regression plots of T_2, MD and FA versus FF. Blue points show the median values of each subject and ROI before correction, while the dotted red line is the multi-variate regression line. Black points represent the median points after correction. The regression model could explain a considerable part of the variance of MD and FA, and most of the T_2 variance, as exemplified by the adjusted R^2.

Average boxplots of the corrected metrics were computed for each group, then differences among muscles and groups were tested with the Wilcoxon Rank-Sum test and the Ansari-Bradley test for dispersion. Results are shown in **Figure 35**. Physiologic differences between muscle groups were observed in HC, with GR and SR showing higher T_2 and FA values, and lower MD than AM and PM. These differences were reduced in patients, eventually due to the massive architectural degeneration. Most of the differences between HC and patients were supported by FF. However, corrected measures also showed differences between patient groups and healthy controls. Finally, the correlations between MRI metrics and MRC of adductors and quadriceps were evaluated. Significant correlations were observed in the CAL group between FF of AM and MRC adductors (ρ=-0.89, p=0.01)/quadriceps (ρ=-76, p=0.05), pointing out a reduction of functionality with increasing FF, while FF was not significant in the DIS group. Conversely, MD and FA were correlated with MRC only in the DIS group, associating lower MD and higher FA values to higher functional scores. In particular, MD of the anterior muscles correlated with MRC of the quadriceps (ρ=-0.76, p=0.05) and MRC of

the adductor (ρ=-0.82, p=0.03), while FA of PM correlated with MRC of adductor (ρ=0.80, p=0.03). In conclusion, T_2 and dMRI metrics are strongly biased by fat in highly infiltrated patients, and the bias can be reduced by multi-variate modeling of the FF effect. FF explained MRC in LGMD2A but not in LGMD2B, where MRC correlated with corrected dMRI metrics.

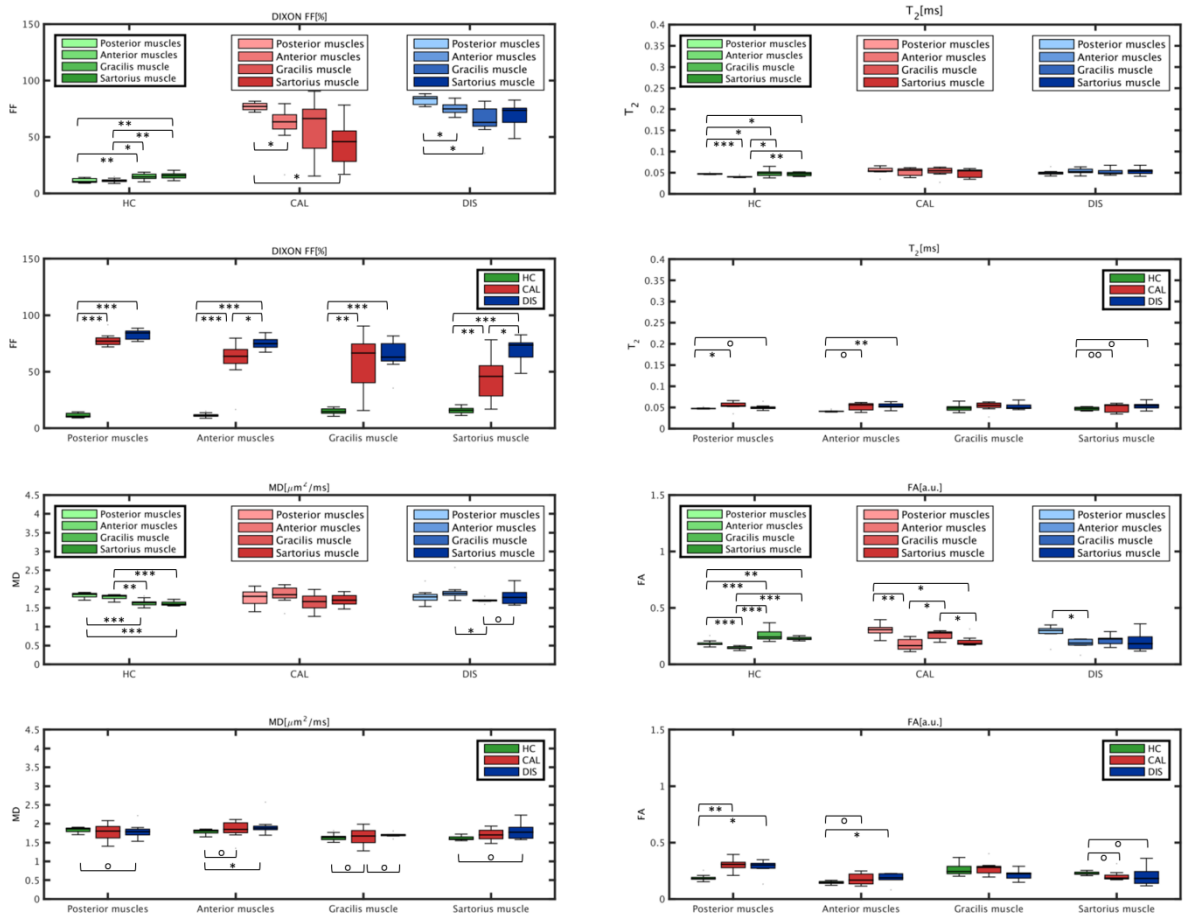

Figure 35 Boxplots of FF and corrected T_2, MD and FA grouped by diagnosis (odd rows) and muscles (even rows). Asterisks refer to statistical difference of medians (Wilcoxon Runk Sum test), while circles refer to statistical difference of dispersion (Ansari Bradley test). */°: p≤0.05; **/°°: p≤0.005; ***/°°°: p≤0.0005.

Early results of this study have been presented as conference proceedings at ISMRM 2015 (Alberto De Luca, D'Angelo, et al., 2016), and are now being submitted as a journal paper.

Automatic localization of cerebral cortical malformations using fractal analysis

Malformations of cortical development (MCDs) encompass a wide spectrum of brain abnormalities frequently associated with main neurological symptoms as epilepsy and cognitive impairment. The number and the complexity of the cortical gyri can be focally or diffusely reduced (pachygyria and lissencephaly), or increased (polymicrogyria), thus determining important alterations of the geometric pattern of the cortical layer (Barkovich, Guerrini, Kuzniecky, Jackson, & Dobyns, 2012). MRI and in particular T_{1W} images are the best non-invasive tool for the evaluation of the in-vivo cerebral cortex geometry. Existing quantitative analysis of T_{1W}, as Voxel Based Morphometry (VBM, (Ashburner & Friston, 2000)) or FreeSurfer (Fischl & Dale, 2000; Han et al., 2006), appear to be poorly suited for the analysis of MCDs. Being developed and tested mainly on healthy controls or patients with mild structural alterations, they may produce wrong results when applied to patients with large architectural deformations. Some previous works successfully employed these tools on some subtypes of MCDs (Im et al., 2012; Oliveira, Valente, Shergill, Leite, & Amaro, 2010). However, it is worth to notice that group level analyses require some degrees of inter-subject homogeneity and a sufficient sample size, but both conditions are not valid for MCDs: the variety and the complexity of the malformations are extremely wide and the sample size is critical, given the relatively low incidence of MCDs. In this work (A De Luca et al., 2016), we first introduce a novel voxel-wise approach based on fractal theory for the location of cortical abnormalities, then test its performances on MCDs subjects. In these pages only the most important findings will be reported, while fine details of the algorithms can be find in the published manuscript. The hypothesis underlying this study is that the brain cortex can be described with fractal geometry, as shown by a previous work (Kiselev, Hahn, & Auer, 2003) and that it can be fully characterized by its fractal dimension (FD, (Mandelbrot, 1982)). In a previous work (Squarcina et al., 2015) we introduced a bi-dimensional fractal based approach that revealed gray matter abnormalities in a group of psychiatric patients. A value of FD was computed for each axial slice with a modified 2D box-counting algorithm that included intensity information in the fractal calculus, then group level statistics were performed for each slice. Differently, the method here presented is designed to work on 3D volumes. 15 HC (9 males, 6 females, age 9.6±2.4 years) and 9 patients affected by MCDs (3 females, 6 females, age 7.8±2.3 years) underwent MRI at IRCCS Eugenio Medea (Bosisio Parini, Italy) with a Philips Achieva 3T scanner. For each

subject a 3D T_{1W} FFE sequence was acquired with T_E/T_R=3.86/8.40ms, voxel resolution 1x1x1mm^3. Five patients showed bilateral and diffuse polymicrogyria on 2 or more cerebral lobes, one patient showed unilateral polymicrogyria in the opercular and parietal region of the right hemisphere, one patient showed both bilateral polymicrogyria and a simplified gyral pattern, while two subjects reported pachygyria and subcortical band heterotopia.

Fractal objects are characterized by self-similarity, that is the repetition of a motif at different observation scales. A common algorithm used to compute the FD of fractal objects is the box-counting algorithm, introduced by Mandelbrot in 1982 (Mandelbrot, 1982). However, this algorithm only provides a global FD value, thus it is unsuitable for the localization of abnormalities. We extended the box-counting algorithm to 1) use an arbitrary voxel-wise weight in the box-counting and 2) to obtain voxel-wise values of FD using the neighborhood of each voxel V. Along with FD, we additionally computed Q, that is the intercept of the linear regression of the box-counting algorithm and represents the logarithm of the number of occupied voxels. It can thus be considered as a surrogate measure of density in around V.

T_{1W} volumes were firstly pre-processed to perform intensity bias correction with the N4 tool of ANTs (Tustison et al., 2010), then the standard FSL processing pipeline was applied. The pipeline included skull-stripping with the Brain Extraction Tool (BET, (S. M. Smith, 2002)), linear and non-linear registration to a standard template with the FMRIB's Linear/Non-linear Registration Tools (FLIRT/FNIRT, (Mark Jenkinson, Bannister, Brady, & Smith, 2002; Mark Jenkinson, Beckmann, Behrens, Woolrich, & Smith, 2012; M Jenkinson & Smith, 2001)), tissue type segmentation with the FMRIB's automated segmentation tool (FAST) (Y Zhang et al., 2001) and sub-cortical classification with FIRST (Patenaude, Smith, Kennedy, & Jenkinson, 2011). Given our interest only in cortical GM, a gray matter mask was built using the GM PVE map and excluding the cerebellum and brain stem using the sub-cortical tissue segmentation (Mazziotta et al., 2001). Two different GM templates were built with ANTs using the GM PVE maps of two distinct subsets of 5 HC. FD and Q maps were computed in the subject space to avoid artefactual shape alterations using the GM PVE as weight, then moved to template space for inter-subject comparisons. All the mentioned pre-processing steps are visually summarized in **Figure 36**.

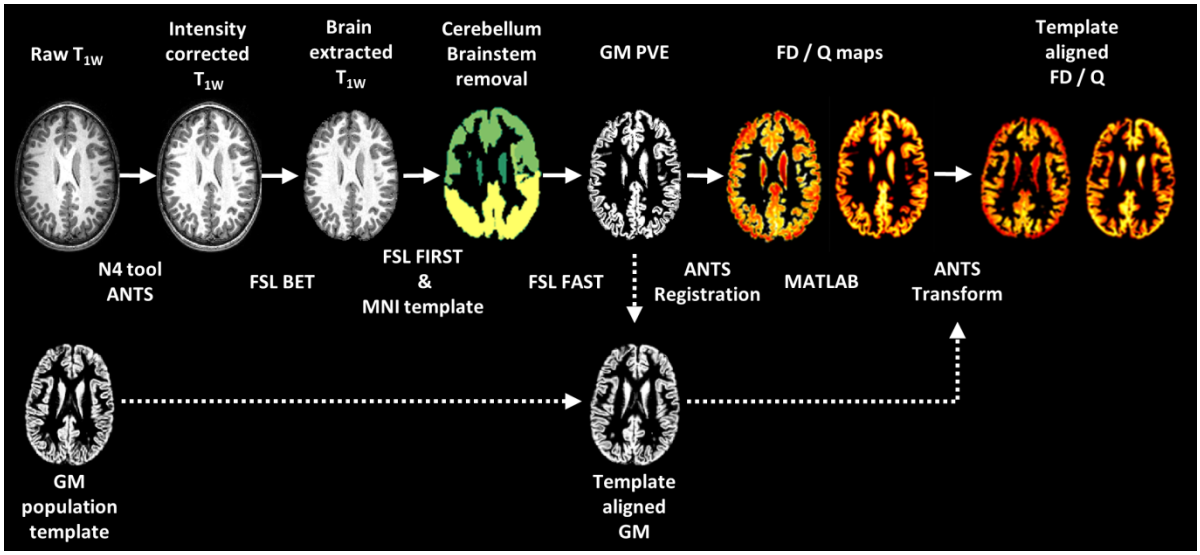

Figure 36 A graphical overview of the steps and the tools involved in the processing pipeline.

A global and a local distance maps were defined to perform the lesion segmentation with both diffuse and focal features. The FD and Q normalized histograms were computed for each subject, obtaining individual probabilities of FD and Q. The histograms of HC were averaged to obtain a reference histogram, then the global probability maps were computed by assigning to each voxel V of a given subject S the order 1 distance of the FD/Q histogram computed in S from the reference histogram. Local distance maps were defined similarly, but histograms were computed in the neighborhood of each voxel V. Lesion detection was finally performed by thresholding the distance maps with two different thresholds, that were optimized to achieve a false positive rate (FPR) less than 5% or to maximize the (weighted) accuracy of the algorithm. The maximum achieved accuracy was 84%, corresponding to 85% specificity and 83% sensitivity, and resulted in the lesion detection maps shown in **Figure 37**. The area under the ROC curve (Bradley, 1997) of the algorithm was 0.88. The whole procedure was repeated on the second anatomical template and resulted in very similar performances. To compare our method with previously published approaches, the FreeSurfer reconstruction was performed on the same dataset. Three different metrics previously used for lesion detection in conjunction with z-scores thresholding were analyzed: cortical thickness, sulcal depth and curvature index. Our method outperformed all three metrics, that resulted in with (weighted) accuracy between 0.61 and 0.75, with areas under the ROC curve between 0.64 and 0.8.

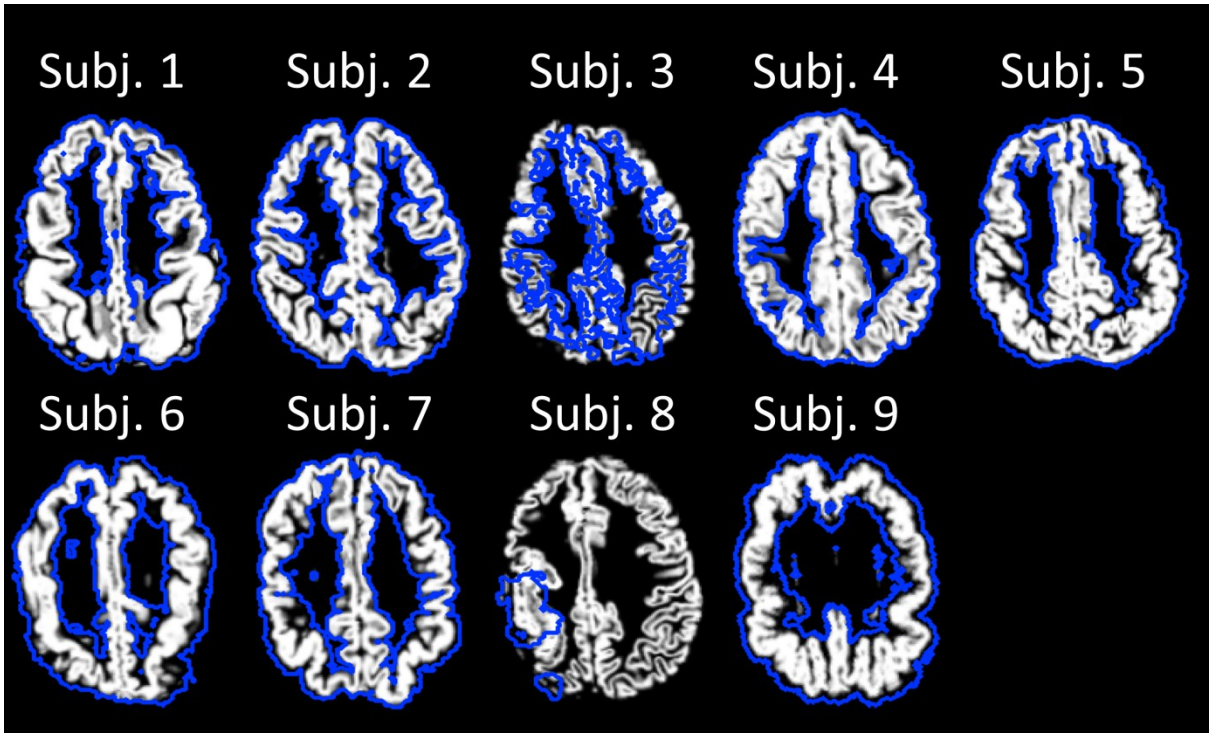

Figure 37 Axial slice of the GM segmentation of MCD subjects. All subjects were aligned to TMP1 with an affine 12 DOF transform for visual comparison. Contoured areas show the final lesion map (solid blue lines). Subject 8 is particularly interesting as affected by focal pathology. Notice that the algorithm selected only the abnormal side.

In conclusion, we proved that fractal indices are able to characterize the alterations induced by MCDs. The reliance on voxel-based box-counting and on local distance maps allowed the correct identification of focal MCDs, even when the size of the lesions was limited. On the tested dataset the method was characterized by high accuracy and it was possible to tune its parameters to enforce sensitivity or specificity. This method is feasible for clinical applications and can easily be applied on large datasets.

Neurogenetics of developmental dyslexia: from genes to behavior through brain neuroimaging and cognitive and sensorial mechanisms

Reading is a cognitive skill unique to humans, however, for about 5 to 12% of the population it is extremely difficult (Peterson & Pennington, 2015). These individuals are affected by a complex neurodevelopmental disorder called developmental dyslexia (DD), which represents the most common learning disability among school-aged children. Genetics are rapidly gaining popularity in DD and much has been learned regarding the possible downstream

effects of DD risk genes on brain structure, function and circuitry. Following the increasing findings provided by molecular genetic, cognitive, and imaging-genetic studies of DD, in a work that is now in press (Mascheretti et al., n.d.), we propose an inter-disciplinary, multi-level, imaging-genetic approach to disentangle the pathways from genes to behavior. Since the early 1980s, at least nine DD risk loci have been mapped on 8 different chromosomes and named DYX1-DYX9 (Carrion-Castillo, Franke, & Fisher, 2013; Eicher & Gruen, 2013; Scerri & Schulte-Körne, 2010; Skeide et al., 2016; Yuping Zhang et al., 2016; Zhao, Chen, Zhang, & Zuo, 2016). Several genes spanning these regions have been reported and linked to DD etiology. Among all these genes, 9 DD-candidates have been replicated in at least one independent sample: DYX1C1, DCDC2, KIAA0319, C2ORF3, MRPL19, ROBO1, GRIN2B, FOXP2 and CNTNAP2 (Einarsdottir et al., 2015; Graham & Fisher, 2013; Ludwig et al., 2010). Recently, a short tandem repeat (BV677278) has been reported in the intron 2 of the DCDC2 gene (Meng et al., 2011; Yuping Zhang et al., 2016). It has been observed to be rather conserved across species and appears to change the gene expression. Accordingly, the name READ1 (Regulatory Element Associated with Dyslexia 1) has been proposed for this genetic risk variant (Powers et al., 2013). A naturally occurring deletion encompassing READ1 (DCDC2d) has been associated with DD and DD-related phenotypes (Brkanac et al., 2007). Findings on DCDC2, DYX1C1, ROBO1, KIAA0319, FOXP2 and CNTNAP2 (Cicchini, Marino, Mascheretti, Perani, & Morrone, 2015; Gori, Seitz, Ronconi, Franceschini, & Facoetti, 2015; Lai, Gerrelli, Monaco, Fisher, & Copp, 2003; Strauss et al., 2006; Truong et al., 2014; Vernes et al., 2008; Y. Wang et al., 2006) depict DD as a disorder at the mild end of the spectrum of a number of pathways producing developmental disturbances in neuronal positioning and axonal outgrowth.

MRI has been extensively used to investigated both morphological, structural and functional abnormalities in DD patients. Most of the MRI studies have relied on Voxel Based Morphometry (VBM) to quantify gray (Kronbichler et al., 2008; Pernet, Poline, Demonet, & Rousselet, 2009; Vinckenbosch, Robichon, & Eliez, 2005) and white matter (Dole, Meunier, & Hoen, 2013; Silani et al., 2005) volumes and fMRI during specific tasks (Baillieux et al., 2009; Paulesu, Danelli, & Berlingeri, 2014; Seki et al., 2001; Shaywitz et al., 2002). Finally, dMRI (Carter et al., 2009; Rimrodt, Peterson, Denckla, Kaufmann, & Cutting, 2010; Steinbrink et al., 2008) has been used to perform voxel-wise statistics, in conjunction with Tract-Based Spatial Statistics (TBSS) (S. M. Smith et al., 2006) or for fiber-tracking purposes. A summary of the findings can be seen in **Figure 38**, while more detailed results,

including lists of anatomical areas, will be available in the published paper. Given the heterogeneity of imaging modalities and findings, it is difficult to summarize results into a unifying perspective. VBM and DTI seem to converge into temporo-parietal and partially middle-frontal involvement in DD, while anterior and occipital areas seem to be less frequently involved. Regarding fMRI, results may be aggregated observing general prevalence of cerebral hypo-activation over hyper-activation during task-based fMRI. Circuits involving temporo-basal, parietal and frontal lobes are more frequently impaired, without a clear lateralization between left and right hemispheres.

We believe that the heterogeneity and variability observed in imaging studies results, suggests the need of a refined approach. Imaging data may be considered as an intermediate phenotype (IP) (Gottesman & Gould, 2003), i.e. a reduced measure of functioning. Genetic determination of IPs is likely to be less complex than the determination of the related behavioral / clinical phenotype, as the latter incorporates multiple neural systems and is influenced by multiple genes and environmental etiologic variables (Pennington, 2006). To note, such use of IPs has played a crucial role in improving the knowledge of the gene to phenotype gap in other neurodevelopmental disorders (Braff, 2015).

Performing joint genetic and neuroimaging studies in humans, where the association between genotypes and brain phenotypes can be tested, is an emerging strategy to link DD-candidate genes to brain structure and function. To date, imaging-genetic studies have focused on at least one of the above described DD-candidate genes and on the proposed functional variants spanning them (Darki, Peyrard-Janvid, Matsson, Kere, & Klingberg, 2012, 2014; Dennis et al., 2011; Eicher & Gruen, 2013; Hoogman et al., 2014; Jamadar et al., 2013; Marino et al., 2014; Meda et al., 2008; Pergola et al., 2016; Pinel et al., 2012; Scerri et al., 2012; Scott-Van Zeeland et al., 2010; Tan, Doke, Ashburner, Wood, & Frackowiak, 2010; von Hohenberg et al., 2014; Whalley et al., 2011; Wilcke et al., 2012). These works are taken into consideration to support the proposal of an interdisciplinary approach by focusing on selective, functional genetic variants and particular, well-defined cognitive/sensorial phenotypes. DCDC2d has been associated with altered GM volumes in reading/language-related brain regions especially in the left hemisphere (Meda et al., 2008), and with common and unique alterations of WM fiber tracts in subjects with DD (Marino et al., 2014).

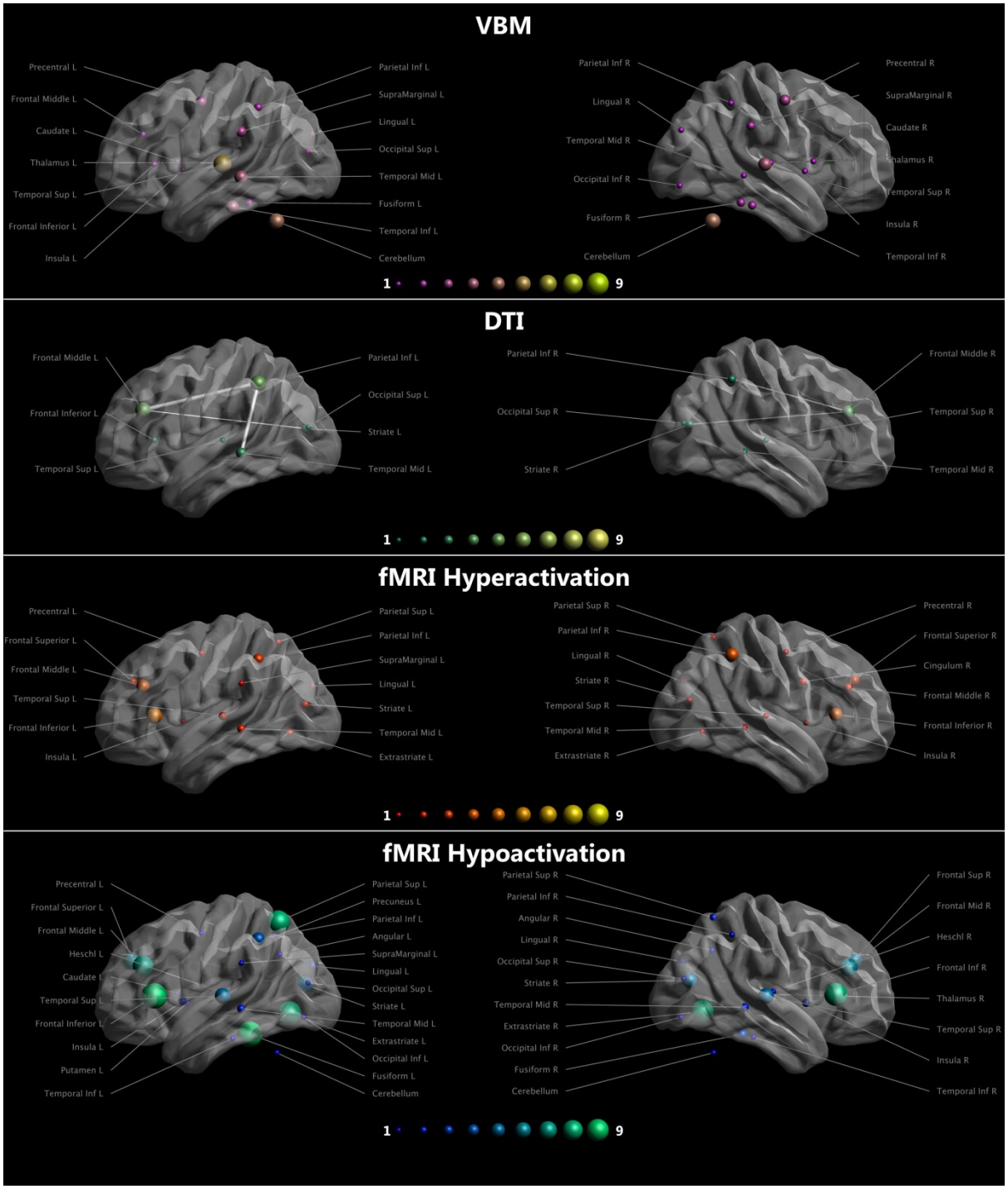

Figure 38 Rows show the findings obtained with structural and functional MRI techniques in DD subjects. The size and the color of the spheres reflect the amount of papers reporting differences in the specified area. Longitudinal fascicoli and arcuate fasciculus are shown as edges. fMRI findings are not divided by task. Task specific findings are available in Supplementary material of the published paper. The figure was created with ExploreDTI (http://www.exploredti.com).

Clearly, neuroimaging is playing a fundamental part in disentangling the role of genetic variants in the etiology of complex cognitive functions as reading. However, the complexity of the "reading circuit" is still far from being fully understood, as revealed by the heterogeneous and sometimes conflicting results of brain MRI studies. Study design and data processing are important factors increasing complexity and heterogeneity in neuroimaging research. The inclusion of subjects with unknown genetic profile is likely to enhance inter-subject variability, as different DD genes may cause different deficits. Even if some imaging-genetic studies of DD have been proposed, the number of these work is too low to draw definitive conclusions about the role of each DD-candidate gene. Moreover, it is interesting to note some technical evidence that might limit the integration of these results. Of the imaging-genetic studies mentioned in this review, ten have employed 1.5T scanners, eight were performed with 3T scanners, one acquired with a 4T scanner. Two of them employed similar acquisition protocols and performed VBM to investigate GM, but their results were only partially overlapping. These different findings may be due to the different disorders included in the studies, and/or to the different analysis pipelines (linear regression versus independent component analysis). Genetic data can be integrated with every parametric map derived from MRI, whether a simple measure of volume, a microstructure related metric or a measure of chemical properties. Three of the mentioned studies integrated genetic data in the VBM analysis of WM volume as attempt to reveal genetically-related alterations, limiting the analysis of DTI data to the detection of the major fiber bundles included in altered WM areas. Nevertheless, DTI analysis can provide metrics that are more specific to WM microstructure than VBM. These maps can be analyzed similarly to VBM, but may provide additional characterization of the genetic effect at microstructure level. To date, only three studies have used DTI-derived maps to detect voxel-based WM modifications related to DD-candidate genes. Further studies with cutting the edge diffusion MRI protocols (i.e. high field magnets, multiple directions and b-values) and populations with a specific genetic characterization are therefore needed. Moreover, recent diffusion-based techniques, as the Neurite Orientation Dispersion and Density Imaging have provided metrics that are more specific to WM and GM in several applications. The application of such model or other affine techniques might be beneficial to the study of DD, providing additional disentanglement of the connections between genetic variations and structural alterations.

In conclusion, this review aimed to highlight the promising imaging-genetic approach as a way to unravel insights behind the pathophysiology of reading (dis)ability. As the presence of

putative functional genetic variants influencing the expression of some of the DD-candidate genes has been provided and as genetic associations with specific, well-defined cognitive / sensorial mechanisms have been reported, current knowledge of genetics of DD could help target imaging more selectively. Even if there are weaknesses despite strengths in this perspective, such hypothesis driven approach in imaging-genetic as a field would lead to the optimization of criteria to diagnose DD and to the early identification of 'biologically at-risk' children.

FIGURES CREDITS

Figure 1 was downloaded from: chem.libretexts.org under the Creative Commons Attribution-Noncommercial-Share Alike 3.0 United States License.

Figure 2 was adapted from: The Principles of Magnetic Resonance, and Associated Hardware, in *Magnetic Resonance Technology: Hardware and System Component Design*, 2016, pp. 1-47 DOI: 10.1039/9781782623878-00001 eISBN:978-1-78262-387-8.

Figure 3 is property of Treccani (treccani.it), that allowed the inclusion of the figure within this thesis with written consent received on the 14th of November 2016. The picture was downloaded from http://www.treccani.it/enc/media/share/images/orig/system/galleries/Enciclopedia_della_Scienza_e_della_Tecnica/Integrazioni/Vol.4/Rison_magn_nucl_fig_03.jpg.

Figure 9 was downloaded from the English Wikipedia [Public domain], via Wikimedia Commons https://upload.wikimedia.org/wikipedia/commons/3/3c/Ms_progression_types.svg

Figure 10 was taken from: "Epilepsy in multiple sclerosis: The role of temporal lobe damage", published June 2016 in Multiple Sclerosis Journal, doi: 10.1177/1352458516651502.

Figure 12 was taken from: "DTI visualization with streamsurfaces and evenly-spaced volume seeding", VisSym '04 Joint Eurographics – IEEE TCVG Symposium on Visualization, Conference Proceedings

REFERENCES

Alexander, D. C., Hubbard, P. L., Hall, M. G., Moore, E. a, Ptito, M., Parker, G. J. M., & Dyrby, T. B. (2010). Orientationally invariant indices of axon diameter and density from diffusion MRI. *NeuroImage*, *52*(4), 1374–89. https://doi.org/10.1016/j.neuroimage.2010.05.043

Andersson, J. L. R., Skare, S., & Ashburner, J. (2003). How to correct susceptibility distortions in spin-echo echo-planar images: application to diffusion tensor imaging. *NeuroImage*, *20*(2), 870–88. https://doi.org/10.1016/S1053-8119(03)00336-7

Andersson, J. L. R., & Sotiropoulos, S. N. (2016). An integrated approach to correction for off-resonance effects and subject movement in diffusion MR imaging. *NeuroImage*, *125*, 1063–78. https://doi.org/10.1016/j.neuroimage.2015.10.019

Ashburner, J., & Friston, K. J. (2000). Voxel-based morphometry--the methods. *NeuroImage*, *11*(6 Pt 1), 805–21. https://doi.org/10.1006/nimg.2000.0582

Assaf, Y., & Basser, P. J. (2005). Composite hindered and restricted model of diffusion (CHARMED) MR imaging of the human brain. *NeuroImage*, *27*(1), 48–58. https://doi.org/10.1016/j.neuroimage.2005.03.042

Assaf, Y., Blumenfeld-Katzir, T., Yovel, Y., & Basser, P. J. (2008). AxCaliber: a method for measuring axon diameter distribution from diffusion MRI. *Magnetic Resonance in Medicine : Official Journal of the Society of Magnetic Resonance in Medicine / Society of Magnetic Resonance in Medicine*, *59*(6), 1347–54. https://doi.org/10.1002/mrm.21577

Aung, W. Y., Mar, S., & Benzinger, T. L. (2013). Diffusion tensor MRI as a biomarker in axonal and myelin damage. *Imaging in Medicine*, *5*(5), 427–440. https://doi.org/10.2217/iim.13.49

Avants, B. B., Tustison, N. J., Song, G., Cook, P. A., Klein, A., & Gee, J. C. (2011). A reproducible evaluation of ANTs similarity metric performance in brain image registration. *NeuroImage*, *54*(3), 2033–44. https://doi.org/10.1016/j.neuroimage.2010.09.025

Baillieux, H., Vandervliet, E. J. M., Manto, M., Parizel, P. M., De Deyn, P. P., & Mariën, P.

(2009). Developmental dyslexia and widespread activation across the cerebellar hemispheres. *Brain and Language*, *108*(2), 122–32. https://doi.org/10.1016/j.bandl.2008.10.001

Bane, O., Wagner, M., Zhang, J. L., Dyvorne, H. A., Orton, M., Rusinek, H., & Taouli, B. (2016). Assessment of renal function using intravoxel incoherent motion diffusion-weighted imaging and dynamic contrast-enhanced MRI. *Journal of Magnetic Resonance Imaging : JMRI*. https://doi.org/10.1002/jmri.25171

Bansal, D., Miyake, K., Vogel, S. S., Groh, S., Chen, C.-C., Williamson, R., … Campbell, K. P. (2003). Defective membrane repair in dysferlin-deficient muscular dystrophy. *Nature*, *423*(6936), 168–72. https://doi.org/10.1038/nature01573

Barkovich, A. J., Guerrini, R., Kuzniecky, R. I., Jackson, G. D., & Dobyns, W. B. (2012). A developmental and genetic classification for malformations of cortical development: Update 2012. *Brain*. https://doi.org/10.1093/brain/aws019

Basser, P. J., Mattiello, J., & LeBihan, D. (1994). MR diffusion tensor spectroscopy and imaging. *Biophysical Journal*, *66*(1), 259–67. https://doi.org/10.1016/S0006-3495(94)80775-1

Basser, P. J., & Pierpaoli, C. (1996). Microstructural and physiological features of tissues elucidated by quantitative-diffusion-tensor MRI. *Journal of Magnetic Resonance. Series B*, *111*, 209–219. https://doi.org/10.1016/j.jmr.2011.09.022

Behrens, T. E. J., Woolrich, M. W., Jenkinson, M., Johansen-Berg, H., Nunes, R. G., Clare, S., … Smith, S. M. (2003). Characterization and propagation of uncertainty in diffusion-weighted MR imaging. *Magnetic Resonance in Medicine*, *50*(5), 1077–88. https://doi.org/10.1002/mrm.10609

Bland, J. M., & Altman, D. G. (1986). Statistical methods for assessing agreement between two methods of clinical measurement. *Lancet (London, England)*, *1*(8476), 307–10. Retrieved from http://www.ncbi.nlm.nih.gov/pubmed/2868172

Bloch, F., Hansen, W. W., & Packard, M. (1946a). Nuclear Induction. *Physical Review E*, *69*(127). https://doi.org/https://doi.org/10.1103/PhysRev.69.127

Bloch, F., Hansen, W. W., & Packard, M. (1946b). The Nuclear Induction Experiment.

Physical Review E, *70*(474). https://doi.org/https://doi.org/10.1103/PhysRev.70.474

Bonati, U., Hafner, P., Schädelin, S., Schmid, M., Naduvilekoot Devasia, A., Schroeder, J., … Fischer, D. (2015). Quantitative muscle MRI: A powerful surrogate outcome measure in Duchenne muscular dystrophy. *Neuromuscular Disorders*. https://doi.org/10.1016/j.nmd.2015.05.006

Bonati, U., Schmid, M., Hafner, P., Haas, T., Bieri, O., Gloor, M., … Fischer, D. (2015). Longitudinal 2-point dixon muscle magnetic resonance imaging in becker muscular dystrophy. *Muscle & Nerve*, *51*(6), 918–21. https://doi.org/10.1002/mus.24629

Bradley, A. P. (1997). The use of the area under the ROC curve in the evaluation of machine learning algorithms. *Pattern Recognition*, *30*(7), 1145–1159. https://doi.org/10.1016/S0031-3203(96)00142-2

Braff, D. L. (2015). The importance of endophenotypes in schizophrenia research. *Schizophrenia Research*, *163*(1–3), 1–8. https://doi.org/10.1016/j.schres.2015.02.007

Brkanac, Z., Chapman, N. H., Matsushita, M. M., Chun, L., Nielsen, K., Cochrane, E., … Raskind, W. H. (2007). Evaluation of candidate genes for DYX1 and DYX2 in families with dyslexia. *American Journal of Medical Genetics. Part B, Neuropsychiatric Genetics : The Official Publication of the International Society of Psychiatric Genetics*, *144B*(4), 556–60. https://doi.org/10.1002/ajmg.b.30471

Brown, R. W., Cheng, Y.-C. N., Haacke, E. M., Thompson, M. R., & Venkatesan, R. (2014). *Magnetic Resonance Imaging*. (R. W. Brown, Y.-C. N. Cheng, E. M. Haacke, M. R. Thompson, & R. Venkatesan, Eds.). Chichester, UK: John Wiley & Sons Ltd. https://doi.org/10.1002/9781118633953

Calabrese, M., Castellaro, M., Bertoldo, A., De Luca, A., Pizzini, F. B., Ricciardi, G. K., … Monaco, S. (2016). Epilepsy in multiple sclerosis: The role of temporal lobe damage. *Multiple Sclerosis (Houndmills, Basingstoke, England)*. https://doi.org/10.1177/1352458516651502

Calabrese, M., De Stefano, N., Atzori, M., Bernardi, V., Mattisi, I., Barachino, L., … Gallo, P. (2008). Extensive cortical inflammation is associated with epilepsy in multiple sclerosis. *Journal of Neurology*, *255*(4), 581–6. https://doi.org/10.1007/s00415-008-0752-7

Calabrese, M., Filippi, M., & Gallo, P. (2010). Cortical lesions in multiple sclerosis. *Nature Reviews. Neurology*, *6*(8), 438–44. https://doi.org/10.1038/nrneurol.2010.93

Calabrese, M., Rinaldi, F., Grossi, P., Mattisi, I., Bernardi, V., Favaretto, A., … Gallo, P. (2010). Basal ganglia and frontal/parietal cortical atrophy is associated with fatigue in relapsing-remitting multiple sclerosis. *Multiple Sclerosis (Houndmills, Basingstoke, England)*, *16*(10), 1220–8. https://doi.org/10.1177/1352458510376405

Calabrese, M., Rocca, M. A., Atzori, M., Mattisi, I., Favaretto, A., Perini, P., … Filippi, M. (2010). A 3-year magnetic resonance imaging study of cortical lesions in relapse-onset multiple sclerosis. *Annals of Neurology*, *67*(3), 376–83. https://doi.org/10.1002/ana.21906

Campuzano, V., Montermini, L., Lutz, Y., Cova, L., Hindelang, C., Jiralerspong, S., … Koenig, M. (1997). Frataxin is reduced in Friedreich ataxia patients and is associated with mitochondrial membranes. *Human Molecular Genetics*, *6*(11), 1771–80. Retrieved from http://www.ncbi.nlm.nih.gov/pubmed/9302253

Campuzano, V., Montermini, L., Moltò, M. D., Pianese, L., Cossée, M., Cavalcanti, F., … Pandolfo, M. (1996). Friedreich's ataxia: autosomal recessive disease caused by an intronic GAA triplet repeat expansion. *Science (New York, N.Y.)*, *271*(5254), 1423–7. Retrieved from http://www.ncbi.nlm.nih.gov/pubmed/8596916

Carr, H. Y., & Purcell, E. M. (1954). Effects of Diffusion on Free Precession in Nuclear Magnetic Resonance Experiments. *Physical Review E*, *94*(630). https://doi.org/https://doi.org/10.1103/PhysRev.94.630

Carrion-Castillo, A., Franke, B., & Fisher, S. E. (2013). Molecular genetics of dyslexia: an overview. *Dyslexia (Chichester, England)*, *19*(4), 214–40. https://doi.org/10.1002/dys.1464

Carter, J. C., Lanham, D. C., Cutting, L. E., Clements-Stephens, A. M., Chen, X., Hadzipasic, M., … Kaufmann, W. E. (2009). A dual DTI approach to analyzing white matter in children with dyslexia. *Psychiatry Research*, *172*(3), 215–9. https://doi.org/10.1016/j.pscychresns.2008.09.005

Casaseca-de-la-Higuera, P., Tristán-Vega, A., Aja-Fernández, S., Alberola-López, C., Westin, C.-F., & San José Estépar, R. (2012). Optimal real-time estimation in diffusion

tensor imaging. *Magnetic Resonance Imaging*, *30*(4), 506–17. https://doi.org/10.1016/j.mri.2011.12.001

Chang, L.-C., Jones, D. K., & Pierpaoli, C. (2005). RESTORE: robust estimation of tensors by outlier rejection. *Magnetic Resonance in Medicine : Official Journal of the Society of Magnetic Resonance in Medicine / Society of Magnetic Resonance in Medicine*, *53*(5), 1088–95. https://doi.org/10.1002/mrm.20426

Cheung, M. M., Hui, E. S., Chan, K. C., Helpern, J. A., Qi, L., & Wu, E. X. (2009). Does diffusion kurtosis imaging lead to better neural tissue characterization? A rodent brain maturation study. *NeuroImage*, *45*(2), 386–92. https://doi.org/10.1016/j.neuroimage.2008.12.018

Cho, G. Y., Moy, L., Zhang, J. L., Baete, S., Lattanzi, R., Moccaldi, M., … Sigmund, E. E. (2015). Comparison of fitting methods and b-value sampling strategies for intravoxel incoherent motion in breast cancer. *Magnetic Resonance in Medicine*, *74*(4), 1077–85. https://doi.org/10.1002/mrm.25484

Cicchini, G. M., Marino, C., Mascheretti, S., Perani, D., & Morrone, M. C. (2015). Strong motion deficits in dyslexia associated with DCDC2 gene alteration. *The Journal of Neuroscience : The Official Journal of the Society for Neuroscience*, *35*(21), 8059–64. https://doi.org/10.1523/JNEUROSCI.5077-14.2015

Compston, A., & Coles, A. (2008). Multiple sclerosis. *Lancet (London, England)*, *372*(9648), 1502–17. https://doi.org/10.1016/S0140-6736(08)61620-7

Concia, M., Sprinkart, A. M., Penner, A.-H., Brossart, P., Gieseke, J., Schild, H. H., … Mürtz, P. (2014). Diffusion-weighted magnetic resonance imaging of the pancreas: diagnostic benefit from an intravoxel incoherent motion model-based 3 b-value analysis. *Investigative Radiology*, *49*(2), 93–100. https://doi.org/10.1097/RLI.0b013e3182a71cc3

Cook, P. A., Bai, Y., Nedjati-Gilani, S., Seunarine, K. K., Hall, M. G., Parker, Geoff J M, & Alexander, D. C. (2006). Camino: Open-Source Diffusion-MRI Reconstruction and Processing. In *International Society for Magnetic Resonance in Medicine*. Seattle, USA.

Darki, F., Peyrard-Janvid, M., Matsson, H., Kere, J., & Klingberg, T. (2012). Three dyslexia susceptibility genes, DYX1C1, DCDC2, and KIAA0319, affect temporo-parietal white matter structure. *Biological Psychiatry*, *72*(8), 671–6.

https://doi.org/10.1016/j.biopsych.2012.05.008

Darki, F., Peyrard-Janvid, M., Matsson, H., Kere, J., & Klingberg, T. (2014). DCDC2 polymorphism is associated with left temporoparietal gray and white matter structures during development. *The Journal of Neuroscience : The Official Journal of the Society for Neuroscience*, *34*(43), 14455–62. https://doi.org/10.1523/JNEUROSCI.1216-14.2014

Das, S. R., Avants, B. B., Grossman, M., & Gee, J. C. (2009). Registration based cortical thickness measurement. *NeuroImage*, *45*(3), 867–79. https://doi.org/10.1016/j.neuroimage.2008.12.016

De Luca, A., Arrigoni, F., Romaniello, R., Triulzi, F. M., Peruzzo, D., & Bertoldo, A. (2016). Automatic localization of cerebral cortical malformations using fractal analysis. *Physics in Medicine and Biology*, *61*(16), 6025–40. https://doi.org/10.1088/0031-9155/61/16/6025

De Luca, A., Bertoldo, A., Arrigoni, F., & Froeling, M. (2016). Hindered diffusion, free water and pseudo-diffusion quantification in the brain: a comparison of Stejskal-Tanner and Flow-Compensated gradients. In *Diffusion Workshop of the International Society for Magnetic Resonance in Medicine*. Lisbon, Portugal.

De Luca, A., Bertoldo, A., & Froeling, M. (2016). Effects of perfusion on DTI and DKI estimates in the skeletal muscle. *Magnetic Resonance in Medicine*. https://doi.org/10.1002/mrm.26373

De Luca, A., Castellaro, M., Montemezzi, S., Calabrese, M., & Bertoldo, A. (2015a). Hippocampi and epilepsy in MS patients: a diffusion weighted imaging study with NODDI. In *International Society for Magnetic Resonance in Medicine* (p. 29 May-06 June 2015). Toronto, Canada.

De Luca, A., Castellaro, M., Montemezzi, S., Calabrese, M., & Bertoldo, A. (2015b). Tissue separation of multi-shell DW-MRI with a physiologically constrained multi compartment model and spherical deconvolution. In *International Society for Magnetic Resonance in Medicine* (p. 29 May-06 June 2015). Toronto, Canada.

De Luca, A., D'Angelo, M. G., Peruzzo, D., Triulzi, F., Bertoldo, A., & Arrigoni, F. (2016). Multi-parametric assessment of thigh muscles in patients with limb girdle muscular

dystrophies (LGMD): preliminary results. In *International Society for Magnetic Resonance in Medicine*. Singapore.

Delatycki, M. B., Williamson, R., & Forrest, S. M. (2000). Friedreich ataxia: an overview. *Journal of Medical Genetics*, *37*(1), 1–8. Retrieved from http://www.ncbi.nlm.nih.gov/pubmed/10633128

Dell'acqua, F., Rizzo, G., Scifo, P., Clarke, R., Scotti, G., Cerutti, S., & Fazio, F. (2005). A Deconvolution Approach Based on Multi-Tensor Model to Solve Fiber Crossing in Diffusion-MRI. *Conference Proceedings : ... Annual International Conference of the IEEE Engineering in Medicine and Biology Society. IEEE Engineering in Medicine and Biology Society. Conference*, *2*, 1415–8. https://doi.org/10.1109/IEMBS.2005.1616695

Dell'acqua, F., Scifo, P., Rizzo, G., Catani, M., Simmons, A., Scotti, G., & Fazio, F. (2010). A modified damped Richardson-Lucy algorithm to reduce isotropic background effects in spherical deconvolution. *NeuroImage*, *49*(2), 1446–58. https://doi.org/10.1016/j.neuroimage.2009.09.033

Dennis, E. L., Jahanshad, N., Rudie, J. D., Brown, J. A., Johnson, K., McMahon, K. L., … Thompson, P. M. (2011). Altered structural brain connectivity in healthy carriers of the autism risk gene, CNTNAP2. *Brain Connectivity*, *1*(6), 447–59. https://doi.org/10.1089/brain.2011.0064

Díaz-Manera, J., Llauger, J., Gallardo, E., & Illa, I. (2015). Muscle MRI in muscular dystrophies. *Acta Myologica : Myopathies and Cardiomyopathies : Official Journal of the Mediterranean Society of Myology*, *34*(2–3), 95–108. Retrieved from http://www.ncbi.nlm.nih.gov/pubmed/27199536

Dole, M., Meunier, F., & Hoen, M. (2013). Gray and white matter distribution in dyslexia: a VBM study of superior temporal gyrus asymmetry. *PloS One*, *8*(10), e76823. https://doi.org/10.1371/journal.pone.0076823

Eicher, J. D., & Gruen, J. R. (2013). Imaging-genetics in dyslexia: connecting risk genetic variants to brain neuroimaging and ultimately to reading impairments. *Molecular Genetics and Metabolism*, *110*(3), 201–12. https://doi.org/10.1016/j.ymgme.2013.07.001

Einarsdottir, E., Svensson, I., Darki, F., Peyrard-Janvid, M., Lindvall, J. M., Ameur, A., …

Matsson, H. (2015). Mutation in CEP63 co-segregating with developmental dyslexia in a Swedish family. *Human Genetics*, *134*(11–12), 1239–48. https://doi.org/10.1007/s00439-015-1602-1

Einstein, A. (1905). Über die von der molekularkinetischen Theorie der Wärme geforderte Bewegung von in ruhenden Flüssigkeiten suspendierten Teilchen. *Annalen Der Physik*, *322*(8), 549–560. https://doi.org/10.1002/andp.19053220806

Fick, A. (1855). Ueber Diffusion. *Annalen Der Physik Und Chemie*, *170*(1), 59–86. https://doi.org/10.1002/andp.18551700105

Filli, L., Boss, A., Wurnig, M. C., Kenkel, D., Andreisek, G., & Guggenberger, R. (2015). Dynamic intravoxel incoherent motion imaging of skeletal muscle at rest and after exercise. *NMR in Biomedicine*, *28*(2), 240–246. https://doi.org/10.1002/nbm.3245

Filli, L., Wurnig, M. C., Luechinger, R., Eberhardt, C., Guggenberger, R., & Boss, A. (2015). Whole-body intravoxel incoherent motion imaging. *European Radiology*, *25*(7), 2049–58. https://doi.org/10.1007/s00330-014-3577-z

Fischer, D., Hafner, P., Rubino, D., Schmid, M., Neuhaus, C., Jung, H., … Bonati, U. (2016). The 6-minute walk test, motor function measure and quantitative thigh muscle MRI in Becker muscular dystrophy: A cross-sectional study. *Neuromuscular Disorders : NMD*, *26*(7), 414–22. https://doi.org/10.1016/j.nmd.2016.04.009

Fischer, D., Walter, M. C., Kesper, K., Petersen, J. A., Aurino, S., Nigro, V., … Schröder, R. (2005). Diagnostic value of muscle MRI in differentiating LGMD2I from other LGMDs. *Journal of Neurology*, *252*(5), 538–47. https://doi.org/10.1007/s00415-005-0684-4

Fischl, B., & Dale, a M. (2000). Measuring the thickness of the human cerebral cortex from magnetic resonance images. *Proceedings of the National Academy of Sciences of the United States of America*, *97*(20), 11050–5. https://doi.org/10.1073/pnas.200033797

Fischmann, A., Hafner, P., Gloor, M., Schmid, M., Klein, A., Pohlman, U., … Fischer, D. (2013). Quantitative MRI and loss of free ambulation in Duchenne muscular dystrophy. *Journal of Neurology*, *260*(4), 969–74. https://doi.org/10.1007/s00415-012-6733-x

Francke, U. (1999). Williams-Beuren syndrome: genes and mechanisms. *Human Molecular Genetics*, *8*(10), 1947–54. Retrieved from

http://www.ncbi.nlm.nih.gov/pubmed/10469848

Froeling, M., Nederveen, A. J., Heijtel, D. F. R., Lataster, A., Bos, C., Nicolay, K., … Strijkers, G. J. (2012). Diffusion-tensor MRI reveals the complex muscle architecture of the human forearm. *Journal of Magnetic Resonance Imaging*, *36*(1), 237–248. https://doi.org/10.1002/jmri.23608

Froeling, M., Nederveen, A. J., Nicolay, K., & Strijkers, G. J. (2013). DTI of human skeletal muscle: the effects of diffusion encoding parameters, signal-to-noise ratio and T2 on tensor indices and fiber tracts. *NMR in Biomedicine*, *26*(11), 1339–52. https://doi.org/10.1002/nbm.2959

Froeling, M., Oudeman, J., Strijkers, G. J., Maas, M., Drost, M. R., Nicolay, K., & Nederveen, A. J. (2015). Muscle changes detected with diffusion-tensor imaging after long-distance running. *Radiology*, *274*(2), 548–62. https://doi.org/10.1148/radiol.14140702

Froeling, M., Oudeman, J., Van Den Berg, S., Nicolay, K., Maas, M., Strijkers, G. J., … Nederveen, A. J. (2010). Reproducibility of diffusion tensor imaging in human forearm muscles at 3.0 T in a clinical setting. *Magnetic Resonance in Medicine*, *64*(4), 1182–1190. https://doi.org/10.1002/mrm.22477

Galbán, C. J., Maderwald, S., Uffmann, K., de Greiff, A., & Ladd, M. E. (2004). Diffusive sensitivity to muscle architecture: a magnetic resonance diffusion tensor imaging study of the human calf. *European Journal of Applied Physiology*, *93*(3), 253–62. https://doi.org/10.1007/s00421-004-1186-2

Girard, G., Whittingstall, K., Deriche, R., & Descoteaux, M. (2014). Towards quantitative connectivity analysis: reducing tractography biases. *NeuroImage*, *98*, 266–78. https://doi.org/10.1016/j.neuroimage.2014.04.074

Gori, S., Seitz, A. R., Ronconi, L., Franceschini, S., & Facoetti, A. (2015). Multiple Causal Links Between Magnocellular-Dorsal Pathway Deficit and Developmental Dyslexia. *Cerebral Cortex (New York, N.Y. : 1991)*. https://doi.org/10.1093/cercor/bhv206

Gottesman, I. I., & Gould, T. D. (2003). The endophenotype concept in psychiatry: etymology and strategic intentions. *The American Journal of Psychiatry*, *160*(4), 636–45. https://doi.org/10.1176/appi.ajp.160.4.636

Graham, S. A., & Fisher, S. E. (2013). Decoding the genetics of speech and language. *Current Opinion in Neurobiology*, *23*(1), 43–51. https://doi.org/10.1016/j.conb.2012.11.006

Guglielmetti, C., Veraart, J., Roelant, E., Mai, Z., Daans, J., Van Audekerke, J., … Verhoye, M. (2016). Diffusion kurtosis imaging probes cortical alterations and white matter pathology following cuprizone induced demyelination and spontaneous remyelination. *NeuroImage*, *125*, 363–77. https://doi.org/10.1016/j.neuroimage.2015.10.052

Hahn, E. L. (1950). Spin Echoes. *Physical Review E*, *80*(580). https://doi.org/https://doi.org/10.1103/PhysRev.80.580

Han, X., Jovicich, J., Salat, D., van der Kouwe, A., Quinn, B., Czanner, S., … Fischl, B. (2006). Reliability of MRI-derived measurements of human cerebral cortical thickness: the effects of field strength, scanner upgrade and manufacturer. *NeuroImage*, *32*(1), 180–94. https://doi.org/10.1016/j.neuroimage.2006.02.051

Hazlewood, C. F., Chang, D. C., Nichols, B. L., & Woessner, D. E. (1974). Nuclear magnetic resonance transverse relaxation times of water protons in skeletal muscle. *Biophysical Journal*, *14*(8), 583–606. https://doi.org/10.1016/S0006-3495(74)85937-0

Hiepe, P., Gussew, A., Rzanny, R., Anders, C., Walther, M., Scholle, H.-C., & Reichenbach, J. R. (2014). Interrelations of muscle functional MRI, diffusion-weighted MRI and (31) P-MRS in exercised lower back muscles. *NMR in Biomedicine*, *27*(8), 958–70. https://doi.org/10.1002/nbm.3141

Hoeft, F., Barnea-Goraly, N., Haas, B. W., Golarai, G., Ng, D., Mills, D., … Reiss, A. L. (2007). More is not always better: increased fractional anisotropy of superior longitudinal fasciculus associated with poor visuospatial abilities in Williams syndrome. *The Journal of Neuroscience : The Official Journal of the Society for Neuroscience*, *27*(44), 11960–5. https://doi.org/10.1523/JNEUROSCI.3591-07.2007

Hoogman, M., Guadalupe, T., Zwiers, M. P., Klarenbeek, P., Francks, C., & Fisher, S. E. (2014). Assessing the effects of common variation in the FOXP2 gene on human brain structure. *Frontiers in Human Neuroscience*, *8*, 473. https://doi.org/10.3389/fnhum.2014.00473

Hooijmans, M. T., Damon, B. M., Froeling, M., Versluis, M. J., Burakiewicz, J.,

Verschuuren, J. J. G. M., … Kan, H. E. (2015). Evaluation of skeletal muscle DTI in patients with duchenne muscular dystrophy. *NMR in Biomedicine*, (October), n/a-n/a. https://doi.org/10.1002/nbm.3427

Hua, K., Zhang, J., Wakana, S., Jiang, H., Li, X., Reich, D. S., … Mori, S. (2008). Tract probability maps in stereotaxic spaces: analyses of white matter anatomy and tract-specific quantification. *NeuroImage*, *39*(1), 336–47. https://doi.org/10.1016/j.neuroimage.2007.07.053

Iima, M., & Le Bihan, D. (2016). Clinical Intravoxel Incoherent Motion and Diffusion MR Imaging: Past, Present, and Future. *Radiology*, *278*(1), 13–32. https://doi.org/10.1148/radiol.2015150244

Im, K., Pienaar, R., Paldino, M. J., Gaab, N., Galaburda, A. M., & Grant, P. E. (2012). Quantification and Discrimination of Abnormal Sulcal Patterns in Polymicrogyria. *Cerebral Cortex (New York, N.Y. : 1991)*, *23*(12), 3007–15. https://doi.org/10.1093/cercor/bhs292

Irfanoglu, M. O., Modi, P., Nayak, A., Hutchinson, E. B., Sarlls, J., & Pierpaoli, C. (2015). DR-BUDDI (Diffeomorphic Registration for Blip-Up blip-Down Diffusion Imaging) method for correcting echo planar imaging distortions. *NeuroImage*, *106*, 284–99. https://doi.org/10.1016/j.neuroimage.2014.11.042

Jackowski, A. P., Rando, K., Maria de Araújo, C., Del Cole, C. G., Silva, I., & Tavares de Lacerda, A. L. (2009). Brain abnormalities in Williams syndrome: a review of structural and functional magnetic resonance imaging findings. *European Journal of Paediatric Neurology : EJPN : Official Journal of the European Paediatric Neurology Society*, *13*(4), 305–16. https://doi.org/10.1016/j.ejpn.2008.07.002

Jamadar, S., Powers, N. R., Meda, S. A., Calhoun, V. D., Gelernter, J., Gruen, J. R., & Pearlson, G. D. (2013). Genetic influences of resting state fMRI activity in language-related brain regions in healthy controls and schizophrenia patients: a pilot study. *Brain Imaging and Behavior*, *7*(1), 15–27. https://doi.org/10.1007/s11682-012-9168-1

Janssen, B., Voet, N., Geurts, A., van Engelen, B., & Heerschap, A. (2016). Quantitative MRI reveals decelerated fatty infiltration in muscles of active FSHD patients. *Neurology*, *86*(18), 1700–7. https://doi.org/10.1212/WNL.0000000000002640

Jenkinson, M., Bannister, P., Brady, M., & Smith, S. (2002). Improved optimization for the robust and accurate linear registration and motion correction of brain images. *NeuroImage*, *17*(2), 825–41. Retrieved from http://www.ncbi.nlm.nih.gov/pubmed/12377157

Jenkinson, M., Beckmann, C. F., Behrens, T. E. J., Woolrich, M. W., & Smith, S. M. (2012). FSL. *NeuroImage*, *62*(2), 782–90. https://doi.org/10.1016/j.neuroimage.2011.09.015

Jenkinson, M., & Smith, S. (2001). A global optimisation method for robust affine registration of brain images. *Medical Image Analysis*, *5*(2), 143–56. Retrieved from http://www.ncbi.nlm.nih.gov/pubmed/11516708

Jensen, J. H., & Helpern, J. a. (2010). MRI quantification of non-Gaussian water diffusion by kurtosis analysis. *NMR in Biomedicine*, *23*(7), 698–710. https://doi.org/10.1002/nbm.1518

Jensen, J. H., Helpern, J. a, Ramani, A., Lu, H., & Kaczynski, K. (2005). Diffusional kurtosis imaging: the quantification of non-gaussian water diffusion by means of magnetic resonance imaging. *Magnetic Resonance in Medicine : Official Journal of the Society of Magnetic Resonance in Medicine / Society of Magnetic Resonance in Medicine*, *53*(6), 1432–40. https://doi.org/10.1002/mrm.20508

Jeurissen, B., Leemans, A., Tournier, J.-D., Jones, D. K., & Sijbers, J. (2013). Investigating the prevalence of complex fiber configurations in white matter tissue with diffusion magnetic resonance imaging. *Human Brain Mapping*, *34*(11), 2747–66. https://doi.org/10.1002/hbm.22099

Jeurissen, B., Tournier, J.-D., Dhollander, T., Connelly, A., & Sijbers, J. (2014). Multi-tissue constrained spherical deconvolution for improved analysis of multi-shell diffusion MRI data. *NeuroImage*. https://doi.org/10.1016/j.neuroimage.2014.07.061

Jezzard, P., & Balaban, R. S. (1995). Correction for geometric distortion in echo planar images from B0 field variations. *Magnetic Resonance in Medicine*, *34*(1), 65–73. https://doi.org/10.1002/mrm.1910340111

Karampinos, D. C., King, K. F., Sutton, B. P., & Georgiadis, J. G. (2010). Intravoxel partially coherent motion technique: Characterization of the anisotropy of skeletal muscle microvasculature. *Journal of Magnetic Resonance Imaging*, *31*(4), 942–953.

https://doi.org/10.1002/jmri.22100

Keil, V. C., Madler, B., Schild, H. H., & Hadizadeh, D. R. (2015). Evaluating a Semi-continuous Multi-compartmental Intra-Voxel Incoherent Motion (IVIM) Model in the Brain : How Does the Method Influence the Results in IVIM ? In *International Society for Magnetic Resonance in Medicine*. Toronto, Canada.

Kiselev, V. G., Hahn, K. R., & Auer, D. P. (2003). Is the brain cortex a fractal? *NeuroImage*, *20*(3), 1765–1774. https://doi.org/10.1016/S1053-8119(03)00380-X

Klein, S., Staring, M., Murphy, K., Viergever, M. A., & Pluim, J. P. W. (2010). elastix: a toolbox for intensity-based medical image registration. *IEEE Transactions on Medical Imaging*, *29*(1), 196–205. https://doi.org/10.1109/TMI.2009.2035616

Koay, C. G., Chang, L.-C., Carew, J. D., Pierpaoli, C., & Basser, P. J. (2006). A unifying theoretical and algorithmic framework for least squares methods of estimation in diffusion tensor imaging. *Journal of Magnetic Resonance (San Diego, Calif. : 1997)*, *182*(1), 115–25. https://doi.org/10.1016/j.jmr.2006.06.020

Kronbichler, M., Wimmer, H., Staffen, W., Hutzler, F., Mair, A., & Ladurner, G. (2008). Developmental dyslexia: gray matter abnormalities in the occipitotemporal cortex. *Human Brain Mapping*, *29*(5), 613–25. https://doi.org/10.1002/hbm.20425

Kurtzke, J. F. (1983). Rating neurologic impairment in multiple sclerosis: an expanded disability status scale (EDSS). *Neurology*, *33*(11), 1444–52. Retrieved from http://www.ncbi.nlm.nih.gov/pubmed/6685237

Lai, C. S. L., Gerrelli, D., Monaco, A. P., Fisher, S. E., & Copp, A. J. (2003). FOXP2 expression during brain development coincides with adult sites of pathology in a severe speech and language disorder. *Brain : A Journal of Neurology*, *126*(Pt 11), 2455–62. https://doi.org/10.1093/brain/awg247

Le Bihan, D. (2013). Apparent diffusion coefficient and beyond: what diffusion MR imaging can tell us about tissue structure. *Radiology*, *268*(2), 318–22. https://doi.org/10.1148/radiol.13130420

Le Bihan, D., & Breton, E. (1985). Imagerie de diffusion in-vivo par résonance magnétique nucléaire. *Comptes-Rendus de l'Académie Des Sciences*, *93*(5), 27–34.

Le Bihan, D., Breton, E., Lallemand, D., Grenier, P., Cabanis, E., & Laval-Jeantet, M. (1986). MR imaging of intravoxel incoherent motions: application to diffusion and perfusion in neurologic disorders. *Radiology*, *161*(2), 401–7. https://doi.org/10.1148/radiology.161.2.3763909

Le Bihan, D., Poupon, C., Amadon, A., & Lethimonnier, F. (2006). Artifacts and pitfalls in diffusion MRI. *Journal of Magnetic Resonance Imaging : JMRI*, *24*(3), 478–88. https://doi.org/10.1002/jmri.20683

Leemans, A., & Jones, D. K. (2009). The B-matrix must be rotated when correcting for subject motion in DTI data. *Magnetic Resonance in Medicine*, *61*(6), 1336–49. https://doi.org/10.1002/mrm.21890

Leung, D. G., Carrino, J. A., Wagner, K. R., & Jacobs, M. A. (2015). Whole-body magnetic resonance imaging evaluation of facioscapulohumeral muscular dystrophy. *Muscle & Nerve*, *52*(4), 512–20. https://doi.org/10.1002/mus.24569

Løkken, N., Hedermann, G., Thomsen, C., & Vissing, J. (2016). Contractile properties are disrupted in Becker muscular dystrophy, but not in limb girdle type 2I. *Annals of Neurology*, *80*(3), 466–71. https://doi.org/10.1002/ana.24743

Lu, Y., Jansen, J. F. a, Mazaheri, Y., Stambuk, H. E., Koutcher, J. a., & Shukla-Dave, A. (2012). Extension of the intravoxel incoherent motion model to non-gaussian diffusion in head and neck cancer. *Journal of Magnetic Resonance Imaging*, *36*(5), 1088–1096. https://doi.org/10.1002/jmri.23770

Luciani, A., Vignaud, A., Cavet, M., Nhieu, J. T. Van, Mallat, A., Ruel, L., … Rahmouni, A. (2008). Liver cirrhosis: intravoxel incoherent motion MR imaging--pilot study. *Radiology*, *249*(3), 891–9. https://doi.org/10.1148/radiol.2493080080

Ludwig, K. U., Roeske, D., Herms, S., Schumacher, J., Warnke, A., Plume, E., … Hoffmann, P. (2010). Variation in GRIN2B contributes to weak performance in verbal short-term memory in children with dyslexia. *American Journal of Medical Genetics. Part B, Neuropsychiatric Genetics : The Official Publication of the International Society of Psychiatric Genetics*, *153B*(2), 503–11. https://doi.org/10.1002/ajmg.b.31007

Madler, B., & Coenen, V. A. (2013). Performance Evaluation of Various Numerical Algorithms for a Multi-Compartmental IVIM-Model. In *International Society for*

Magnetic Resonance in Medicine. Salt Lake City, USA.

Madler, B., Hadizadeh, D. R., & Gieseke, J. (2013). Assessment of a Continuous Multi-Compartmental Intra-Voxel Incoherent Motion (IVIM) Model for the Human Brain. In *International Society for Magnetic Resonance in Medicine*. Salt Lake City, USA.

Mandelbrot, B. (1982). *The Fractal Geometry of Nature*.

Marenco, S., Siuta, M. A., Kippenhan, J. S., Grodofsky, S., Chang, W.-L., Kohn, P., … Berman, K. F. (2007). Genetic contributions to white matter architecture revealed by diffusion tensor imaging in Williams syndrome. *Proceedings of the National Academy of Sciences of the United States of America*, *104*(38), 15117–22. https://doi.org/10.1073/pnas.0704311104

Marino, C., Scifo, P., Della Rosa, P. A., Mascheretti, S., Facoetti, A., Lorusso, M. L., … Perani, D. (2014). The DCDC2/intron 2 deletion and white matter disorganization: focus on developmental dyslexia. *Cortex; a Journal Devoted to the Study of the Nervous System and Behavior*, *57*, 227–43. https://doi.org/10.1016/j.cortex.2014.04.016

Marschar, A. M., Kuder, T. A., Stieltjes, B., Nagel, A. M., Bachert, P., & Laun, F. B. (2015). In vivo imaging of the time-dependent apparent diffusional kurtosis in the human calf muscle. *Journal of Magnetic Resonance Imaging*, *41*(6), 1581–1590. https://doi.org/10.1002/jmri.24743

Martens, M. A., Wilson, S. J., & Reutens, D. C. (2008). Research Review: Williams syndrome: a critical review of the cognitive, behavioral, and neuroanatomical phenotype. *Journal of Child Psychology and Psychiatry, and Allied Disciplines*, *49*(6), 576–608. https://doi.org/10.1111/j.1469-7610.2008.01887.x

Mascheretti, S., De Luca, A., Trezzi, V., Peruzzo, D., Marino, C., & Arrigoni, F. (n.d.). Neurogenetics of developmental dyslexia: From genes to behavior through brain neuroimaging and cognitive and sensorial mechanisms. *Translational Psychiatry*, *In Press*.

Mazziotta, J., Toga, A., Evans, A., Fox, P., Lancaster, J., Zilles, K., … Mazoyer, B. (2001). A probabilistic atlas and reference system for the human brain: International Consortium for Brain Mapping (ICBM). *Philosophical Transactions of the Royal Society of London. Series B, Biological Sciences*, *356*(1412), 1293–322.

https://doi.org/10.1098/rstb.2001.0915

McNab, J. A., Edlow, B. L., Witzel, T., Huang, S. Y., Bhat, H., Heberlein, K., … Wald, L. L. (2013). The Human Connectome Project and beyond: initial applications of 300 mT/m gradients. *NeuroImage*, *80*, 234–45. https://doi.org/10.1016/j.neuroimage.2013.05.074

Meda, S. A., Gelernter, J., Gruen, J. R., Calhoun, V. D., Meng, H., Cope, N. A., & Pearlson, G. D. (2008). Polymorphism of DCDC2 Reveals Differences in Cortical Morphology of Healthy Individuals-A Preliminary Voxel Based Morphometry Study. *Brain Imaging and Behavior*, *2*(1), 21–26. https://doi.org/10.1007/s11682-007-9012-1

Meng, H., Powers, N. R., Tang, L., Cope, N. A., Zhang, P.-X., Fuleihan, R., … Gruen, J. R. (2011). A dyslexia-associated variant in DCDC2 changes gene expression. *Behavior Genetics*, *41*(1), 58–66. https://doi.org/10.1007/s10519-010-9408-3

Mercuri, E., Bushby, K., Ricci, E., Birchall, D., Pane, M., Kinali, M., … Muntoni, F. (2005). Muscle MRI findings in patients with limb girdle muscular dystrophy with calpain 3 deficiency (LGMD2A) and early contractures. *Neuromuscular Disorders : NMD*, *15*(2), 164–71. https://doi.org/10.1016/j.nmd.2004.10.008

Mori, S., Wakana, S., van Zijl, P. C. M., & Nagae-Poetscher, L. M. (2005). *MRI Atlas of Human White Matter*. book, Elsevier Science. Retrieved from http://books.google.ca/books?id=ltwRYlvFNLIC

Moseley, M. E., Cohen, Y., Kucharczyk, J., Mintorovitch, J., Asgari, H. S., Wendland, M. F., … Norman, D. (1990). Diffusion-weighted MR imaging of anisotropic water diffusion in cat central nervous system. *Radiology*, *176*(2), 439–45. https://doi.org/10.1148/radiology.176.2.2367658

Nagy, Z., & Weiskopf, N. (2008). Efficient fat suppression by slice-selection gradient reversal in twice-refocused diffusion encoding. *Magnetic Resonance in Medicine*, *60*(5), 1256–60. https://doi.org/10.1002/mrm.21746

Nguyen, A., Ledoux, J.-B., Omoumi, P., Becce, F., Forget, J., & Federau, C. (2016). Application of intravoxel incoherent motion perfusion imaging to shoulder muscles after a lift-off test of varying duration. *NMR in Biomedicine*, *29*(1), 66–73. https://doi.org/10.1002/nbm.3449

Nigro, V., Aurino, S., & Piluso, G. (2011). Limb girdle muscular dystrophies: update on genetic diagnosis and therapeutic approaches. *Current Opinion in Neurology*, *24*(5), 429–36. https://doi.org/10.1097/WCO.0b013e32834aa38d

Ojima, K., Kawabata, Y., Nakao, H., Nakao, K., Doi, N., Kitamura, F., … Sorimachi, H. (2010). Dynamic distribution of muscle-specific calpain in mice has a key role in physical-stress adaptation and is impaired in muscular dystrophy. *The Journal of Clinical Investigation*, *120*(8), 2672–83. https://doi.org/10.1172/JCI40658

Oliveira, P. P. D. M., Valente, K. D., Shergill, S. S., Leite, C. D. C., & Amaro, E. (2010). Cortical thickness reduction of normal appearing cortex in patients with polymicrogyria. *Journal of Neuroimaging*, *20*(1), 46–52. https://doi.org/10.1111/j.1552-6569.2009.00372.x

Oudeman, J., Nederveen, A. J., Strijkers, G. J., Maas, M., Luijten, P. R., & Froeling, M. (2015). Techniques and applications of skeletal muscle diffusion tensor imaging: A review. *Journal of Magnetic Resonance Imaging*, n/a-n/a. https://doi.org/10.1002/jmri.25016

Pajevic, S., & Pierpaoli, C. (1999). Color schemes to represent the orientation of anisotropic tissues from diffusion tensor data: application to white matter fiber tract mapping in the human brain. *Magnetic Resonance in Medicine*, *42*(3), 526–40. Retrieved from http://www.ncbi.nlm.nih.gov/pubmed/10467297

Pang, H., Ren, Y., Dang, X., Feng, X., Yao, Z., Wu, J., … Zhang, Y. (2015). Diffusional kurtosis imaging for differentiating between high-grade glioma and primary central nervous system lymphoma. *Journal of Magnetic Resonance Imaging : JMRI*. https://doi.org/10.1002/jmri.25090

Park, H. W., Kim, D. J., & Cho, Z. H. (1987). Gradient reversal technique and its applications to chemical-shift-related NMR imaging. *Magnetic Resonance in Medicine*, *4*(6), 526–36. Retrieved from http://www.ncbi.nlm.nih.gov/pubmed/3613953

Patenaude, B., Smith, S. M., Kennedy, D. N., & Jenkinson, M. (2011). A Bayesian model of shape and appearance for subcortical brain segmentation. *NeuroImage*, *56*(3), 907–22. https://doi.org/10.1016/j.neuroimage.2011.02.046

Paulesu, E., Danelli, L., & Berlingeri, M. (2014). Reading the dyslexic brain: multiple

dysfunctional routes revealed by a new meta-analysis of PET and fMRI activation studies. *Frontiers in Human Neuroscience*, *8*, 830. https://doi.org/10.3389/fnhum.2014.00830

Pennington, B. F. (2006). From single to multiple deficit models of developmental disorders. *Cognition*, *101*(2), 385–413. https://doi.org/10.1016/j.cognition.2006.04.008

Pergola, G., Di Carlo, P., Andriola, I., Gelao, B., Torretta, S., Attrotto, M. T., … Bertolino, A. (2016). Combined effect of genetic variants in the GluN2B coding gene (GRIN2B) on prefrontal function during working memory performance. *Psychological Medicine*, *46*(6), 1135–50. https://doi.org/10.1017/S0033291715002639

Pernet, C. R., Poline, J. B., Demonet, J. F., & Rousselet, G. A. (2009). Brain classification reveals the right cerebellum as the best biomarker of dyslexia. *BMC Neuroscience*, *10*, 67. https://doi.org/10.1186/1471-2202-10-67

Peterson, R. L., & Pennington, B. F. (2015). Developmental dyslexia. *Annual Review of Clinical Psychology*, *11*, 283–307. https://doi.org/10.1146/annurev-clinpsy-032814-112842

Pichiecchio, A., Rossi, M., Cinnante, C., Colafati, S. G., De Icco, R., Parini, R., … Di Rocco, M. (2016). Muscle MRI of classic infantile Pompe patients: Fatty substitution and edema-like changes. *Muscle & Nerve*. https://doi.org/10.1002/mus.25417

Pierpaoli, C., & Basser, P. J. (1996). Toward a quantitative assessment of diffusion anisotropy. *Magnetic Resonance in Medicine*. Retrieved from http://onlinelibrary.wiley.com/doi/10.1002/mrm.1910360612/full

Pierpaoli, C., Walker, L., Irfanoglu, M. O., Barnett, A. S., Basser, P. J., Chang, L.-C., … Wu, M. T. (2010). TORTOISE: an integrated software package for processing of diffusion MRI data. *ISMRM 18th Annual Meeting*, 1597.

Pinel, P., Fauchereau, F., Moreno, A., Barbot, A., Lathrop, M., Zelenika, D., … Dehaene, S. (2012). Genetic variants of FOXP2 and KIAA0319/TTRAP/THEM2 locus are associated with altered brain activation in distinct language-related regions. *The Journal of Neuroscience : The Official Journal of the Society for Neuroscience*, *32*(3), 817–25. https://doi.org/10.1523/JNEUROSCI.5996-10.2012

Polavarapu, K., Manjunath, M., Preethish-Kumar, V., Sekar, D., Vengalil, S., Thomas, P., … Nalini, A. (2016). Muscle MRI in Duchenne muscular dystrophy: Evidence of a distinctive pattern. *Neuromuscular Disorders : NMD*, *26*(11), 768–774. https://doi.org/10.1016/j.nmd.2016.09.002

Polman, C. H., Reingold, S. C., Banwell, B., Clanet, M., Cohen, J. A., Filippi, M., … Wolinsky, J. S. (2011). Diagnostic criteria for multiple sclerosis: 2010 Revisions to the McDonald criteria. *Annals of Neurology*, *69*(2), 292–302. https://doi.org/10.1002/ana.22366

Polman, C. H., Reingold, S. C., Edan, G., Filippi, M., Hartung, H.-P., Kappos, L., … Wolinsky, J. S. (2005). Diagnostic criteria for multiple sclerosis: 2005 revisions to the "McDonald Criteria". *Annals of Neurology*, *58*(6), 840–6. https://doi.org/10.1002/ana.20703

Ponrartana, S., Ramos-Platt, L., Wren, T. A. L., Hu, H. H., Perkins, T. G., Chia, J. M., & Gilsanz, V. (2014). Effectiveness of diffusion tensor imaging in assessing disease severity in Duchenne muscular dystrophy: preliminary study. *Pediatric Radiology*. https://doi.org/10.1007/s00247-014-3187-6

Ponrartana, S., Ramos-Platt, L., Wren, T. A. L., Hu, H. H., Perkins, T. G., Chia, J. M., & Gilsanz, V. (2015). Effectiveness of diffusion tensor imaging in assessing disease severity in Duchenne muscular dystrophy: preliminary study. *Pediatric Radiology*, *45*(4), 582–9. https://doi.org/10.1007/s00247-014-3187-6

Powers, N. R., Eicher, J. D., Butter, F., Kong, Y., Miller, L. L., Ring, S. M., … Gruen, J. R. (2013). Alleles of a polymorphic ETV6 binding site in DCDC2 confer risk of reading and language impairment. *American Journal of Human Genetics*, *93*(1), 19–28. https://doi.org/10.1016/j.ajhg.2013.05.008

Qi, J., Olsen, N. J., Price, R. R., Winston, J. A., & Park, J. H. (2008). Diffusion-weighted imaging of inflammatory myopathies: polymyositis and dermatomyositis. *Journal of Magnetic Resonance Imaging : JMRI*, *27*(1), 212–7. https://doi.org/10.1002/jmri.21209

Reese, T. G., Heid, O., Weisskoff, R. M., & Wedeen, V. J. (2003). Reduction of eddy-current-induced distortion in diffusion MRI using a twice-refocused spin echo. *Magnetic Resonance in Medicine*, *49*(1), 177–82. https://doi.org/10.1002/mrm.10308

Rimrodt, S. L., Peterson, D. J., Denckla, M. B., Kaufmann, W. E., & Cutting, L. E. (2010). White matter microstructural differences linked to left perisylvian language network in children with dyslexia. *Cortex; a Journal Devoted to the Study of the Nervous System and Behavior*, *46*(6), 739–49. https://doi.org/10.1016/j.cortex.2009.07.008

Rinaldi, F., Calabrese, M., Grossi, P., Puthenparampil, M., Perini, P., & Gallo, P. (2010). Cortical lesions and cognitive impairment in multiple sclerosis. *Neurological Sciences : Official Journal of the Italian Neurological Society and of the Italian Society of Clinical Neurophysiology*, *31*(Suppl 2), S235-7. https://doi.org/10.1007/s10072-010-0368-4

Sadaka, Y., Verhey, L. H., Shroff, M. M., Branson, H. M., Arnold, D. L., Narayanan, S., … Canadian Pediatric Demyelinating Disease Network. (2012). 2010 McDonald criteria for diagnosing pediatric multiple sclerosis. *Annals of Neurology*, *72*(2), 211–23. https://doi.org/10.1002/ana.23575

Sahraian, M. A., Radue, E.-W., Haller, S., & Kappos, L. (2010). Black holes in multiple sclerosis: definition, evolution, and clinical correlations. *Acta Neurologica Scandinavica*, *122*(1), 1–8. https://doi.org/10.1111/j.1600-0404.2009.01221.x

Sarkozy, A., Deschauer, M., Carlier, R.-Y., Schrank, B., Seeger, J., Walter, M. C., … Straub, V. (2012). Muscle MRI findings in limb girdle muscular dystrophy type 2L. *Neuromuscular Disorders : NMD*, *22 Suppl 2*, S122-9. https://doi.org/10.1016/j.nmd.2012.05.012

Scerri, T. S., Darki, F., Newbury, D. F., Whitehouse, A. J. O., Peyrard-Janvid, M., Matsson, H., … Paracchini, S. (2012). The dyslexia candidate locus on 2p12 is associated with general cognitive ability and white matter structure. *PloS One*, *7*(11), e50321. https://doi.org/10.1371/journal.pone.0050321

Scerri, T. S., & Schulte-Körne, G. (2010). Genetics of developmental dyslexia. *European Child & Adolescent Psychiatry*, *19*(3), 179–97. https://doi.org/10.1007/s00787-009-0081-0

Schmitt, F., Stehling, M. K., & Turner, R. (1998). *Echo-Planar Imaging*. Springer Berlin Heidelberg.

Schneider, M. J., Dietrich, O., Ingrisch, M., Helck, A., Winter, K. S., Reiser, M. F., … Notohamiprodjo, M. (2016). Intravoxel Incoherent Motion Magnetic Resonance

Imaging in Partially Nephrectomized Kidneys. *Investigative Radiology*, *51*(5), 323–30. https://doi.org/10.1097/RLI.0000000000000244

Scott-Van Zeeland, A. A., Abrahams, B. S., Alvarez-Retuerto, A. I., Sonnenblick, L. I., Rudie, J. D., Ghahremani, D., … Bookheimer, S. Y. (2010). Altered functional connectivity in frontal lobe circuits is associated with variation in the autism risk gene CNTNAP2. *Science Translational Medicine*, *2*(56), 56ra80. https://doi.org/10.1126/scitranslmed.3001344

Seki, A., Koeda, T., Sugihara, S., Kamba, M., Hirata, Y., Ogawa, T., & Takeshita, K. (2001). A functional magnetic resonance imaging study during sentence reading in Japanese dyslexic children. *Brain & Development*, *23*(5), 312–6. Retrieved from http://www.ncbi.nlm.nih.gov/pubmed/11504602

Shaywitz, B. A., Shaywitz, S. E., Pugh, K. R., Mencl, W. E., Fulbright, R. K., Skudlarski, P., … Gore, J. C. (2002). Disruption of posterior brain systems for reading in children with developmental dyslexia. *Biological Psychiatry*, *52*(2), 101–10. Retrieved from http://www.ncbi.nlm.nih.gov/pubmed/12114001

Sigmund, E. E., Novikov, D. S., Sui, D., Ukpebor, O., Baete, S., Babb, J. S., … Fieremans, E. (2014). Time-dependent diffusion in skeletal muscle with the random permeable barrier model (RPBM): Application to normal controls and chronic exertional compartment syndrome patients. *NMR in Biomedicine*, *27*(5), 519–528. https://doi.org/10.1002/nbm.3087

Sigmund, E. E., Vivier, P.-H., Sui, D., Lamparello, N. a., Tantillo, K., Mikheev, a., … Chandarana, H. (2012). Intravoxel Incoherent Motion and Diffusion-Tensor Imaging in Renal Tissue under Hydration and Furosemide Flow Challenges. *Radiology*, *263*(3), 758–769. https://doi.org/10.1148/radiol.12111327

Sijbers, J., & den Dekker, A. J. (2004). Maximum likelihood estimation of signal amplitude and noise variance from MR data. *Magnetic Resonance in Medicine*, *51*(3), 586–94. https://doi.org/10.1002/mrm.10728

Silani, G., Frith, U., Demonet, J.-F., Fazio, F., Perani, D., Price, C., … Paulesu, E. (2005). Brain abnormalities underlying altered activation in dyslexia: a voxel based morphometry study. *Brain : A Journal of Neurology*, *128*(Pt 10), 2453–61.

https://doi.org/10.1093/brain/awh579

Skeide, M. A., Kraft, I., Müller, B., Schaadt, G., Neef, N. E., Brauer, J., … Friederici, A. D. (2016). NRSN1 associated grey matter volume of the visual word form area reveals dyslexia before school. *Brain : A Journal of Neurology*, *139*(Pt 10), 2792–2803. https://doi.org/10.1093/brain/aww153

Smith, R. E., Tournier, J.-D., Calamante, F., & Connelly, A. (2012). Anatomically-constrained tractography: improved diffusion MRI streamlines tractography through effective use of anatomical information. *NeuroImage*, *62*(3), 1924–38. https://doi.org/10.1016/j.neuroimage.2012.06.005

Smith, R. E., Tournier, J.-D., Calamante, F., & Connelly, A. (2013). SIFT: Spherical-deconvolution informed filtering of tractograms. *NeuroImage*, *67*, 298–312. https://doi.org/10.1016/j.neuroimage.2012.11.049

Smith, S. M. (2002). Fast robust automated brain extraction. *Human Brain Mapping*, *17*(3), 143–55. https://doi.org/10.1002/hbm.10062

Smith, S. M., Jenkinson, M., Johansen-Berg, H., Rueckert, D., Nichols, T. E., Mackay, C. E., … Behrens, T. E. J. (2006). Tract-based spatial statistics: voxelwise analysis of multi-subject diffusion data. *NeuroImage*, *31*(4), 1487–505. https://doi.org/10.1016/j.neuroimage.2006.02.024

Smith, S. M., & Nichols, T. E. (2009). Threshold-free cluster enhancement: addressing problems of smoothing, threshold dependence and localisation in cluster inference. *NeuroImage*, *44*(1), 83–98. https://doi.org/10.1016/j.neuroimage.2008.03.061

Spiess, A.-N., & Neumeyer, N. (2010). An evaluation of R2 as an inadequate measure for nonlinear models in pharmacological and biochemical research: a Monte Carlo approach. *BMC Pharmacology*, *10*(1), 6. https://doi.org/10.1186/1471-2210-10-6

Squarcina, L., De Luca, A., Bellani, M., Brambilla, P., Turkheimer, F. E., & Bertoldo, A. (2015). Fractal analysis of MRI data for the characterization of patients with schizophrenia and bipolar disorder. *Physics in Medicine and Biology*, *60*(4), 1697–716. https://doi.org/10.1088/0031-9155/60/4/1697

Steidle, G., & Schick, F. (2015). Addressing spontaneous signal voids in repetitive single-

shot DWI of musculature: spatial and temporal patterns in the calves of healthy volunteers and consideration of unintended muscle activities as underlying mechanism. *NMR in Biomedicine*, (July 2014), n/a-n/a. https://doi.org/10.1002/nbm.3311

Steinbrink, C., Vogt, K., Kastrup, A., Müller, H.-P., Juengling, F. D., Kassubek, J., & Riecker, A. (2008). The contribution of white and gray matter differences to developmental dyslexia: insights from DTI and VBM at 3.0 T. *Neuropsychologia*, *46*(13), 3170–8. https://doi.org/10.1016/j.neuropsychologia.2008.07.015

Stejskal, E. O., & Tanner, J. E. (1965). Spin Diffusion Measurements: Spin Echoes in the Presence of a Time-Dependent Field Gradient. *The Journal of Chemical Physics*, *42*(288). https://doi.org/http://dx.doi.org/10.1063/1.1695690

Stoeck, C. T., von Deuster, C., Genet, M., Atkinson, D., & Kozerke, S. (2016). Second-order motion-compensated spin echo diffusion tensor imaging of the human heart. *Magnetic Resonance in Medicine*, *75*(4), 1669–76. https://doi.org/10.1002/mrm.25784

Stramare, R., Beltrame, V., Dal Borgo, R., Gallimberti, L., Frigo, A. C., Pegoraro, E., … Feltrin, G. P. (2010). MRI in the assessment of muscular pathology: a comparison between limb-girdle muscular dystrophies, hyaline body myopathies and myotonic dystrophies. *La Radiologia Medica*, *115*(4), 585–99. https://doi.org/10.1007/s11547-010-0531-2

Strauss, K. A., Puffenberger, E. G., Huentelman, M. J., Gottlieb, S., Dobrin, S. E., Parod, J. M., … Morton, D. H. (2006). Recessive symptomatic focal epilepsy and mutant contactin-associated protein-like 2. *The New England Journal of Medicine*, *354*(13), 1370–7. https://doi.org/10.1056/NEJMoa052773

Subramony, S. H. (2007). SARA--a new clinical scale for the assessment and rating of ataxia. *Nature Clinical Practice. Neurology*, *3*(3), 136–7. https://doi.org/10.1038/ncpneuro0426

Szafer, A., Zhong, J., Anderson, A. W., & Gore, J. C. (1995). Diffusion-weighted imaging in tissues: theoretical models. *NMR in Biomedicine*, *8*(7–8), 289–96. https://doi.org/8739267

Tan, G. C. Y., Doke, T. F., Ashburner, J., Wood, N. W., & Frackowiak, R. S. J. (2010). Normal variation in fronto-occipital circuitry and cerebellar structure with an autism-associated polymorphism of CNTNAP2. *NeuroImage*, *53*(3), 1030–42.

https://doi.org/10.1016/j.neuroimage.2010.02.018

Tanner, J. E. (1979). Self diffusion of water in frog muscle. *Biophysical Journal*, *28*(1), 107–16. https://doi.org/10.1016/S0006-3495(79)85162-0

Torrey, H. C. (1956). Bloch Equations with Diffusion Terms. *Physical Review E*, *104*(563). https://doi.org/https://doi.org/10.1103/PhysRev.104.563

Tournier, J.-D., Calamante, F., & Connelly, A. (2010). Improved probabilistic streamlines tractography by 2nd order integratio nover fibre orientation distribution. In *International Society for Magnetic Resonance in Medicine*. Stockholm, Sweden.

Tournier, J.-D., Calamante, F., Gadian, D. G., & Connelly, A. (2004). Direct estimation of the fiber orientation density function from diffusion-weighted MRI data using spherical deconvolution. *NeuroImage*, *23*(3), 1176–85. https://doi.org/10.1016/j.neuroimage.2004.07.037

Tournier, J.-D., Yeh, C.-H., Calamante, F., Cho, K.-H., Connelly, A., & Lin, C.-P. (2008). Resolving crossing fibres using constrained spherical deconvolution: validation using diffusion-weighted imaging phantom data. *NeuroImage*, *42*(2), 617–25. https://doi.org/10.1016/j.neuroimage.2008.05.002

Truong, D. T., Che, A., Rendall, A. R., Szalkowski, C. E., LoTurco, J. J., Galaburda, A. M., & Holly Fitch, R. (2014). Mutation of Dcdc2 in mice leads to impairments in auditory processing and memory ability. *Genes, Brain, and Behavior*, *13*(8), 802–11. https://doi.org/10.1111/gbb.12170

Truyen, L., Barkhof, F., Frequin, S. T., Polman, C. H., Tobi, H., Hommes, O. R., & Valk, J. (1996). Magnetic resonance imaging of epilepsy in multiple sclerosis: a case control study. Implications for treatment trials with 4-aminopyridine. *Multiple Sclerosis (Houndmills, Basingstoke, England)*, *1*(4), 213–7. Retrieved from http://www.ncbi.nlm.nih.gov/pubmed/9345437

Turner, R., Le Bihan, D., & Chesnick, A. S. (1991). Echo-planar imaging of diffusion and perfusion. *Magnetic Resonance in Medicine*, *19*(2), 247–53. Retrieved from http://www.ncbi.nlm.nih.gov/pubmed/1881311

Tustison, N. J., Avants, B. B., Cook, P. A., Zheng, Y., Egan, A., Yushkevich, P. A., & Gee, J.

C. (2010). N4ITK: improved N3 bias correction. *IEEE Transactions on Medical Imaging*, *29*(6), 1310–20. https://doi.org/10.1109/TMI.2010.2046908

Tzourio-Mazoyer, N., Landeau, B., Papathanassiou, D., Crivello, F., Etard, O., Delcroix, N., … Joliot, M. (2002). Automated anatomical labeling of activations in SPM using a macroscopic anatomical parcellation of the MNI MRI single-subject brain. *NeuroImage*, *15*(1), 273–89. https://doi.org/10.1006/nimg.2001.0978

V.P.L.S., R. B. F. R. S. H. M. R. S. E. & R. I. A. (1828). XXVII. A brief account of microscopical observations made in the months of June, July and August 1827, on the particles contained in the pollen of plants; and on the general existence of active molecules in organic and inorganic bodies. *Philosophical Magazine Series 2*, *4*(21), 161–173. article. https://doi.org/10.1080/14786442808674769

Van Donkelaar, C. C., Kretzers, L. J., Bovendeerd, P. H., Lataster, L. M., Nicolay, K., Janssen, J. D., & Drost, M. R. (1999). Diffusion tensor imaging in biomechanical studies of skeletal muscle function. *Journal of Anatomy*, *194 (Pt 1*, 79–88. Retrieved from http://www.ncbi.nlm.nih.gov/pubmed/10227669

Van Essen, D. C., Smith, S. M., Barch, D. M., Behrens, T. E. J., Yacoub, E., Ugurbil, K., & WU-Minn HCP Consortium. (2013). The WU-Minn Human Connectome Project: an overview. *NeuroImage*, *80*, 62–79. https://doi.org/10.1016/j.neuroimage.2013.05.041

Vavla, M., Arrigoni, F., Petacchi, E., Nordio, A., De Luca, A., Russo, E., … Martinuzzi, A. (2015). Potential neuroimaging biomarkers validated in Friedrich's Ataxia: DTI and Function mangnetic resonance findings. In *IARC 2015* (p. 25–28 March 2015). Berkshire, England.

Veraart, J., Poot, D. H. J., Van Hecke, W., Blockx, I., Van der Linden, A., Verhoye, M., & Sijbers, J. (2011). More accurate estimation of diffusion tensor parameters using diffusion Kurtosis imaging. *Magnetic Resonance in Medicine*, *65*(1), 138–45. https://doi.org/10.1002/mrm.22603

Vernes, S. C., Newbury, D. F., Abrahams, B. S., Winchester, L., Nicod, J., Groszer, M., … Fisher, S. E. (2008). A functional genetic link between distinct developmental language disorders. *The New England Journal of Medicine*, *359*(22), 2337–45. https://doi.org/10.1056/NEJMoa0802828

Vinckenbosch, E., Robichon, F., & Eliez, S. (2005). Gray matter alteration in dyslexia: converging evidence from volumetric and voxel-by-voxel MRI analyses. *Neuropsychologia*, *43*(3), 324–31. https://doi.org/10.1016/j.neuropsychologia.2004.06.023

von Hohenberg, C. C., Pasternak, O., Kubicki, M., Ballinger, T., Vu, M.-A., Swisher, T., … Shenton, M. E. (2014). White matter microstructure in individuals at clinical high risk of psychosis: a whole-brain diffusion tensor imaging study. *Schizophrenia Bulletin*, *40*(4), 895–903. https://doi.org/10.1093/schbul/sbt079

Vos, S. B., Tax, C. M. W., Luijten, P. R., Ourselin, S., Leemans, A., & Froeling, M. (2016). The importance of correcting for signal drift in diffusion MRI. *Magnetic Resonance in Medicine*, *22*, 4460. https://doi.org/10.1002/mrm.26124

Wang, H., Suh, J. W., Das, S. R., Pluta, J. B., Craige, C., & Yushkevich, P. A. (2013). Multi-Atlas Segmentation with Joint Label Fusion. *IEEE Transactions on Pattern Analysis and Machine Intelligence*, *35*(3), 611–23. https://doi.org/10.1109/TPAMI.2012.143

Wang, Y., Paramasivam, M., Thomas, A., Bai, J., Kaminen-Ahola, N., Kere, J., … Loturco, J. J. (2006). DYX1C1 functions in neuronal migration in developing neocortex. *Neuroscience*, *143*(2), 515–22. https://doi.org/10.1016/j.neuroscience.2006.08.022

Wetscherek, A., Stieltjes, B., & Laun, F. B. (2015). Flow-compensated intravoxel incoherent motion diffusion imaging. *Magnetic Resonance in Medicine*, *74*(2), 410–9. https://doi.org/10.1002/mrm.25410

Whalley, H. C., O'Connell, G., Sussmann, J. E., Peel, A., Stanfield, A. C., Hayiou-Thomas, M. E., … Hall, J. (2011). Genetic variation in CNTNAP2 alters brain function during linguistic processing in healthy individuals. *American Journal of Medical Genetics. Part B, Neuropsychiatric Genetics : The Official Publication of the International Society of Psychiatric Genetics*, *156B*(8), 941–8. https://doi.org/10.1002/ajmg.b.31241

Wilcke, A., Ligges, C., Burkhardt, J., Alexander, M., Wolf, C., Quente, E., … Kirsten, H. (2012). Imaging genetics of FOXP2 in dyslexia. *European Journal of Human Genetics : EJHG*, *20*(2), 224–9. https://doi.org/10.1038/ejhg.2011.160

Willcocks, R. J., Arpan, I. A., Forbes, S. C., Lott, D. J., Senesac, C. R., Senesac, E., … Vandenborne, K. (2014). Longitudinal measurements of MRI-T2 in boys with Duchenne

muscular dystrophy: Effects of age and disease progression. *Neuromuscular Disorders*, *24*(5), 393–401. https://doi.org/10.1016/j.nmd.2013.12.012

Willcocks, R. J., Rooney, W. D., Triplett, W. T., Forbes, S. C., Lott, D. J., Senesac, C. R., … Vandenborne, K. (2016). Multicenter prospective longitudinal study of magnetic resonance biomarkers in a large duchenne muscular dystrophy cohort. *Annals of Neurology*, *79*(4), 535–47. https://doi.org/10.1002/ana.24599

Williams, S. E., Heemskerk, A. M., Welch, E. B., Li, K., Damon, B. M., & Park, J. H. (2013). Quantitative effects of inclusion of fat on muscle diffusion tensor MRI measurements. *Journal of Magnetic Resonance Imaging : JMRI*, *38*(5), 1292–7. https://doi.org/10.1002/jmri.24045

Willis, T. A., Hollingsworth, K. G., Coombs, A., Sveen, M.-L., Andersen, S., Stojkovic, T., … Straub, V. (2014). Quantitative magnetic resonance imaging in limb-girdle muscular dystrophy 2I: a multinational cross-sectional study. *PloS One*, *9*(2), e90377. https://doi.org/10.1371/journal.pone.0090377

Winkler, A. M., Ridgway, G. R., Webster, M. A., Smith, S. M., & Nichols, T. E. (2014). Permutation inference for the general linear model. *NeuroImage*, *92*, 381–97. https://doi.org/10.1016/j.neuroimage.2014.01.060

Wu, E. X., & Cheung, M. M. (2010). MR diffusion kurtosis imaging for neural tissue characterization. *NMR in Biomedicine*, *23*(7), 836–48. https://doi.org/10.1002/nbm.1506

Zalesky, A., Fornito, A., & Bullmore, E. T. (2010). Network-based statistic: identifying differences in brain networks. *NeuroImage*, *53*(4), 1197–207. https://doi.org/10.1016/j.neuroimage.2010.06.041

Zhang, H., Avants, B. B., Yushkevich, P. A., Woo, J. H., Wang, S., McCluskey, L. F., … Gee, J. C. (2007). High-dimensional spatial normalization of diffusion tensor images improves the detection of white matter differences: an example study using amyotrophic lateral sclerosis. *IEEE Transactions on Medical Imaging*, *26*(11), 1585–97. https://doi.org/10.1109/TMI.2007.906784

Zhang, H. G., Schneider, T., Wheeler-Kingshott, C. a, & Alexander, D. C. (2012). NODDI: practical in vivo neurite orientation dispersion and density imaging of the human brain. *NeuroImage*, *61*(4), 1000–16. https://doi.org/10.1016/j.neuroimage.2012.03.072

Zhang, H., Yushkevich, P. A., Alexander, D. C., & Gee, J. C. (2006). Deformable registration of diffusion tensor MR images with explicit orientation optimization. *Medical Image Analysis*, *10*(5), 764–85. https://doi.org/10.1016/j.media.2006.06.004

Zhang, Y., Brady, M., & Smith, S. (2001). Segmentation of brain MR images through a hidden Markov random field model and the expectation-maximization algorithm. *IEEE Transactions on Medical Imaging*, *20*(1), 45–57. https://doi.org/10.1109/42.906424

Zhang, Y., Li, J., Song, S., Tardif, T., Burmeister, M., Villafuerte, S. M., … Shu, H. (2016). Association of DCDC2 Polymorphisms with Normal Variations in Reading Abilities in a Chinese Population. *PloS One*, *11*(4), e0153603. https://doi.org/10.1371/journal.pone.0153603

Zhao, H., Chen, Y., Zhang, B.-P., & Zuo, P.-X. (2016). KIAA0319 gene polymorphisms are associated with developmental dyslexia in Chinese Uyghur children. *Journal of Human Genetics*, *61*(8), 745–52. https://doi.org/10.1038/jhg.2016.40

Zijta, F. M., Froeling, M., Van Der Paardt, M. P., Lakeman, M. M. E., Bipat, S., Montauban Van Swijndregt, A. D., … Stoker, J. (2011). Feasibility of diffusion tensor imaging (DTI) with fibre tractography of the normal female pelvic floor. *European Radiology*, *21*(6), 1243–1249. https://doi.org/10.1007/s00330-010-2044-8

SHORT CV AND PUBLICATIONS

Alberto De Luca obtained the scientific high school diploma at "Liceo Scientifico" P. Paleocapa (Rovigo, Italy) in 2007. During the same year he enrolled the biomedical engineering course at the University of Padova, where he achieved the bachelor and master degrees in 2011 and 2013.
Since the 1st of January 2014 he has been a Ph.D. student at the Department of Information Engineering of the University of Padova, under the supervision of Prof. Alessandra Bertoldo. The Ph.D. scholarship was funded by the Scientific Institute IRCCS E. Medea, where he carried out part of his research activities in the Neuroimaging Lab, directed by Dr. Filippo Arrigoni. His methodological research activities are mainly focused on Diffusion MRI, both in the brain and in the skeletal muscle, but he also carried out clinical processing of other MRI sequences. From September 2015 to February 2016 Alberto visited the Radiology Department of UMC Utrecht, The Netherlands, under the supervision and collaboration of Dr. Martijn Froeling.

Publications in international peer reviewed journals:

- **A. De Luca**, A Bertoldo, M Froeling: "Effects of perfusion on DTI and DKI estimates in the skeletal muscle", Magnetic Resonance in Medicine 2016 Aug 19, PMID: 27538923 DOI:10.1002/mrm.26373.
- S. Mascheretti and **A. De Luca**, V Trezzi, D. Peruzzo, A. Nordio, C. Marino, F. Arrigoni: "Neurogenetics of developmental dyslexia: From genes to behavior through brain neuroimaging and cognitive and sensorial mechanisms", Translational Psychiatry, In Press.
- **A. De Luca**, F Arrigoni, R Romaniello, FM Triulzi, D Peruzzo, A Bertoldo: "Automatic localization of cerebral cortical malformations using fractal analysis". Physics in Medicine and Biology, 2016 61(16):6025-40, PMID: 27444964 DOI: 10.1088/0031-9155/61/16/6025.
- M. Calabrese, M. Castellaro, A. Bertoldo, **A. De Luca**, FB Pizzini, GK Ricciardi, M Pitteri, S Zimatore, R Magliozzi, MD Benedetti, P Manganotti, R Reynolds, A Gajofatto, S Monaco: "Epilepsy in multiple sclerosis: The role of temporal lobe damage", Multiple Sclerosis Journal, 2016 June 3, PMID:27260699 DOI: 10.1177/1352458516651502.
- L. Squarcina, **A. De Luca**, M. Bellani, P. Brambilla, FE Turkheimer, A. Bertoldo: "Fractal analysis of MRI data for the characterization of patients with schizophrenia and bipolar disorder", Physics in Medicine and Biology, 2015 60(4):1697-716. Doi: 10.1088/0031-9155/60/4/1697.

Proceedings of international conferences:

- **A De Luca**, A Bertoldo, M Froeling: "Effects of perfusion on DTI and DKI estimates of the skeletal muscle". ISMRM Diffusion Workshop 2016, Lisbon, Portugal, 11-16 September 2016.
- **A De Luca**, A Bertoldo, M Froeling: "A correlation study of free diffusion and kurtosis changes in longitudinal acquisition of the skeletal muscle". ISMRM Diffusion Workshop 2016, Lisbon, Portugal, 11-16 September 2016.
- **A De Luca**, A Bertoldo, F Arrigoni, M Froeling: "Hindered diffusion, free water and pseudo-diffusion quantification in the brain: a comparison of Stejskal-Tanner and Flow-Compensated gradients.". ISMRM Diffusion Workshop 2016, Lisbon, Portugal, 11-16 September 2016.
- **A De Luca**, A Bertoldo, M Froeling: "Effects of perfusion on DTI and DKI estimates in the skeletal muscle". ISMRM 2016, Singapore, 07-13 May 2016
- **A De Luca**, G D'Angelo, D Peruzzo, F Triulzi, A Bertoldo, F Arrigoni: "Multi-parametric assessment of thigh muscles in patients with limb girdle muscular dystrophies (LGMD): preliminary results.", ISMRM 2016, Singapore, 07-13 May 2016.
- Arrigoni F, **De Luca A**, Peruzzo D, Romaniello R, Bertoldo A, Triulzi F: "A novel automatic method for the detection of malformations of cortical development based on fractal properties of cerebral cortex." ESNR 2015
- **A. De Luca**, M. Castellaro, S. Montemezzi, M. Calabrese, A. Bertoldo: "Tissue separation of multi-shell DW-MRI with a physiologically constrained multi compartment model and spherical deconvolution.", ISMRM 2015, Toronto, Canada, 29 May – 06 June 2015.
- **A. De Luca**, M. Castellaro, S. Montemezzi, M. Calabrese, A. Bertoldo: "Hippocampi and epilepsy in MS patients: a diffusion weighted imaging study with NODDI.", ISMRM 2015, Toronto, Canada, 29 May – 06 June 2015.
- **A. De Luca**, D. Peruzzo, F. Triulzi, F. Arrigoni, A. Bertoldo: "An automatic classificator based on local fractal features for the identification of cortical malformations", ISMRM 2015, Toronto, Canada, 29 May – 06 June 2015.
- M. Vavla, F. Arrigoni, E. Petacchi, A. Nordio, **A. De Luca**, E. Russo, S. Pizzighello, G. Paparella, E. Brighina, G. D'Angelo, E. Carraro, A. Martinuzzi: "Potential neuroimaging biomarkers validated in Friedrich's Ataxia: DTI and Functional magnetic resonance findings", IARC 2015, Berkshire, England, 25-28 March 2015.

- L. Squarcina, **A. De Luca**, M. Bellani, P. Brambilla, E. Turkheimer, A. Bertoldo: " Evaluation of gray matter complexity in psychiatric patients using fractal geometry", ISMRM 2014, Milan, Italy, 10-16 May 2014. ID Scopus: 2-s2.0-84922309065
- **A. De Luca**, L. Squarcina, M. Bellani, P.Brambilla, F. E. Turkheimer, A. Bertoldo:"Fractal dimension analysis of gray matter structure applied to schizophrenia patients",HBM 2013, Seattle, USA, 16-20 June 2013

Proceedings of national conferences

- Caratterizzazione multi parametrica del muscolo scheletrico di pazienti affetti da distrofia mediante risonanza magnetica 3T. A. De Luca, D. Peruzzo, G. D'Angelo, F. Arrigoni, A. Bertoldo. High-tech in neuroriabilitazione infantile: traguardi e sfide. 24-25 Settembre 2015, Bosisio Parini (LC).

RINGRAZIAMENTI

Il mio primo pensiero va ai miei genitori, per aver sempre supportato il mio percorso sino a questo traguardo. Ringrazio il mio supervisore Alessandra, per avermi introdotto alla ricerca, sempre fonte di motivazione e di opportunità. Grazie a Filippo, un amico più che un supervisore. Ho fortemente apprezzato la fiducia e il punto di vista clinico sulle attività che ho svolto. Martijn, lavorare con te è stata un'importante apertura mentale, lo scambio di idee e la collaborazione instaurata dalla mia visita hanno fortemente accelerato la mia crescita scientifica. Grazie anche per i momenti di svago fuori lavoro. Voglio sinceramente ringraziare i miei colleghi Andrea, Vittoria, Luca, gli studenti di dottorato del DEI, e sopra tutti Denis e Marco, ricordando particolarmente il loro aiuto nei primi mesi di attività, inclusi i suggerimenti per sopravvivere al primo ISMRM, nonché per le interessanti discussioni. Un grande grazie va a Sara, amica sincera e insostituibile. Grazie a Chiara, per aver condiviso buona parte di questo viaggio. Infine, un grande ringraziamento ai ragazzi dell'UMC Utrecht per la loro accoglienza, è stata un'esperienza straordinaria.

ACKNOWLEDGEMENTS

My first thought goes to my parents, who always supported the route that led me here. Many thanks go to my supervisor Alessandra, which introduced me to the world of MRI research and has been an invaluable source of motivation and opportunities. Thanks to Filippo, that I consider more a friend than a supervisor. I really appreciated the trust and the clinical points of view on what I carried out. Martijn, working with you has been mind opening, the exchange of ideas and the collaboration since my visit greatly boosted my scientific growth. Thanks also for the great times outside work. I want to sincerely thank all my colleagues, Andrea, Vittoria, Luca and the Ph.D. students at DEI, and among all Denis and Marco, especially for their help during the first months, including the tutorial to survive your first ISMRM, and for the interesting discussions. A special thank goes to Sara, sincere and irreplaceable friend. Thanks to Chiara, for sharing most of this journey. Finally, many thanks to all the guys at UMC Utrecht, very welcoming, I had a great time there.